



ISSN 1028-8546

Volume XVIII, Number 3

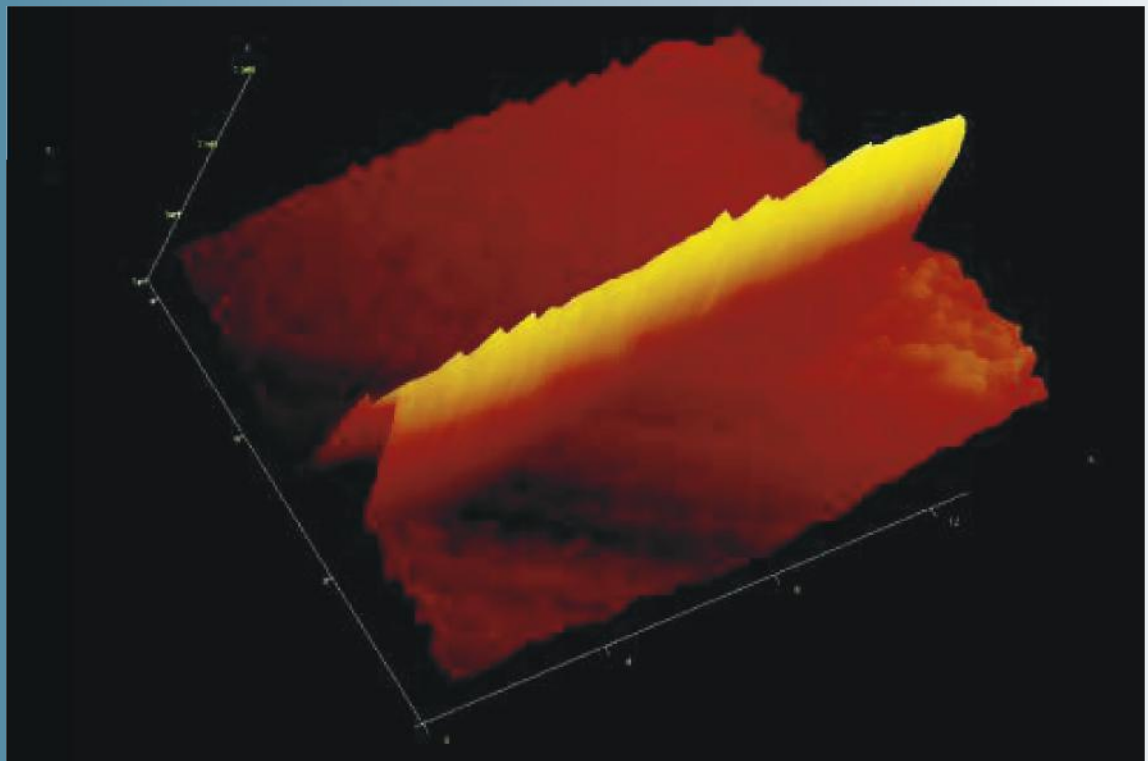
Section: En

September, 2012

# Azerbaijan Journal of Physics

# Fizika

[www.physics.gov.az](http://www.physics.gov.az)



G.M. Abdullayev Institute of Physics  
Azerbaijan National Academy of Sciences  
Department of Physical, Mathematical and Technical Sciences

## *Azerbaijan Journal of Physics*

# *Fizika*

*G.M.Abdullayev Institute of Physics  
Azerbaijan National Academy of Sciences  
Department of Physical, Mathematical and Technical Sciences*

### HONORARY EDITORS

**Arif PASHAYEV**

**Mahmud KERIMOV**

### EDITORS-IN-CHIEF

Arif HASHIMOV  
Chingiz QAJAR

### SENIOR EDITOR

Talat MEHDIYEV

### INTERNATIONAL REVIEW BOARD

Ivan Scherbakov, Russia  
Kerim Allahverdiyev, Turkey  
Mehmet Öndr Yetiş, Turkey  
Gennadii Jablonskii, Buelorussia  
Rafael Imamov, Russia  
Vladimir Man'ko, Russia  
Eldar Salayev, Azerbaijan  
Dieter Hochheimer, USA  
Victor L'vov, Israel  
Vyacheslav Tuzlukov, South Korea  
Majid Ebrahim-Zadeh, Spain

Firudin Hashimzadeh, Azerbaijan  
Anatoly Boreysho, Russia  
Mikhail Khalin, Russia  
Hasan Bidadi, Tebriz, East Azerbaijan, Iran  
Natiq Atakishiyev, Mexico  
Maksud Aliyev, Azerbaijan  
Bahram Askerov, Azerbaijan  
Vali Huseynov, Azerbaijan  
Javad Abdinov, Azerbaijan  
Bagadur Tagiyev, Azerbaijan  
Tayar Djafarov, Azerbaijan

Talat Mehdiyev, Azerbaijan  
Nazim Mamedov, Azerbaijan  
Emil Guseynov, Azerbaijan  
Ayaz Bayramov, Azerbaijan  
Tofiq Mammadov, Azerbaijan  
Salima Mehdiyeva, Azerbaijan  
Shakir Naqiyev, Azerbaijan  
Rauf Guseynov, Azerbaijan  
Almuk Abbasov, Azerbaijan  
Yusif Asadov, Azerbaijan

### TECHNICAL EDITORIAL BOARD

senior secretary Elmira Akhundova, Nazli Huseynova, Sakina Aliyeva,  
Nigar Akhundova, Elshana Aleskerova

### PUBLISHING OFFICE

33 H.Javid ave, AZ-1143, Baku  
ANAS, G.M.Abdullayev Institute of Physics

Tel.: (99412) 439-51-63, 439-32-23

Fax: (99412) 447-04-56

E-mail: [jophphysics@gmail.com](mailto:jophphysics@gmail.com)

Internet: [www.physics.gov.az/index1.html](http://www.physics.gov.az/index1.html)

It is authorized for printing: 30.09.2012

Published at: "ŞƏRQ-QƏRB"  
17 Ashug Alesger str., Baku  
Typographer :Aziz Gulaliyev

Sent for printing on: \_\_ .2012

Printing approved on: \_\_ .2012

Physical binding: \_\_\_\_\_

Number of copies: \_\_\_\_\_200

Order: \_\_\_\_\_

## SHF-MAGNETIC RESONANCES IN NICKEL-ZINC FERRITE

A.A. HABIBZADE, Sh.N. ALIYEVA, S.I. ALIYEVA, T.R. MEHDIYEV

*Institute of Physics, Azerbaijan National Academy of Sciences**Baku, AZ 1143, H. Javid ave.,33*

The super-high-frequency ferromagnetic resonance in Ni-Zn films of different thickness and structure (Ni-Zn film)-dielectric-(Al-screen) has been investigated in temperature interval from 300 up to 450K. The presumable interpretation of obtained investigated results is given in this work.

**Keywords:** ferromagnetic resonance, nickel-zinc ferrite, surface waves

**PACS:** 75.47.Lx, 76.50

## INTRODUCTION

The surface electromagnetic waves are excited by nonuniform magnetic field formed in ferrite by electric current passing on metallic conductor situated on the investigated sample surface, particularly film. The spectrum and the structure of magnetostatic waves propagating in the film are defined by magnetodipole spin-spin interactions caused by dissipation fields appearing at magnetization oscillations in the film without magnetocrystalline anisotropy

The practical interest to the study of surface electromagnetic waves is connected with the fact that their energy inversely decreases to the distance, whereas the energy of volume electromagnetic wave inversely decreases as the square of the distance from point source. This circumstance in practices essentially increases the range of communication system action and also increases their efficiency because of the fact that wave is "fixed" to the surface and "follows" on its curvature.

The present investigations are carried out with the aim of the study of the processes leading to appearance of surface electromagnetic waves in layered structures of ferrite-dielectric-metal [1-22] and also conditions at which the modulation instabilities caused by dispersion peculiarities of these structures appear. The well known nickel-zinc ferrite compositions of  $Ni_{1-x}Zn_xFe_2O_4$  type synthesized on sol-gel technology and having wide use are used in the capacity of the ferrite material.

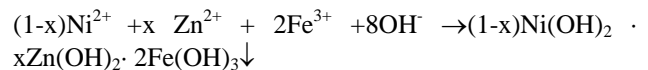
SYNTHESIS OF SOLID SOLUTIONS  $Ni_{1-x}Zn_xFe_2O_4$ 

The micro- and nano-powders of solid solutions  $Ni_{1-x}Zn_xFe_2O_4$  are obtained by the way of co-precipitation

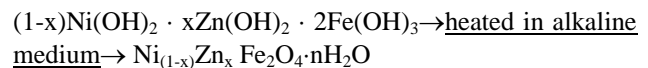
[23-27] of water solutions of impurities  $NiCl_2$ ,  $ZnCl_2$  and  $FeCl_3$  in alkaline medium.

The mixtures of  $NiCl_2$ ,  $ZnCl_2$  and  $FeCl_3$  in stoichiometric relation: 100mL (1-x)M  $NiCl_2$ , 100mL xM  $ZnCl_2$  and 100mL from 2M  $FeCl_3$ , where x changes from 0 up to 1 are prepared and endured at temperature 60°C. The obtained mixtures are added to boiled solution 0.63M NaOH dissolved in 1200ml of distilled water at constant mixing.

The transformation reaction of metal salts in hydroxides is carried in alkaline medium:



Further, the solution of metal hydroxides is kept at temperature 85°C during one hour in alkaline medium that leads to its transformation into ferrite in nano-particle form:



The synthesized micro- and nano-particles of ferrite are filtered by magnet method, carefully washed in distilled water; later in acetone and later are dried at room temperature.

TEM images of obtained ferrite nano-crystals  $Ni_{1-x}Zn_xFe_2O_4$ . (x=0; 0.5; 0.6; 0.8; 1.0) are shown on fig.1.

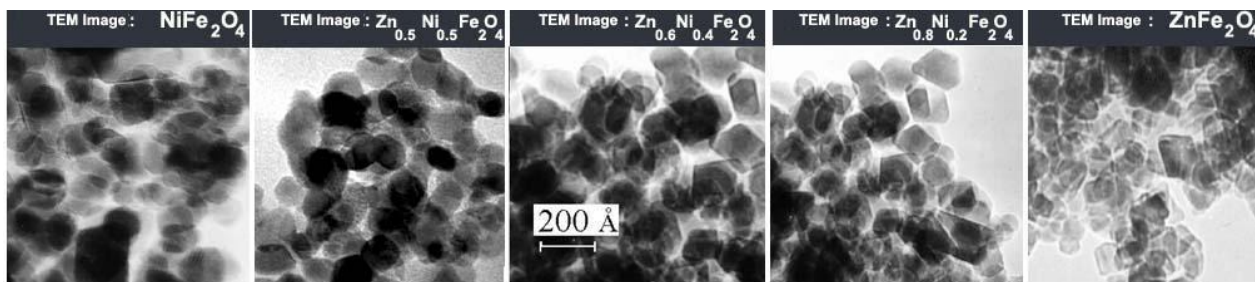
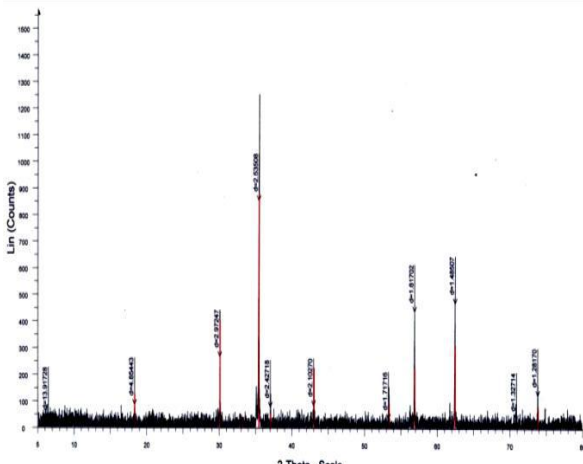


Fig.1. TEM images of prepared nanocrystalline ferrites  $Ni_{1-x}Zn_xFe_2O_4$  (x=0; 0.5; 0.6; 0.8; 1.0)



0110311\_Peromagnit - File: 172211\_Peromagnit.cvx - Type: 2Th/Th locked - Start: 5.000° - End: 79.967° - Step: 0.010° - Step time: 4.8 s - Temp: 25 °C (Room) - Time Binned: 16 s - 2-Theta: 0.000°  
 Operation: Step (Method: 0.000) Background: 1.000 (1.000) report  
 0110311\_Peromagnit - Method: Step Scan - Date: 06/20/2016 10:20:19 - 71.7036 % - d by 1 - Vol: 1.9408 - Cubic - a: 8.39902 - b: 8.39902 - c: 8.39902 - alpha: 90.000 - beta: 90.000 - gamma: 90.000 - Fc

<i>d</i> (Å)	<i>i</i>	<i>h</i>	<i>k</i>	<i>l</i>
4.84936	7.2	1	1	1
2.96962	35.6	2	2	0
2.53250	100	3	1	1
2.42468	8.1	2	2	2
2.09984	17.3	4	0	0
1.71451	10.8	4	2	2
1.61646	20.1	5	1	1
1.48481	21.6	4	4	0
1.41975	2.7	5	3	1
1.32805	3	6	2	0
1.28089	4	5	3	3
1.26625	2	6	2	2
1.21234	2	4	4	4

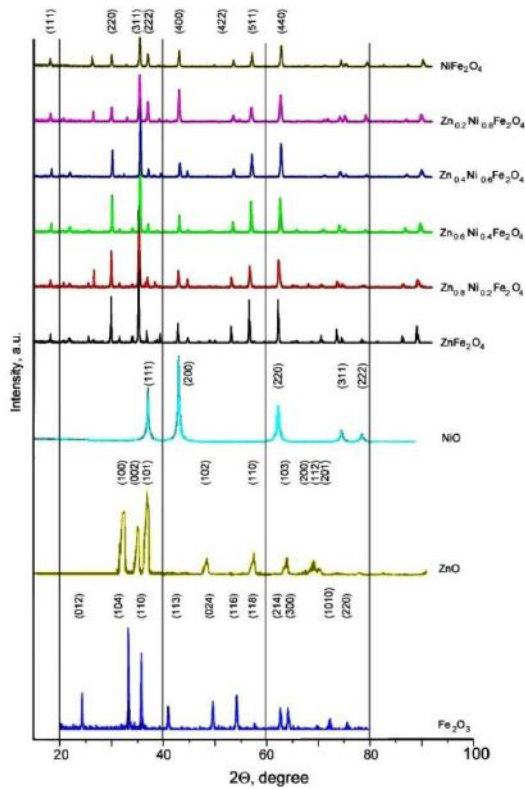


Fig.2. Indexed x-ray diffraction pattern for  $Ni_{1-x}Zn_xFe_2O_4$  with *x* varying from 0 to 1.0 by step 0.2

X-ray photos (XRD) of synthesized powders  $Ni_{1-x}Zn_xFe_2O_4$  are studied on powder diffractometer D8 ADVANCE (Bruker Ltd.) ( $CuK\alpha$ ,  $\lambda = 1.540600 \text{ \AA}$ ) and are given on Fig.2.

The scanning of the chosen peaks is made with the step  $0.010^\circ$ , measurement time 5,8sec at temperature  $25^\circ C$ . For  $x=0.5$  the parameter values are equal:  $a=8.39900\text{ \AA}$ ,  $z=8$ , mol. weight = 234.39, volume =  $592.49\text{ \AA}^3$ , space symmetry group  $Fd3m$ .

The observable plane reflections (311), (400), (422), (511) and (440) in roentgen spectra correspond to spinel structure. The strongest reflection is observed from plane (311). The peaks (220) show on the fact that the half number of  $Fe^{3+}$  ions in inverted spinels are in tetrahedral spaces and the second half number of  $Fe^{3+}$  ions and  $Ni^{2+}$  ions are in octahedral spaces.

The analogous results of roentgen experiments are obtained in work [23].

The data on diffraction of X-ray radiation in  $Ni_{0.5}Zn_{0.5}Fe_2O_4$  (fig.3) agree with investigation results (for example [35]) and allows us to establish that structural changes are observed at two-hour annealing of obtained micro-particles. These structural changes correspond to behavior of ZnO lines with the temperature changes, especially after  $600^\circ C$  and increase of fraction number till this line becomes dominating one at  $1100^\circ C$ . At temperatures from  $900^\circ C$  up to sintering temperature  $1100^\circ C$ , the ferrite particle sizes estimated by widening of Sharer's maximums remain nano-dimensional ones. One can suppose that ZnO causes to sintering process acting as barrier for the particle growth. The coincidence of roentgen lines  $Fe_2O_3$ , ZnO,  $NiFe_2O_4$ ,  $ZnFe_2O_4$  with  $Ni_{1-x}Zn_xFe_2O_4$  shown on Fig.2 and 3, allows us to give the following interpretation of observable maximums in spectra  $Ni_{1-x}Zn_xFe_2O_4$ .

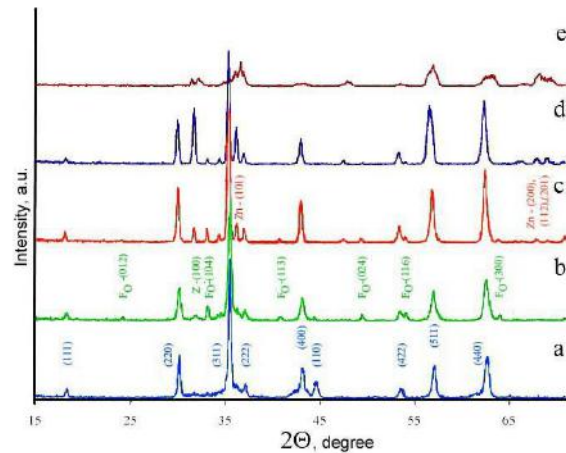


Fig.3. X-ray diffraction  $Ni_{0.5}Zn_{0.5}Fe_2O_4$  at different temperatures: a is after synthesis; b is 600C; c is 800C; d is 900C; e is 1180C.  $F_0 - Fe_2O_3$ ; Zn - ZnO. (the experiment is carried out on X-ray diffractometer X PERT PRO, PANalytical, Netherlands)

Fe-edge firstly existing in pure phase of Ni-Zn ferrite decomposes on  $Fe_2O_3$  and the mixture of Ni and Zn ferrites; ZnO part increases with sintering temperature. The line intensities observable for samples sintered at temperatures 800C and 900C show the increase of ZnO phase crystallinity. The change of Zn content in b

$Ni_{1-x}Zn_xFe_2O_4$  ( $x$  changes from 0 up to 1) leads to the increase of “a” parameter from 8.288 up to 8.440Å, i.e. in interval boundaries corresponding between parameters “a” of lattices  $NiFe_2O_4$  and  $ZnFe_2O_4$ .

The average size of crystallites decreases from 8.95 up to 6.92 nm with increase on zinc concentration (Fig.3). Note that the difference of Ni obtaining conditions also leads to the change of crystallite sizes.

In temperature interval from 800°C up to 1100°C in  $Ni_xZn_{1-x}Fe_2O_4$  the nickel in element form the quantity of which gradually increases up to total composition is observed.

In temperature interval from 800°C up to 1100°C the nickel in  $Ni_xZn_{1-x}Fe_2O_4$  ferrite presences in element form, increasing up to total quantity of nickel in the system.

The change of Zn content in  $Ni_{1-x}Zn_xFe_2O_4$  ( $x$  changes from 0 up to 1) leads to the increase of “a” parameter from 8.288 up to 8.440Å, i.e. in interval boundaries corresponding between parameters “a” of lattices  $NiFe_2O_4$  and  $ZnFe_2O_4$ .

The average size of crystallites decreases from 8.95 up to 6.92 nm with increase on zinc concentration (Fig.4). Note that the difference of Ni obtaining conditions also leads to the change of crystallite sizes.

In temperature interval from 800°C up to 1100°C in  $Ni_xZn_{1-x}Fe_2O_4$  the nickel in element form the quantity of which gradually increases up to total composition is observed.

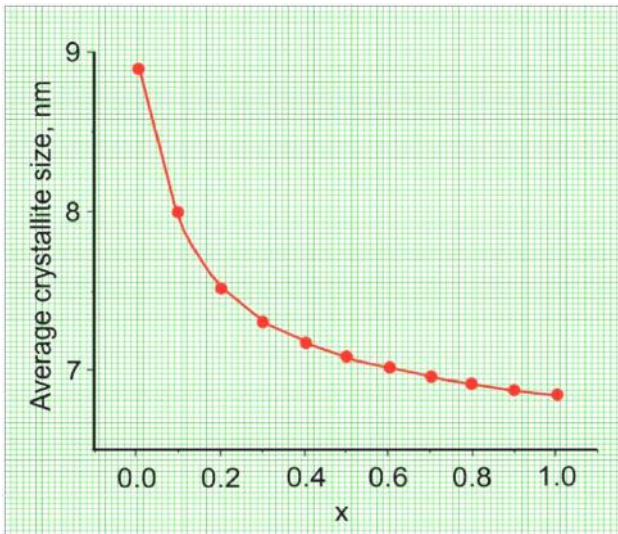


Fig.4 The average sizes of ferromagnetic particles  $Zn_xNi_{1-x}Fe_2O_4$  obtained by hydrothermal method in the dependence on zinc content.

**MAGNETIC PROPERTIES OF SOLID SOLUTIONS  $Ni_{1-x}Zn_xFe_2O_4$**

The solid solutions  $Ni_{1-x}Zn_xFe_2O_4$  of nickel-zinc ferrites are inverted spinels [29] and present themselves the replacement solid solutions formed by two ferrites, the one of which  $NiFe_2O_4$  is ferromagnetic and another  $ZnFe_2O_4$  doesn't have the magnetic properties.

The composition of solid solution with taking into consideration cations by oxygen interstices is characterized by formula:  $(Zn_x^{2+} Fe_{1-x}^{3+}) [Ni_{1-x}^{2+} Fe_{1+x}^{3+}] O_4$ .

The circumstance that  $Fe^{2+}$  ions are easily exchanged by bivalent  $Ni^{2+}$  and  $Zn^{2+}$  ions, explains the statistic distribution on tetrahedral voids of  $Zn^{2+}$  and  $Fe^{3+}$  ions, octahedral voids of  $Ni^{2+}$  и  $Fe^{3+}$  ions and high electric conduction of compound. As the cations of different valences take the crystallographically and energetically equivalent positions in the lattice, so the electron exchange reactions carry out with activation energy  $\Delta E \approx 0,05eV$ .

The zinc cations in spinel structure always take tetrahedral knots. Thus, zinc introduction into crystal lattice is accompanied by displacement of ferrum ions in octahedral positions that leads to decrease of compensation of cation magnetic moments being in A and B sublattices and therefore to increase of magnetization of solid solution saturation, weakens the exchange interaction of A-O-B type that expresses in monotonous Curie temperature decrease at the increase of molar part of  $ZnFe_2O_4$  in ferrite spinel composition. In  $x > 0,5$  region the ion magnetic moments in tetrahedral sublattice aren't able to anti-parallel orientate the cation magnetic moments of B-lattice and the rapid decay of saturation induction, crystal anisotropy decrease and increase of initial ferrite magnetic permeability are observed. The solid solution  $Ni_{1-x}Zn_xFe_2O_4$  where  $x \approx 0,7$  corresponds to maximal value of magnetic permeability.

The physical model of magnetic properties of solid solutions  $Zn_xNi_{1-x}Fe_2O_4$  is proposed in work [28] and experimentally proved in work [29]. It is proved that till  $x = 0,4$   $Zn^{2+}$  ions take only tetrahedral knots. This is also proved by the fact that in tetrahedral coordination  $m_{Fe^{3+}}$  is equal to 5. The further increase of  $Zn^{2+}$  concentration leads to situation when some part of  $Zn^{2+}$  ions begins to fill the octahedral knots. This process leads to the decrease of solid solution magnetization. The presence of some number of  $Zn^{2+}$  ions in octahedral sublattice also explains the results of work [29] in which the interaction relations between sublattices in preposition that all  $Zn^{2+}$  ions takes tetrahedral knots are calculated. The experimental results on dependence of spontaneous magnetization are presented on fig.5-6. The “hypothetic” magnetization is defined by the following expression:

$$M_s^{hyp.} = M_s - \gamma(a_x - a_{x=0.3})$$

for all “x” values which are bigger 0,3 where  $M_s$  is experimental value for the given “x”;  $\gamma$  is interaction constant [29];  $a$  is lattice constant. The negative  $\gamma$  value is explained in work [28] by ratio fluctuations of  $Zn^{2+}$  and  $Fe^{3+}$  ion numbers in tetrahedral knots. The constant  $\gamma$  depends on lattice constant and oxygen ion position and also on interaction values  $Fe^{3+} - Fe^{3+}$ ,  $Fe^{3+} - Zn^{2+}$  and  $Zn^{2+} - Zn^{2+}$  and cation distributions. The values  $\gamma_{0.4} = -1.6$   $\gamma_{0.5} = -1.65$ ;  $\gamma_{0.6} = -1.71$ ;  $\gamma_{0.7} = -1.79$  correspond to obtained experimental data.

It is known that at increase of ferromagnetic particle sizes, they should be one-domain ones, as the magnetostatic energy proportional to its volume decreases rapider than boundary energy between domains that is proportional to particle surface. Magnetic properties of few ferromagnetic powders are defined by properties of one domain. The value of limit (critic) radius for uniaxial

crystal, at which the homogeneous magnetization saves, is defined by expression [30]:

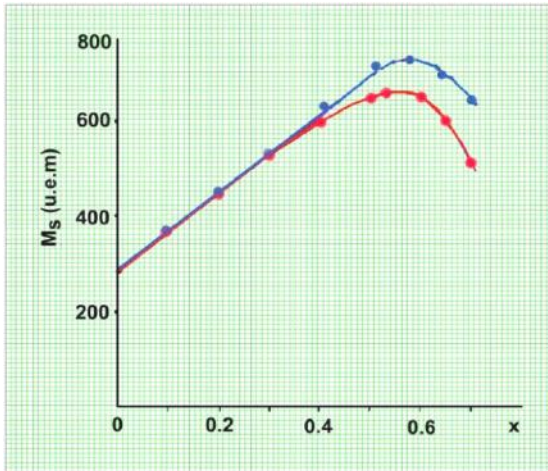


Fig.5. The dependence of spontaneous (full curve) and “hypothetic” (dotted curve) magnetizations  $Ni_{1-x}Zn_xFe_2O_4$  on zinc content.

$$R_c \approx \frac{0.95}{J_s} (10A)^2 \left( Q - \frac{2K}{J_s^2} - \frac{H}{J_s} \right)^{\frac{1}{2}} \quad (1)$$

where  $J_s$  is saturation magnetization;  $A$  is exchange energy parameter;  $K$  is constant anisotropy;  $Q$  is demagnetizing factor;  $H$  is magnetic field strength. Note that particle with radius satisfying to the given equation at all field values  $H > -\frac{2K}{J_s}$  remains one-domain one. At

further decrease of  $R$  radius in the particle system, the probability of Brownian motion of sum magnetic moment vector increases proportionally to  $\exp(E/k_B T)$  where  $E$  depends on anisotropy constant and particle volume and has the meaning the energy barrier at overcoming of which the thermal fluctuations can make the magnetic moment rotation.

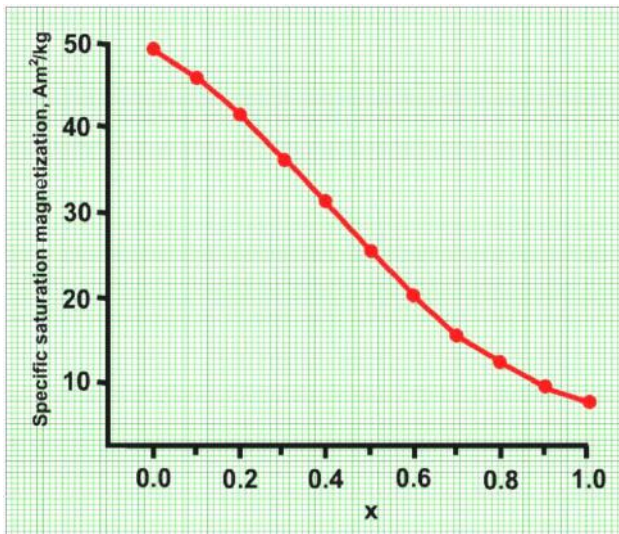


Fig.6 The dependence of solid solution magnetization  $Ni_{1-x}Zn_xFe_2O_4$  obtained by hydrothermal method on zinc content.

In work [29] it is shown that the magnetization stability in this case saves at particle sizes not less  $50\text{\AA}$ . The particle system with radiuses less than critical one behaves itself similar to paramagnetic atom ensemble having the big magnetic moment. Thus, the dependence of magnetization value of solid solutions  $Ni_{1-x}Zn_xFe_2O_4$  obtained by hydrothermal method with the change of zinc concentration (see fig.6) becomes clear.

### COMPOSITE MAGNETIC SPECTRA (POLYMER DIELECTRIC +MIXTURE OF $Ni_{1-x}Zn_xFe_2O_4$ NANOPOWDERS)

The mechanical mixture of obtained nano-powders of solid solutions zinc-nickel ferrites is used as of filler for matrix from polymer dielectric with low dielectric constant.

The concentration of ferrite powder mixture in dielectric matrix is chosen so that at the condition of particle distribution on matrix volume and absence of contacts between particles, magnetic permeability is defined by sum of magnetic permeabilities of each fraction, i.e.  $\ln \mu = \sum v_i \ln \mu_i$  where  $\mu_i$  is magnetic permeability,  $v_i$  is volume part of  $i$ -fraction of powder-filler in the composite. It is established that for the obtaining of these conditions the volume part of nano-powder mixture in dielectric matrix shouldn't be bigger than 0,65. The experimental dependences of mixture component magnetization  $Ni_{1-x}Zn_xFe_2O_4$  where  $x=0.0; 0.2; 0.4; 0.6; 0.8; 1.0$  are shown on fig.7. The magnetization dependence (polymer dielectric +nano-powder mixture  $Ni_{1-x}Zn_xFe_2O_4$  where  $x=0.2; 0.4; 0.6; 0.8$ ) on nano-powder volume part in polymer matrix is presented on fig.8. The experimental dependences presented on figures 8-9 are in well coincidence with physical model.

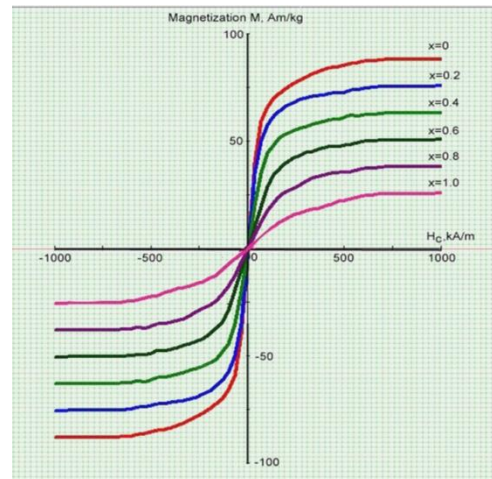


Fig. 7.The dependences of nano-powder magnetization  $Ni_{1-x}Zn_xFe_2O_4$  where  $x=0.0; 0.2; 0.4; 0.6; 0.8; 1.0$ .

The oscillogram of dependence of signal  $u(f)$  generated by sample on frequency of modeling magnetic field is given on Fig.9 and Fig.10. The two resonance peaks on frequencies 23 and 177 kHz corresponding to modes of bending and planar vibrations are observed in spectrum.

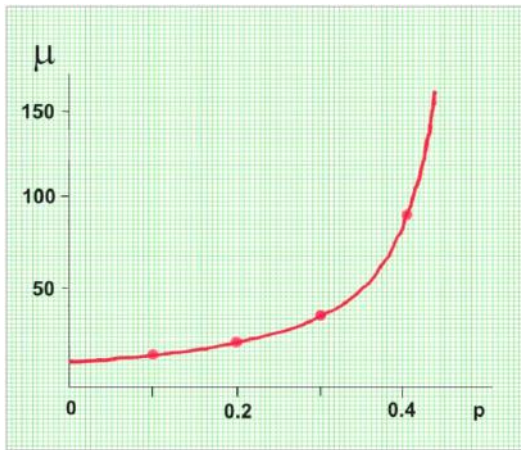


Fig.8. The dependence of composite magnetization (polymer dielectric +nano-powder mixture  $Ni_{1-x}Zn_xFe_2O_4$  where  $x=0.2; 0.4; 0.6; 0.8$ ) on concentration of nano-powder mixture in polymer matrix.

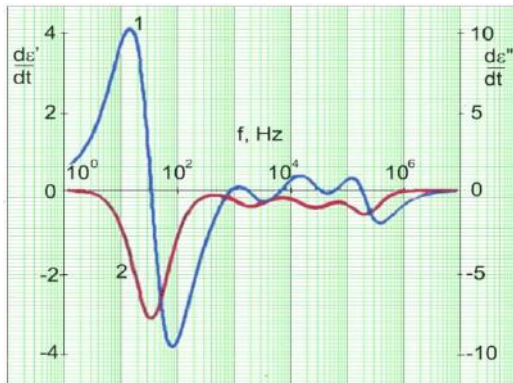
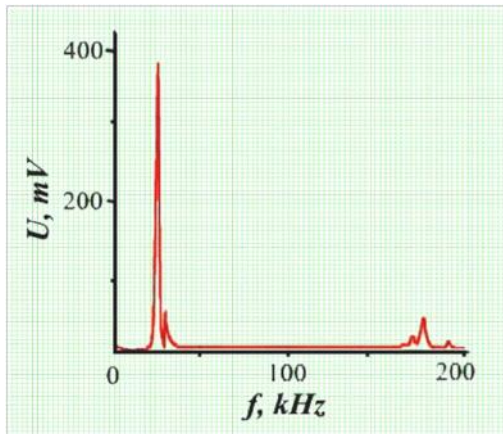


Fig.9. The sample spectrum oscillogram of  $Ni_{1-x}Zn_xFe_2O_4$  in dependence on frequency of modeling magnetic field. For comparison the differential frequency dependences of actual (1) and imaginary (2) parts of dielectric constant for PVC matrix at  $30^{\circ}C$ .

The planar oscillations appear as a result of displacement of field contact on the one of sample surfaces and consequently don't characterize the investigation object.

As analysis shows the absorption spectrum is connected with frequency dependence of ferrite permeability, frequency dependence of composite, and transition from three-dimensional character to two-dimensional one of passing current.

The transition boundary frequency from three-dimension to two-dimension current character is shown by dot line  $l_p$ .

The current behavior at skin effect is defined by scale of mixed conduction system, i.e. the skin-current propagating on resistor at the skin-effect depth less than  $l_p$  will be two-dimensional character and at depth bigger than  $l_p$  it will be the three-dimensional one.

The position of the scale of mixed conduction  $l_p$  as a result of dependence on component conduction coefficients  $\sigma_1(\omega)$  and  $\sigma_2(\omega)$  should depend on frequency  $\omega$ . The calculation shows that such value of  $l_p$  corresponds to signal frequencies higher than 200 kHz.

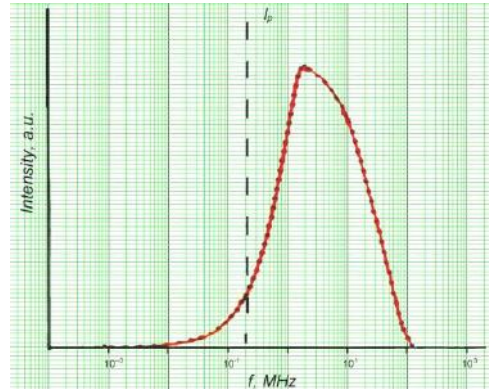


Fig.10. The absorption spectrums of  $Zn_xNi_{1-x}Fe_2O_4$  in frequency region from  $10^2$  up to  $2 \cdot 10^8$  Hz.

### MAGNETIC RESONANCES $Ni_{1-x}Zn_xFe_2O_4$ IN SPECTRUM MICRO-WAVE REGION

The measurements of frequency dependence of real and imaginary components of magnetic permeability, reflection coefficient from samples in frequency range  $0.3 \div 1300$  MHz are carried out with the help of measurement system of complex coefficients of transmission conjugated with computer system of signal registration and treatment. The samples positioned on metallic plane are put into measurement cell agreed with coaxial measurement tract in measurement regime of passing or reflection. The tract supplies the wave propagating of TE, TM and TEM – modes. The data of validity of amplitude and phase measurements of weakened signal is achieved by introduction of set of fixed attenuators, reference terminations of corresponding frequency range. The measurements of magnetic resonance spectra are also carried out on EPR-installation of Bruker LTD (Germany), ELEXSYS-II E500 CW-EPR. The ratio of standardized sample signal Weak Pitch to the noise is 3000:1. SHF-emitter includes the powerful doubled source of Gunn diode type with super-low noise level and also the resonator with super-high goodness. The installation is supplied by Herg program packet for professional EPR-spectrometry. The frequency range: from 1 up to 263 GHz.

The resonator of rectangular type by length  $l=50$  mm and  $a=5.2$ mm and  $b=3.2$ mm [32] in which the measured sample is situated, is switched on in high-frequency tract cascaded providing the measurement area from 26 up to 38Hz. The resonance frequencies decrease and maximum

width of corresponding maximums increases at putting of investigated samples into resonator.

At the absence of external magnetic field with the increase of frequency the passing coefficient increases and reflection coefficient decreases (Fig12). The obtained resonant spectra coincide with results of work [31] and are given on figures 11-13.

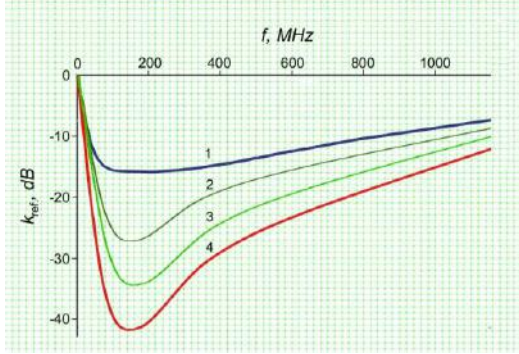


Fig.11. The frequency dependence of reflection coefficient on ferrite film surface: 1 is Ni-Zn ferrite without stoichiometry disturbance; 2 is Ni-Zn ferrite with 18mol.% ferrum oxide excess; 3 is Ni-Zn ferrite with 38mol.% ferrum oxide excess; 4 is Ni-Zn ferrite with 52mol% excess of iron oxide over stoichiometry.

For comparison with obtained results in frequency region up to 1Hz on following figure are given the data on reflection spectrums and magnetic resistance from publication [34] and from work [33] are given data on frequency dependence of dielectric constant for NiZnFe<sub>2</sub>O<sub>4</sub> ferrites with different molar relations Ni<sup>2+</sup>/Zn<sup>2+</sup>/Fe<sup>2+</sup>/Fe<sup>3+</sup>: 1/2/5/2(b1), 3/3/10/4(b), 2/1/5/2(b2), 5/1/10/4(b3).

The comparison shows that high-frequency resonance observed in frequency region up to 1Hz is hypothetically defined by the presence of ferrum oxide included in the structure of reverse spinel (Ni-Zn ferrite).

The experimental investigations of magnetic resonance in nickel-zinc nano-composite are carried out for two polarizations:  $H//H^{SHF}$  and  $H\perp H^{SHF}$  and four particles 26, 28, 30, 32 GHz. In both polarizations the position of resonance line changes to the side of more strong magnetic fields. The following values are measured:

$$d_m = \frac{|D(H)| - |D(0)|}{|D(0)|}; k_m = \frac{|R(H)| - |R(0)|}{|R(0)|}$$

where  $D(H)$  is transmission in external magnetic field;  $D(0)$  is transmission without external magnetic field;  $R(H)$  is reflection in external magnetic field;  $R(0)$  is reflection in the absence of external magnetic field. The spectra of transmission and reflection without external magnetic field are given on fig.12.

It is obvious that the observed frequency dependences  $R(0)$  and  $D(0)$  are caused not only by frequency dependences of absorption coefficient but also dispersion properties of  $TE_{10}$  mode.

The magnetic resonance spectra in Zn-Ni nano-composite at passing through the composite of

electromagnetic waves with frequencies: 1 is 26 GHz; 2 is 28GHz; 3 is 30GHz; 4 is 32GHz ; upper figure corresponds to geometry  $H//H^{SHF}$ ; low one corresponds to  $H\perp H^{SHF}$  are shown on fig.13.

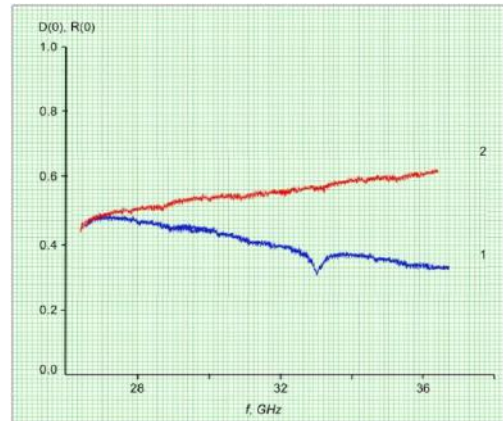
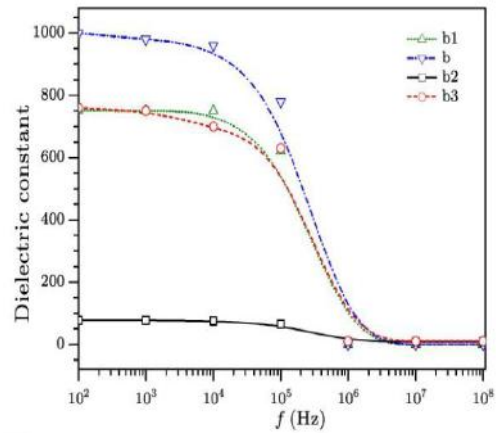
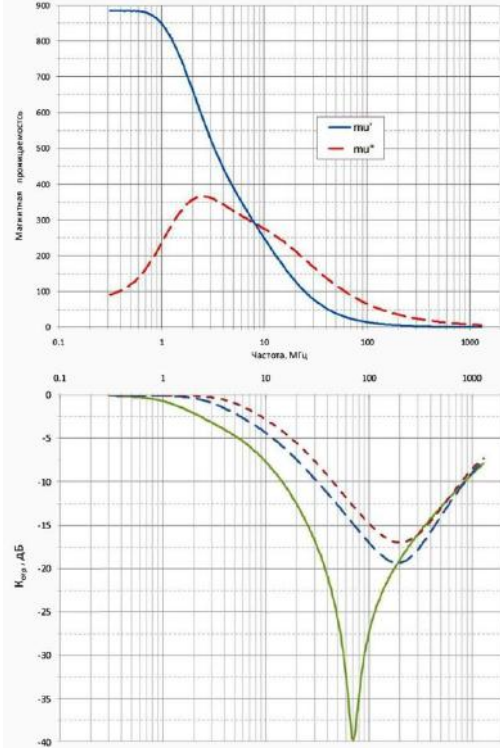


Fig.12 The transmission and reflection spectrums of Ni-Zn nano-composite in the absence of external magnetic field: 1 is reflection; 2 is transmission.

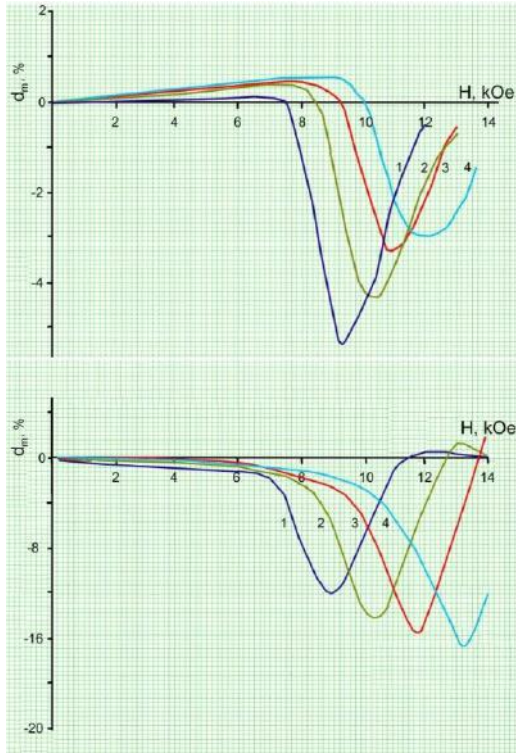


Fig.13. The magnetic resonance in Ni-Zn nano-composite at passing of electromagnetic waves through it with frequencies:1 is 26 GHz; 2 is 28GHz; 3 is 30GHz; 4 is 32GHz ; upper is  $H//H^{SHF}$ ; low is  $H\perp H^{SHF}$ .

The signal amplitude for different frequencies in the second case almost linearly increases with the increase of applied magnetic field and in first case it decreases. The explanation of this effect is correctly given in work [31] and connected with increasing amplitudes of resonator self-resonant frequencies with frequency increase for  $H\perp H^{SHF}$  case and in  $H//H^{SHF}$  case it is connected with the fact that vector direction of internal constant field approximates to the direction of external field. The differential spectra of ferromagnetic resonance (fig.14) are obtained for sizes of  $Ni_{1-x}Zn_xFe_2O_4$  particles which are equal to 10, 11, 12 and 16 nm.

The investigation results are given in following table:

Size nm	Resonance field, Oe	Linewidth, Oe	Relaxation time, ps	Magnetization, emu/g
10	3328	836	65	9.1
11	3105	1071	48	10.5
12	3007	1666	29	19.5
16	2796	2242	20	23

From temperature EPR-investigations  $Ni_{0.35}Zn_{0.65}Fe_2O_4$  (Fig.15) follows that the distribution of surface magnetic waves depends on boundary conditions. The films of different magnetizations have the different frequency pass bands of normal mode that corresponds to different conditions of appearance and distribution of surface magnetostatic waves in Ni-Zn ferrite film-dielectric-metal structure. The electromagnetic wave damping under influence on external magnetic field in all compositions of solid solutions  $Zn_xNi_{1-x}Fe_2O_4$  takes place

enough rapidly, that is connected with increase of absorption coefficient as it is followed from measurement.

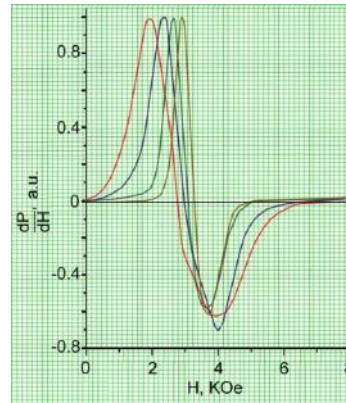


Fig.14. The temperature dependence of EPR –spectrum of  $Ni_{0.35}Zn_{0.65}Fe_2O_4$ : 1 is 300K; 2 is 350K; 3 is 400K; 4 is 425K; 5 is 450K.

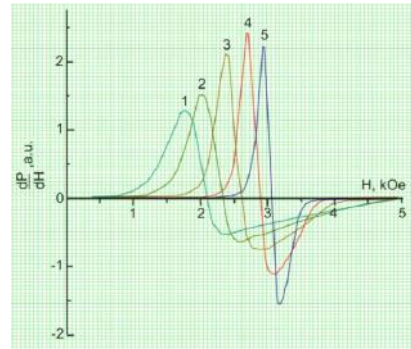


Fig.15 The temperature dependence of EPR –spectrum of  $Ni_{0.35}Zn_{0.65}Fe_2O_4$ : 1 is 300K; 2 is 350K; 3 is 400K; 4 is 425K; 5 is 450K.

Note that analogous temperature behavior of EPR spectrums is observed at study of states of nano-particle ferrum oxides (III) in a polyethylene matrix [36].

The usual theory of EPR in nano-particles [37,38] predicts the decrease of line width with temperature increase because of influence decrease of supermagnetic fluctuations. As resonant line widening and its shifting are connected with each other by definite relations [39], then one can consider about presence of phase transitions in the system on their carrying out [40]. In the given case, the experiments show on the fact that the anomalous behavior of EPR spectrum is observed in the investigated temperature region in  $Zn_{0.65}Ni_{0.35}Fe_2O_4$ . As is supposed in [36], this can be connected firstly with melting of binding matrix, secondly, with change of structure, dimensions and etc of micro-particles themselves. The small growth of width line in interval higher 450K can be connected with additional widening mechanism appearing in weakly viscous matrix. It is known that magnetic moment fluctuations take place in solid matrix by Neel mechanism. In liquid matrix one should take into consideration the Brownian relaxation mechanism as magnetization light axes of separate particles have the possibility to move. The rapid narrowing of EPR line higher 600K can be evidences either about change of inner particle structure or their enlargement. The latest factor leads to decrease of

supermagnetic fluctuations causing the widening of EPR signal.

Thus, as it is followed from X-ray data, (see in the beginning of present article), the observed behavior of EPR spectrums should be directly connected with structural changes in Ni-Zn ferrite in high temperature region.

The appearance of anisotropy of EPR signal after heating in magnetic field evidences about partial ordering of easy magnetization axes of nano-particles saving after matrix hardening.

### SURFACE ELECTROMAGNETIC WAVE ON METAL-DIELECTRIC BOUNDARY

It is known that the surface magnetostatic waves propagating in single tangent magnetized ferromagnetic film [15] at the increase of signal level are stable ones in respect to longitudinal excitations. For such wave type the modulation instability is absent in direction of excitation propagation. In works [16,17] it is shown that modulation instability of surface magnetostatic waves in single ferromagnetic film can appear even at excitation of two signals on different frequencies as a result of mutual influence between two modulation stable waves.

The metal presence allows us to obtain any form of dispersion and also gives the possibility to control of transmission band changing it in wide limits.

In present paper Al is used in the capacity of metal for which:  $\sigma_0 = 3.7 \cdot 10^{17} s^{-1}$ ;  $r_s/a_0 = 2.07$ ;  $l_s = 161 \text{ \AA}$ ;  $\Gamma = 12.5 \cdot 10^{13} s^{-1}$ ;  $\tau = 0.8 \cdot 10^{-14} s$ ;  $\omega_p = 2.4 \cdot 10^{16} s^{-1}$ . Here  $\Gamma$  is collision frequency with phonons, defects and other electrons;  $\sigma$  is conductivity;  $\tau = 1/\Gamma$ ;  $\omega_p$  is electron plasma frequency with effective mass  $m^* = m_e \frac{n_0}{n_e}$ ;  $n_0$  is electron concentration in valent band;  $n_e$  is free electron concentration;  $-r_s/a_0$  is ratio of sphere radius per on one free electron to its Borovski radius;  $l_s$  is electron free length.

The polyvinylchloride, the dielectric and frequency properties of which are investigated in particular, in work [16] is used in the capacity of dielectric.

The calculated frequency dependences of skin-layer depth for aluminum for case when skin-layer thickness is bigger than free length are presented on fig.16. The normal skin-effect is observed for frequencies of alternating field satisfying to  $\omega\tau \ll 1$ . The frequency region, in which the condition  $1 \ll \omega\tau \ll \omega_p\tau$  is correct, corresponds to relaxation region, the oscillation frequency essentially increases the collision frequency and skin-layer depth stops to depend on frequency. In some region of frequency, the skin-layer thickness can be less than free length, i.e. anomalous skin-effect should be observed [22]. For aluminum at temperature 273°K the weak anomalous skin-effect is seen on Fig.16.

According to work [21] the dispersion relation  $k_s(\omega)$  for all radiation range is obtained solving the following equation [22]:

$$\frac{\varepsilon_1}{k_1} I_0(k_2 a) K_1(k_1 a) - \frac{\varepsilon_2}{k_2} I_1(k_2 a) K_0(k_1 a) = 0$$

where  $a$  is metallic rod diameter;  $I_0, I_1, K_0, K_1$  are Bessel functions of first and second kind;  $k_i = \sqrt{k_s^2 - \frac{\omega^2}{c^2} \varepsilon_i}$ ,  $i=1,2$ .

In low-frequency range at condition that module of complex dielectric constant is bigger than unit (i.e. Leontovich condition is carried out) and consequently, the electromagnetic wave refracted on interface practically normally propagates to the surface, for obtaining of solution of Helmholtz equation we use the expression:

$$k_1 a \frac{K_0(k_1 a)}{K_1(k_1 a)} = i Z_2 \varepsilon_1 \frac{\omega}{c} a,$$

where  $Z_2 = \left( \varepsilon_2 + i \frac{4\pi\sigma_2}{\omega} \right)^{-1/2}$  is active medium impedance.

For HF and SHF ranges the parameter  $Z_2 \frac{\omega}{c} a$  is less than unit. The frequency dependences of propagation factor  $\lambda_1$  and damping coefficient  $\delta_1$  of longitudinal wave are presented on fig.17 on which the low 0.382MHz and top  $6.962 \cdot 10^5$  MHz boundaries of wave existence on frequency are given.

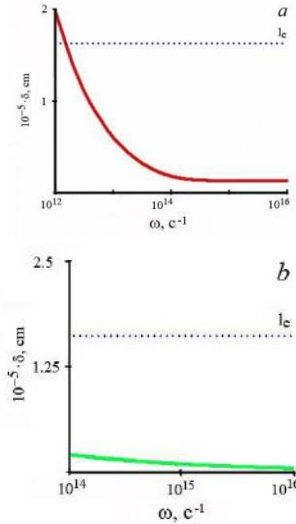


Fig.16. The depth  $\delta$  (a. normal; b. anomalous) of skin-effect for aluminum at 273K.  $l_e$  is free length.

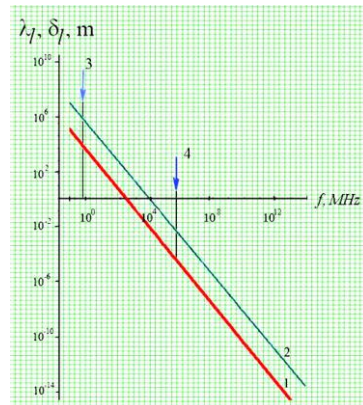


Fig.17. The frequency dependences of propagation factor  $\lambda_1$  of longitudinal wave (1) and damping coefficient  $\delta_1$  of longitudinal wave (2). 3 и 4 are low 0.382MHz and top  $6.962 \cdot 10^5$  MHz boundaries by frequency of wave existence.

The analysis method of non-linear magnetostatic spin waves applied in [4] is developed in works [7-11]. The conclusion about stability condition of surface magnetostatic spin waves relatively longitudinal excitations is one of the results obtained in [6] and further experimentally proved.

In work [12] for investigation of surface magnetostatic waves the ferromagnetic film-dielectric-metal structure where the ferromagnetic film thickness is equal to  $d$  and the dielectric layer thickness is  $t$  is considered and it is accepted that surface magnetostatic wave propagates along  $Y$ -axis, external magnetic field lies in structure plane and is directed along  $Z$  axis. In this case the wave vector has only two components ( $k_y$  and  $k_z$ ) moreover  $k_z \cong 0$ .

The theoretic investigation of instabilities of surface magnetostatic waves are based on results of solution analysis of two-dimension non-linear Schrodinger equation. Taking into consideration the approximations [12] it has the form:

$$i \left( \frac{\partial \phi}{\partial \tau} + v_g \frac{\partial \phi}{\partial y} \right) + \frac{\beta_2^{\parallel}}{2} \frac{\partial^2 \phi}{\partial y^2} + \beta_2^{\perp} \frac{\partial^2 \phi}{\partial z^2} - N |\phi|^2 \phi = 0$$

where  $v_g = \frac{d\omega}{dk}$  is group velocity;  $\beta_2^{\parallel} = \frac{d^2\omega(k_y, 0)}{dk_y^2}$  is group velocity dispersion;  $\beta_2^{\perp} = \left[ \frac{d^2\omega(k_y, k_z)}{dk_z^2} \right]_{k_z=0}$  is coefficient taking into consideration the diffraction;  $N = \left[ \frac{d\omega}{d|\phi|^2} \right]_{|\phi|=0}$  is nonlinearity coefficient;  $\phi(y, z, t)$  is slowly changing amplitude of carrier wave  $e^{i(k_y y + k_z z - i\omega_0 t)}$ ;  $\omega$  is frequency. Note that  $v_g$ ,  $\beta_2^{\parallel}$ ,  $\beta_2^{\perp}$  are obtained from solution of linear dispersion equation.

$$\beta_2^{\perp} = \left[ \frac{d^2\omega(k_y, k_z)}{dk_z^2} \right]_{k_z=0} = - \left\{ \frac{1 + \mu + [1 + \mu + \alpha(\mu + \mu_a - 1)] - tak(\mu^2 - \mu_a^2 + 2\mu_a - 1) \tanh(kd) + \frac{dk}{2\mu} [\mu^2 - \mu_a^2 + 1 + \alpha(\mu^2 - \mu_a^2 + 2\mu_a - 1) [1 - \tanh^2(kd)]]}{\frac{k^2}{\omega_m \omega_h \omega} \{ 2(\mu - 1)\omega^2 + [2\mu(\mu - 1)^2 \omega^2 (1 + \alpha) - \mu_a \omega_h (\omega_m + 2\omega \mu_a) [\mu_a - \alpha(1 - \mu_a)]] \tanh(kd) \}} \right\}$$

For other coefficients nonlinear Schrodinger equation at  $k_z = 0$  transforms to the following form:

$$e^{-2kd} = \frac{(\mu - \mu_a + 1)[\mu + \mu_a + th(kt)]}{(\mu + \mu_a - 1)[\mu - \mu_a - th(kt)]}$$

From this it follows :

$$\omega = \frac{\omega_m}{4} \alpha (1 - \beta) + \frac{1}{4} \{ [2(\omega_m + 2\omega_h) + \omega_m \alpha (1 - \beta)]^2 - 4\omega_m^2 \beta \}^{1/2},$$

and, further the wave group velocity ( $\alpha = e^{-2kt}$ ;  $\beta = e^{-2kd}$ ):

For consideration structure as is shown in work [12], this equation has the form:

$$2kk_f \mu + [\mu^2 k_f^2 - \mu_a^2 k_y^2 + k^2 + \alpha(\mu^2 k_f^2 - \mu_a^2 k_y^2 - k^2 + 2kk_f \mu \tanh kfd) = 0,$$

where  $k^2 = k_y^2 + k_z^2$ ;  $k_f^2 = k_y^2 + \frac{k_z^2}{\mu}$ ;  $\alpha = e^{-2kt}$ ;  $\mu$  and  $\mu_a$  are diagonal and non-diagonal components of magnetic permeability tensor. Taking into consideration the component  $\mu$  and  $\mu_a$  are defined by formulas.

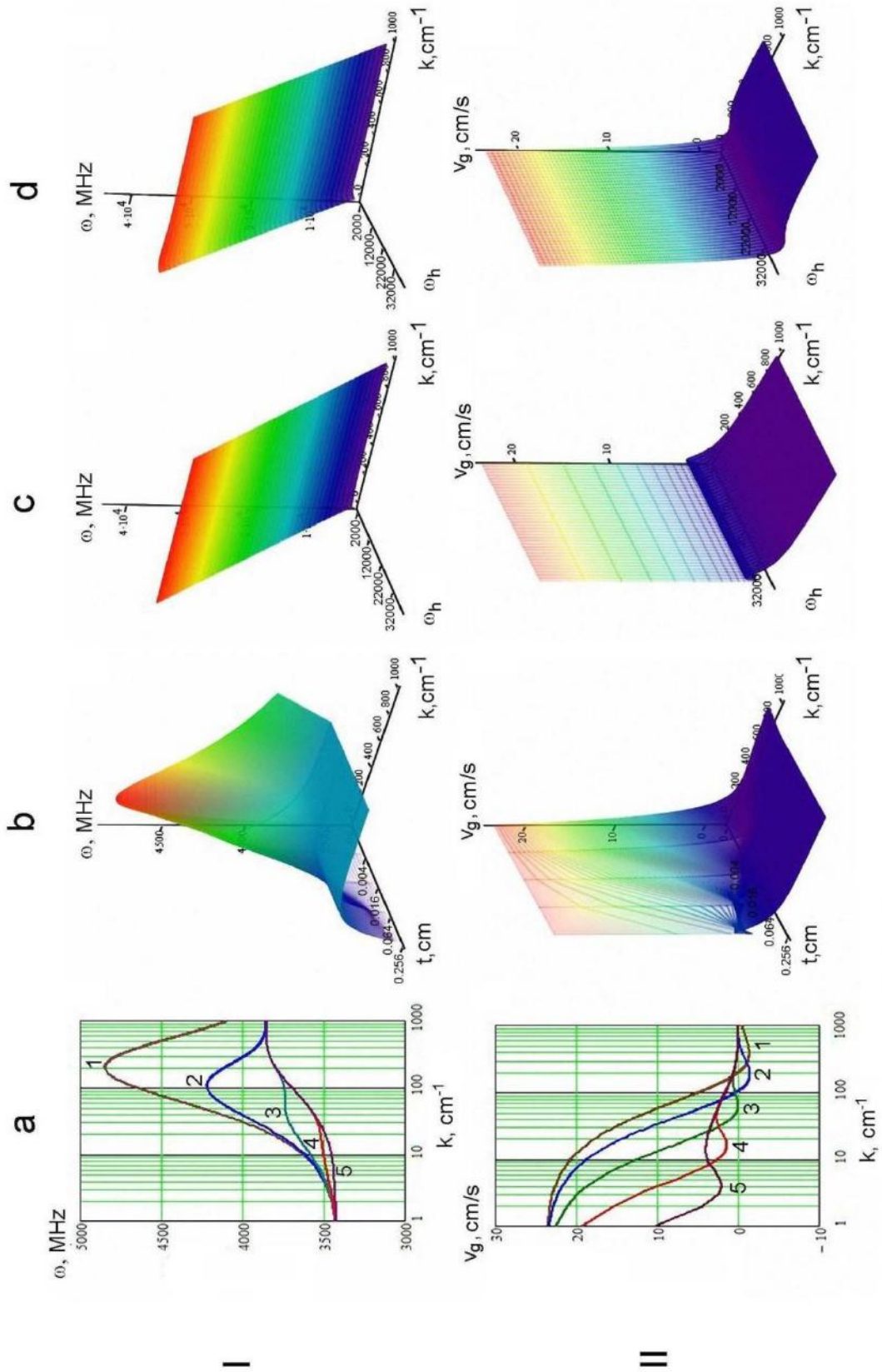
$$\mu(\omega, y) = 1 - \frac{\omega_M(y)(\omega_h + iv)}{\omega^2 - (\omega_h + iv)^2};$$

$$\mu_a(\omega, y) = \frac{\omega_M(y)\omega}{\omega^2 - (\omega_h + iv)^2}$$

where  $\nu$  is relaxation frequency defining the magnetic losses in ferrite;  $\omega_M(y)$  is frequency magnetization precession. It is supposed that frequency precession heterogeneity is defined by linear law  $\omega_M(y) = \omega_m(1 - |1 - 2y|)$ ; parabolic law  $\omega_M(y) = 4y\omega_m(1 - y)$ . Further,  $\omega_m = 4\pi\gamma M_0$ ,  $4\pi M_0$  is ferromagnetic saturation magnetization,  $\omega_h = \gamma H$ ,  $\gamma$  is gyromagnetic relation.

The condition of instability appearance of magnetostatic spin wave (Lighthill condition [6]) has the form:  $\beta_2^{\perp} \cdot N < 0$ . By other words, the instability appearance is defined by group velocity of magnetostatic spin wave. The change of group velocity dispersion can be carried out by change of dielectric layer thickness between ferrite and metallic layers.

From work [12] it follows:



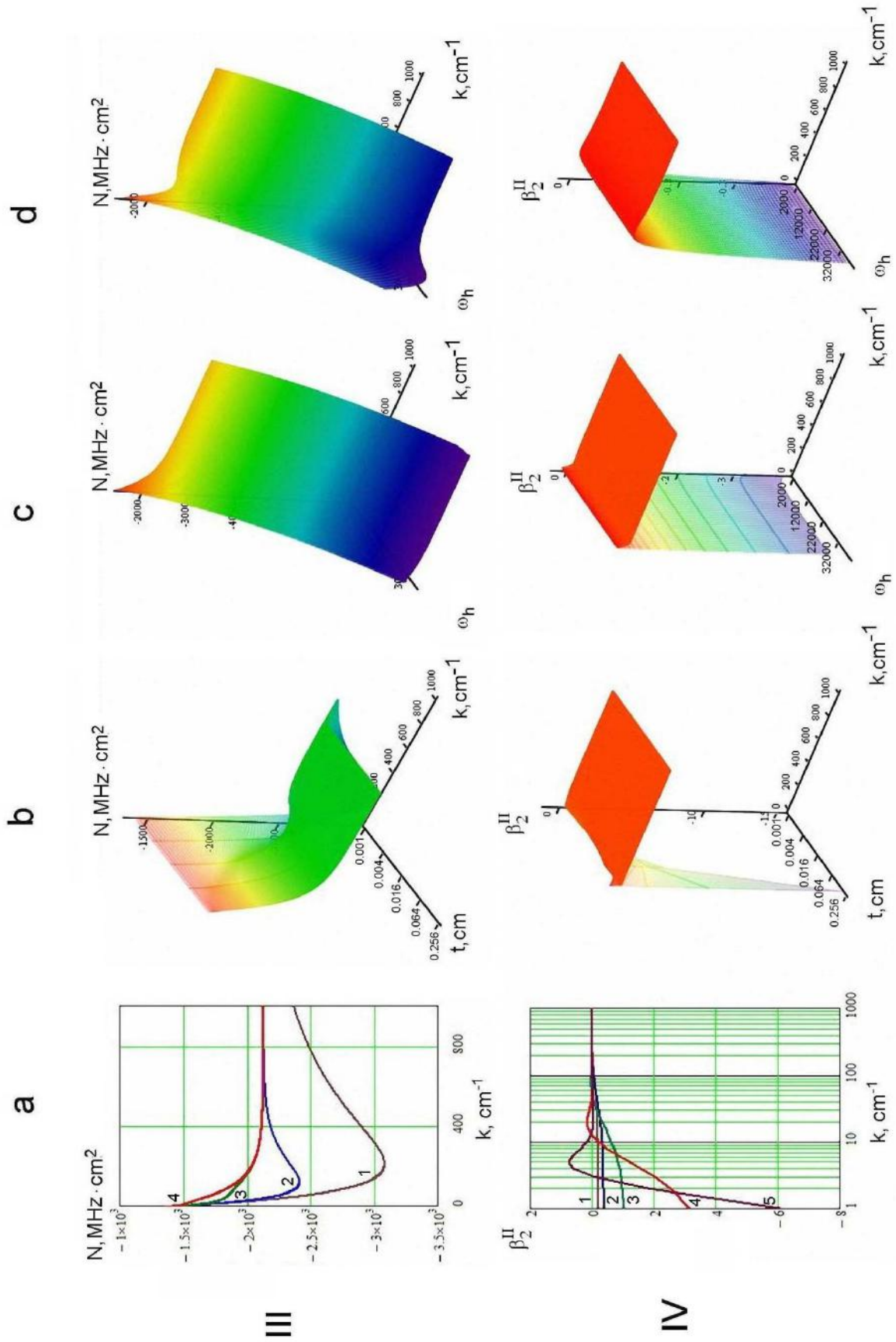


Fig.18. (continuation)

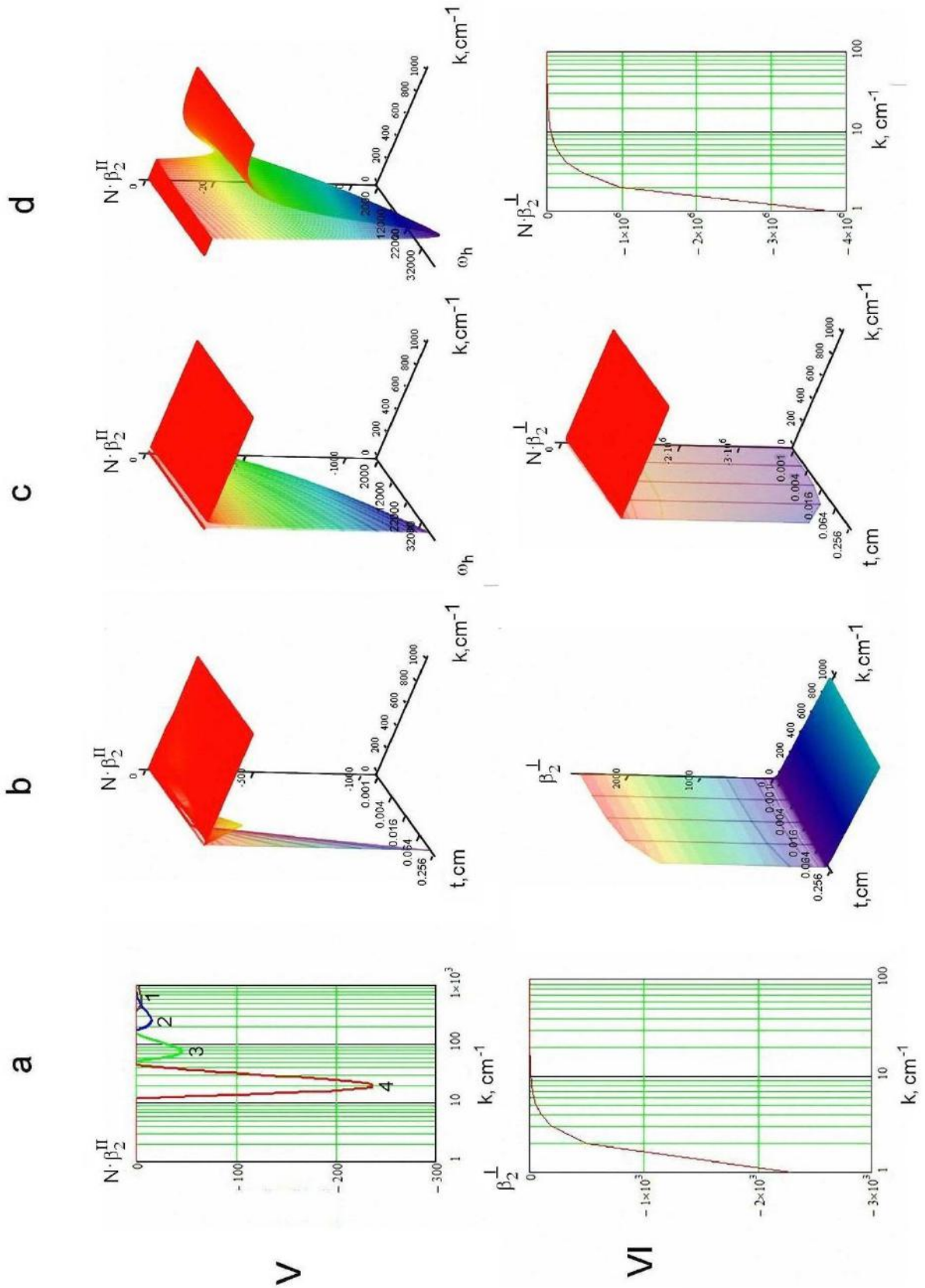


Fig.18. (continuation)

$$v_g = \frac{d\omega}{dk} = -\frac{\omega_m}{2} [t - (t+d)\beta]\alpha - \frac{\omega_m}{2} \{ [t - (t+d)\beta]\alpha((2(\omega_m + 2\omega_h) + \omega_m\alpha(1-\beta))^2 - 4\omega_m^2\beta) - 2\omega_m d\beta \} / \{ (2(\omega_m + 2\omega_h) + \omega_m\alpha(1-\beta))^2 - 4\omega_m^2\beta \}^{1/2}$$

Dispersion of wave group velocity is as follows:

$$\beta_2^{\parallel} = \frac{d^2\omega}{dk^2} = \omega_m [t^2 - (t+d)^2\beta]\alpha + \omega_m \{ (2(\omega_m + 2\omega_h) + \omega_m\alpha(1-\beta))^2 - 4\omega_m^2\beta \}^{-3/2} \cdot \{ (((2(\omega_m + 2\omega_h) + \omega_m\alpha(1-\beta))^2 - 4\omega_m^2\beta)[(2(\omega_m + 2\omega_h) + \omega_m\alpha(1-\beta))[t^2 - (t+d)^2\beta]\alpha + \omega_m [t - (t+d)\beta]^2\alpha^2 - 4\omega_m d^2\beta] \omega_m ((2(\omega_m + 2\omega_h) + \omega_m\alpha(1-\beta))[t - (t+d)\beta]\alpha - 2\omega_m d\beta)^2 \}$$

Denoting  $M_z = M_0 [1 - (|m_x|^2 + |m_y|^2)/2M_0^2]$  in the limit  $kd \ll 1, M_z \approx M_0 - M_0|\phi|^2$  and  $\omega_m \approx (1 - |\phi|^2)$  we obtain

$$\left. \frac{d\omega}{d|\phi|^2} \right|_{\phi=0} = -\frac{\omega_m}{4}\alpha(1-\beta) - \frac{\left\{ \omega_m\omega_h[2 + \alpha(1-\beta)] + \frac{\omega_m^2}{4}[(2+\alpha)^2 - \beta\alpha^2](1-\beta) \right\}}{2\left\{ \frac{\omega_m^2}{4}[(2+\alpha)^2 - \beta\alpha^2](1-\beta) + 2\omega_m\omega_h[2 + \alpha(1-\beta)] \right\}^{1/2}}$$

The results of theoretical calculations of surface magnetostatic wave characteristics (SMW) in Ni-Zn structure ferrite-dielectric-aluminum are given on fig.18.

The dependences of frequency  $\omega$ , wave group velocity  $v_g$ , nonlinearity coefficient  $N$ , group velocity dispersion  $\beta_2^{\parallel}$ , magnetostatic wave instability coefficient  $N\beta_2^{\parallel}$ , diffraction coefficient  $\beta_2^{\perp}$  on wave vector  $k$  and dielectric layer thickness  $t$  correspondingly are given in I, II, III, IV, V, VI lines.

The function plots shown in “a” column are presented in column “b” in three-dimensional form. The dependences of functions on external magnetic field strength for the thicknesses of dielectric layers 3 and 1 correspondingly are given in columns “c”, “b” in I, II, III, IV, V lines. The instability of magnetostatic wave appearance  $N\beta_2^{\perp}$  is given in three-dimensional and usual forms in “c”, “d” columns of VI lines. 1, 2, 3, 4, 5 are dielectric layer thicknesses: 0.001, 0.004, 0.016, 0.064, 0.256 cm.

- 
- |   |   |
|---|---|
| <p>[1] J.W. Boyle, A.D. Boardman, J.G. Booth, K.Booth, S.A. Nikitov. Phys. Rev.B, 1996, v. 53, №18, p.12173-12181</p> <p>[2] Burkard Hillebrands, Kamel Ounadjela. Spin Dynamics in Confined Magnetic Structures I, Topics in applied physics, ISSN 0303-4216; v. 83, Springer-Verlag Berlin Heidelberg New York, 2002, 363p.</p> <p>[3] Andrei N. Slavin, Sergei O. Demokritov, and Burkard Hillebrands Nonlinear Spin waves in One and Two-Dimensional Magnetic Waveguides, Springer-Verlag Berlin Heidelberg 2002, p.35-66</p> <p>[4] A.K. Zvezdin and A.F. Popkov, Sov. Phys. JETP, 2 (1983), 350; JETP 1983, 84,606-615 (in Russian).</p> <p>[5] A.K. Zvezdin and A.F. Popkov. Pisma v JETP, t.39, vip.8, s.348-351, 1984. (in Russian)</p> <p>[6] V.I. Karpman. Nelineyniye volni v dispergiruyushih sredakh, M.: Nauka, 1973, 175p. (In Russian)</p> <p>[7] A.D. Boardman, S.A. Nikitov. Phys.Rev B, 1988, v.38, p.11444-11451.</p> <p>[8] A.D. Boardman, Yu.V. Gulyayev, S.A. Nikitov JETP. 1989. t.95. №6. s.2140-2150. (in Russian)</p> <p>[9] A.D. Boardman, S.A. Nikitov, N.A. Waby Phys.Rev. B, 1993, v.48, pp. 15436-15441.</p> <p>[10] A.D. Boardman, Q. Wang, S.A. Nikitov, J. Shen, W. Chen, D.L.Mills, J. Bao. Nonlinear Magnetostatic Surface Waves in Ferromagnetic Films. IEEE Trans. on Magnetics. v.MAG-30, No.1, pp.1-13, 1994.</p> | <p>[11] A.D. Boardman, S.A. Nikitov, K. Xie, H. Mehta. Bright Magnetostatic Spin-Wave Envelope Solitons in Ferromagnetic Films // J. Magn. Mater.1995. V. 145. No 2, p357-378.</p> <p>[12] A.S. Kindyak. O Solitonax poverxnostoy maqnitostaticheskoy spinovoy volni v ctrukture ferrit-dielektrik-metall. Pisma v JTF, 1999, t.25, vip.4 s.48-54. (in Russian)</p> <p>[13] A.S. Kindyak. Neleynie poverxnochnie manitostaticheskie volni v ferrit-poluprovodnikovoy strukture // JTF. 1999. t. 69. v. 6. s. 119.(in Russian)</p> <p>[14] Yu.P. Sharaevskiy, M.A. Malyuqina, E.V. Yarovaya. Pisma JTF, 2006,t.32, v. 3, s.33-39. (in Russian)</p> <p>[15] V.P. Lukomskiy. Ukr.fiz.jurn. 1978, t.23, №1, s.134-139. (in Russian)</p> <p>[16] A.O. Korotkevich, S.A. Nikitov. JTF, 1999, t.116, v.6(12), s.2058-2068.(in Russian)</p> <p>[17] A.V. Kokin, S.A. Nikitov. Vliyanie neprerivnoy nakachki na rasprostranenie solitonov oqibayushey maqnitostaticheskix spinovix voln, FTT, 2001, t.43, v.5, s.851-854. (in Russian)</p> <p>[18] M.A. Malyuqina, Yu.P. Sharaevskiy. Izv. Vuzov. Prikladnaya nelineynaya dinamika, 2000, t.8, №3, s.59-69. (in Russian)</p> <p>[19] Q.M. Dudko, M.A. Malyuqina, Yu.P. Sharaevskiy. , Izv. Vuzov. Prikladnaya nelineynaya dinamika, 2003, t.11, №6, s, s.116-129. (in Russian)</p> |
|---|---|

- [20] A.D. Bordman, K. Xie. Magneto optic spatial solitons, Phys.Rev.Lett., 1995, v.75,n.25, p.4591
- [21] R. Marcelli, S.A. Nikitov. Magnetostatic Surface Wave Solitons Induced by Cross-Phase Modulation, Europhys. Lett., 2001, v.54, n.1, p.91-97
- [22] B.A. Knyazev, A.V. Kuzmin. Poverhnostniye elektromagnitniye volni: osnovnie svoystva, formirovanie, transportirovka, IYAF im. G.I. Budkera SO RAN, Novosibirsk, 2003, 26p. (In Russian)
- [23] Kandasamy Velmurugana, Vellaiyappan Sangli Karuppanan, Venkatachalapathyb, Sechassalom Sendhilmathanc, Synthesis of Nickel Zinc Iron Nanoparticles by Coprecipitation, Technique Materials Research, 2010, 13(3), p.299-303.
- [24] B.R. Churagulov, A.A. Burukhin, N.N. Oleynikov, P.E. Meskin. Synthesis of nanocrystalline nickel-zinc ferrites under hydrothermal conditions, Proceedings of the Joint Sixth International Symposium on Hydrothermal Reactions and Fourth Conference on Solvo-Thermal Reactions, Kochi, Japan, 25-28 July, 2000, pp.553-556.
- [25] Sh.N. Aliyeva. The magnetic properties of  $Zn_xNi_{1-x}Fe_2O_4$  solid solution, Fizika, № 1, vol. XVII, 2011, pp.6-9.
- [26] T.R. Mehdiyev, A.M. Gashimov, N.R. Babayeva, A.A. Habibzade. AJP Fizika, 2008, v. XIV, №3, p.207. (in Russian)
- [27] A.H. Habibzade, S.I. Aliyeva, Sh.N. Aliyeva, T.R. Mekhtiyev. Thermodynamic parameters of solid solutions of  $NiFe_2O_4$ - $ZnFe_2O_4$  system, . AJP Fizika, 2011, v. XVII, №4, p.14-19
- [28] L. Neel and P. Brochet. Comptes Rendus, 230, 280—282 (1950)
- [29] UFN, 1955, vol. LVII, № 2, p. 279, 1955
- [30] E.I. Kondorskiy. Izv. AN USSR, ser. physical, 1952, v.16, p.398 (in Russian)
- [31] A.B. Rinkevich, V.V. Ustinov, M.I. Samoylovich, A.F. Belyanin, S.M. Klesheva, E.A. Kuznetsov. Tekhnologiya i konstruirovaniye elektronnoy apparaturi, 2008, №4b, p.55 (In Russian)
- [32] Charles P. Poole. Electron spin resonance, 1967, 557p.
- [33] Zhou Xin, Hou Zhi-Ling, Ling Feng, Qi Xin. Magnetic properties of Ni-Zn ferrite prepared with layered precursor method, Chin Phys. Lett., vol.27, No2, 2010, p. 117501-1-117501-4
- [34] A. Kudashov. Izuchenie zavisimosti radioploshayushix svoystv ferritovix materialov v zavisimosti ot maqnitnoy pronichamosti obrazcha. Aktualnie problem elektroniki. Materiali II vnutrivuzovskoy molodejnoj nauchnoy shkoli, april 2011q, Kuznechk, Rossiya, r.59-63. (in Russian)
- [35] Ismayadi Ismail and Mansur Hashim. Structural and magnetic properties evaluation of fine-grained  $Ni_{0.5}Zn_{0.5}Fe_2O_4$  series synthesized via mechanical alloying, Australian J. of Basic and Applied Sciences, 5(11), p.1865-1877, 2011
- [36] Q.Yu. Yurkov, S.P. Qubin, D.A. Pankratov, Yu.K. Koksharev, A.V. Kozinkin, Yu.I. Spichkin, T.I. Nedoseykina, I.V. Piroq, V.Q. Vlasenko. Nanochastichi oksida jeleza (Sh) v matriche polietilena. Neorqanicheskie materialy. 2002, t.38, №2, s.186-195. (in Russian)
- [37] V.K. Sharma, F. Waldner. Superparamagnetic and Ferri-magnetic Resonance of Ultrafine  $Fe_3O_4$  Particles in Fer-rofluids // J. Appl. Phys. 1977. V. 48. № 10. P. 4298-III1.
- [38] R.S. De Biasi, T.C. Devezas. Anisotropy Field of Small Magnetic Particles as Measured by Resonance // J. Appl. Phys. 1977. V. 49. № 4. P. 2466-2470.
- [39] Yu.A. Koksharov, D.A. Pankratov, S.P. Gubin et al. Electron Paramagnetic Resonance of Ferrite Nanoparticles // J. Appl. Phys. 2001. V. 89. № 4. P. 2293-2298.
- [40] Nagata K., Ishihara A. ESR of Ultrafine Magnetic Particles // J. Magn. Mater. 1992. V. 104-107. P.1571-1573.

Received: 06.06.2012

## NANO-FRACTAL STRUCTURES ON (0001) VAN-DER-WAALS SURFACE OF $A^V_2B^{VI}_3$ CRYSTALS

F.K. ALESKEROV<sup>1</sup>, S.A. NASIBOVA<sup>1</sup>, R.M. TAGIYEV<sup>2</sup>, A.Sh. KAKHRAMANOV<sup>3</sup>

<sup>1</sup>SSC «Selenium» of ANAS

<sup>2</sup>Gandja regional center of ANAS (Gandja, Azerbaijan)

<sup>3</sup>Baku State University

The formation of fractal structures as a result of heat flow action on atom mass transfer in  $Te^{(I)}-Te^{(I)}A_2^VB_3^{VI}$  layers is investigated. It is established that diffusion process is the effective source of fractal nano-objects. The results obtained in the work add the picture of phenomena and processes on (0001)  $A^V_2B^{VI}_3$  surface and show the use suitability of fractal conceptions for interlayer nano-islands and goffered nano-formations.

**Keywords:** nano-fractal structures, quantum dots.

**PACS:** 05.65.+b, 52.77.Dq

The interest to investigations of interlayer nano-fragments is connected with obtaining and studying of nano-clusters. The cluster construction in mesoscopic structures of different degree of order takes place as a result of intercalation between  $Te^{(I)}-Te^{(I)}A_2^VB_3^{VI}$  layers besides the formation of the clusters. The physics of this process and its control presents the interest from the controlled obtaining of such structures point of view.

The application of the similar conception and methods in the different fields is the characteristic of the modern scientific investigation. The fractals and percolation the use of which at the analysis of experimental results is the approach peculiarity to investigation of nano-structured layered crystals, developed in the article, are related to conceptions having the general scientific value.

The obtaining of nano-structured crystals  $Sb_2Te_3(Bi_2Te_3)$  <impurity> and formation of fractal structures at intercalation and their composites is the aim of the given work.

Last years the relation to nonsmooth functions (or non-regular sets) has changed as they provide significantly better presentation of many physical phenomena than those which give the objects of classic geometry. The fractal geometry is connected with the study of such irregular sets. The fractals are the main object of the fractal geometry. The fractal is the geometric figure in which the one and the same fragment repeats at each scale decrease. The fractals having these properties and obtaining as a result of simple recursive procedure (combination of linear transformations) are called *constructive fractals*. Thus, *constructive fractal* is the set obtaining as a result of linear (affine) contractive mappings of the similarity. The resultant contractive mapping has the stable "point" (fractal).

### RICHARDSON EXPERIMENT.

We chose the small unit of measurement "a", ruler. Further, we measure the curve length consisted from equal sections of "a" length. If ruler is used N times so general measuring length is equal to N a. Later, in the correspondence with Mandelborg definition, the curve "fractal dimension" is equal to:

$$D = \lim_{a \rightarrow 0} \frac{\lg N}{\lg \frac{1}{a}} \quad (1)$$

Let's D is curve (boundary) "bending degree". You can see more detail definition of fractal dimension and other "nonintegral" dimensions in [1].

In some cases the fraction has the constant values on each step. Then

$$D = \frac{\lg N}{\lg \frac{1}{a}} \quad (2)$$

### KOCH CURVE

Koch gives example of the curve which has the tangent anywhere.

Koch curve is self-similar: each its part is the mini-copy of the whole one.

In conclusion let's give the popular fractal models in physics:

In physics there are many problems connected with behavior of complex systems have the deep analogies or with percolation phenomena (percolation) or fractal growth on different models [1-3]. The interest has been risen with transition to nano-objects and nano-world problems that has led to new physical and geometric approaches. This is quite wide one: almost all objects of real world are under its influence [1,4].

### FRACTAL CLUSTERS [2]

The fractal cluster or fractal aggregate is the one of the objects with fractal structure. For comparison let's consider the other physical object with fractal properties which is the percolation cluster.

### THE GEOMETRIC FRACTAL SYSTEM PROPERTIES.

The fractal clusters have the general properties of fractal systems which are comfortable demonstrated on example of fractal polygonal curve consisted of wire with elements of identical length. For this the wire is divided on big number of identical sections of length a and these are numbered; Koch figure is constructed from the wire. The correlation function is introduced:

$$C(r) = \frac{1}{N} \sum_i \rho(r_i) \rho(r_i + r) = \frac{\langle \rho(r) \rho(r+r) \rangle}{\langle \rho(r) \rangle} \quad (3)$$

here  $N$  is section number,  $i$  is number of  $i$ -th section,  $\rho$  is density the value of which is equal to unit in the occupied point and zero in the point doesn't taken by wire. Further, at cluster consideration the wire sections are exchanged by particles from which it is consisted in. If we destroy the right structure of Koch figure and average in formula (3) on  $r$  vector direction then correlation function will correspond to wire average density on  $r$  distance from occupied points. As wire mass in  $r$  radius sphere taken from occupied point ( $r \gg a$ ) is proportional to  $r^D$  then average density on this distance is proportional to  $r^{D-d}$  (here  $d$  is space dimension in which the wire is put). Thus, correlation function has the form:

$$C(r) = \text{const}/r^a \quad (4)$$

Moreover,  $r$  is bigger than the length of minimum line structure and

$$Da = d - a \quad (5)$$

The fractal cluster consists of set of "glued" particles the dimensions of which are significantly less than cluster dimensions.

The existing models of fractal cluster construction in the dependence on physical conditions at which it is carried out, one can divide on following properties: 1) process character (cluster –particle or cluster-cluster); 2) the character of particle motion or clusters (rectilinear or Brownian movements); 3) union character of particles or clusters in the dependence on coalescence probability at their touch.

The process character depends on real physical conditions. In some cases the cluster growth process takes place in the result on attachment of separate particles to it, in other cases on first stage process there are many particles which are united in small clusters and those are united in big ones. Thus, finally the fractal cluster is constructed. Moreover, its compactness and physical properties depend on both particle motion character in the space and on coalescence probability of particles and clusters at their touch.

In simple form Vitten-Sander model can be described in 2D space in following form. The limited 2D space is divided on set of quadratic cells; the one particle is put in it. Each new particle shifts to neighbor cell spontaneously; its way is chosen by Monte-Karlo method. If particle achieves space boundary then it reflects from it. The particle motion continues up to the moment it is near to one of the cluster particle. Then it stops and fixes in the given cell and the following particle is entered in the space. The fractal cluster is grown up by this way. Vitten-Sander model gives the simple method of fractal cluster formation. These models we can use for revealing of cluster union process character in nano-particles and their motion in  $\text{Te}^{(1)}$ -  $\text{Te}^{(1)}$   $\text{A}_2\text{V}_3\text{B}_3^{\text{VI}}$  space. Moreover, it is necessary to study the morphological peculiarities of nano-fractal structure formation on (0001) surface in  $\text{A}_2\text{V}_3\text{B}_3^{\text{VI}}$ .

The relief of interlayer real surface can have fractal geometry [4]. The fractal dimension  $D_f > 2.5$  of the relief is defined both doped surface nature and treatment type, much exceeds its topological dimension  $D_t = 2$ . The relief fractality leads to increase of factual area of  $S_{\text{fact}}$  surface which can significantly exceeds the topological area. According to this, the carrying of investigation directed on study of potential heterogeneity and character of its distribution on fractal relief of semiconductor surface  $\text{A}_2\text{V}_3\text{B}_3^{\text{VI}}$  presents interest.

The works [5-6] with the use of the conception of fractal Brownian surfaces can serves as example: the geometry of potential surface relief of high-doped substrate  $n^+$ -GaAs(100) is investigated and the value of its fractal dimension is defined.

The quantitative evaluation method of order of degree of nano-dimension structures on the base of fractal dimension analysis of AFM data and X-radiation scattering one [8] is proposed in [7].

The interest to formation of structures with element dimensions in nanometer region (for example, quantum point system) and big concentration density of such elements ( $\sim 10^{11}$ - $10^{12}$   $\text{sm}^{-2}$ ) reveals in last years in the connection of revealing in such systems of quantum-dimension effects.

In the result of numerical experiments it is mentioned that at simultaneous attachment of big amount objects the fractal dimension change is bigger than at attachment of small amount of elements. This fact allows us to make conclusion about order or disorder of the system as a whole [8-9].

## THE PROCEDURE OF FRACTAL DIMENSION MEASUREMENT [10,11,12]

The measurements are carried out with the use of scanning probe microscope (SPM).

The investigated methods are enough sensitive ones to the change of relief structure presented in the form of definite numerical series and allow us to quantitatively evaluate its topological complexity. However, the application of such methods requires the additional treatment of analyzed data. There are three dimension types connected with self-affine surface: the surface dimension  $D_{\text{surf}}$  which is local self-affine surface; the profile dimension  $D_{\text{pr}}$  which is also local and self-affine one; contour dimension  $D_c$  which is self-similar dimension. These fractal dimensions are connected with each other by the relation:  $D_{\text{pr}} = D_c = D_{\text{surf}} - 1$ . Для  $D_c = D_{\text{surf}} - 1 = 2.5 - 1 = 1.5$ .

The comparison of AFM-images  $\text{Bi}_2\text{Te}_3$ -In, Cu, Ag obtained by us with landscapes constructed with the help of Foss and Mikin algorithms allows us to accept the nano-fragment fractality including the fractal surface self-affinity. The close and similar pictures are observed at Herst index  $H=0.7$  that gives the fractal dimension which is equal to  $D=3-H=2,3$ .

Let's compare the data for  $D = 2.5$  structures with results [1,7] on fractal dimension of particles (clusters) forming at solid particle association.

In known aggregation model [1-2] characterizing Brownian motion with taking under consideration cluster or particles it is established that associating particles are in the diffusion motion in the space, i.e. particle path

length is small in this case in the comparison with region character dimensions responsible for fractal growth. The investigation results for average values of fractal dimensions at particle association in 3D space (in aggregation model of Brownian motion) give  $D = 2,46 \pm 0,05$  value; for 2D space  $D_f = 1,68 \pm 0,02$  is obtained.

The other models are also known, in particular, fractal cluster growth model on the substrate, when cluster penetrates at adhesion of solid particles to substrate. In models proposed in [1,2] it is accepted that growing 3D cluster forms on plane substrate. In this case the cluster transversal dimension is significantly less than substrate dimensions and attachable particles are in the motion in the space, i.e. clusters penetrate from the plane.

## EXPERIMENTAL PART AND ITS DISCUSSION EXPERIMENT TECHNIQUE

The crystal cleaving along basal plane is carried out directly before experiment. Because of the present of layered structure such crystals are easily cleaved on the planes (0001) which are called cleavage plane.

There is set of effective control methods of the structure, composition and relief of the surface. These are methods of atomic force microscopy and roentgen-diffractometry on the nano-level of (0001)  $A_2^V B_3^{VI}$  <impurity> surface.

The electron-microscopic images are obtained on AFM by NC-AFM mark which allows the obtaining of not only 3D but also 2D image of crystal surface (0001). The sample relief with nano-fractal formations doped by impurities: indium, cuprum, bore are studied on scanning AFM by NC-AFM mark.

The preparation of pure surface is carried out by the way of cleaving of crystals and solid solutions of  $Bi_2Te_3 - Bi_2Se_3$  system with impurities on (0001) plane on air directly before the investigation. The study of chemical composition of their surfaces is carried out with the help of X-ray films. The analysis shows the absence of harmful impurity content, particularly, the oxygen in obtained crystals.

The peculiarities of particle aggregation in free space are studied in detail. Our interest is shifted to the side of research of more complex systems the self-organization of which takes place in limited interlayer space. The impurity formations between layers in layered crystals intercalated by diffusion method are such ones. Such nano-formations have the fractal structure (see fig.1-2). The self-organization fractal surfaces with strong boundary of cluster transition (marked by ellipsoid figures) into organized fractal filaments (they are shown by hands in fig.1a,b) is observed. On fig.2c the transition boundary is marked by black line, moreover, the regions are strongly differs. The study results of nano-fractal "ensemble" formation process in  $Bi_2Te_3$ -impurity system on example of  $Bi_2Te_3$ <Cu, In> are given below.

The value of fractal dimensions  $2 < D_f < 3$  which exceeds the value of topological dimension of investigated surface ( $D_f=2$ ) on definition and that's why it is the fractional value, is the main characteristics of 3D fractal surfaces.

The real surfaces can be only self-affine, i.e. they can have the similarity property only in enough narrow interval of measuring scales  $\delta$ . For  $Sb_2Te_3$ <Te> system  $\delta$  value can change up to nano-meter decades.

For obtaining of  $D_f$  nano-fragment surface the triangulation method is used concluding in constituent surface approximation by pyramid series and area measurement of their lateral surfaces, is used. The measurement delicacy of S surface area in the given case depends on quantity of such pyramids (partition number) which is defined by value of measuring scale  $\delta$ .

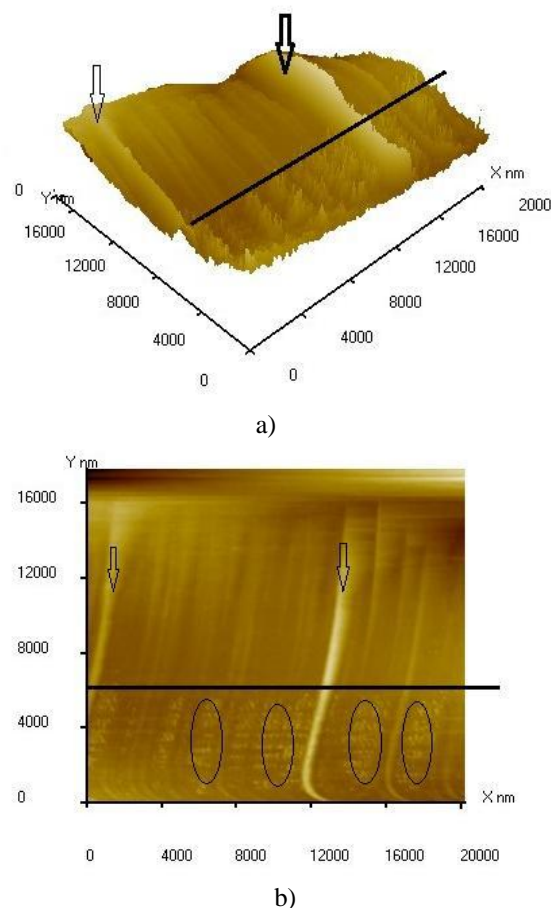
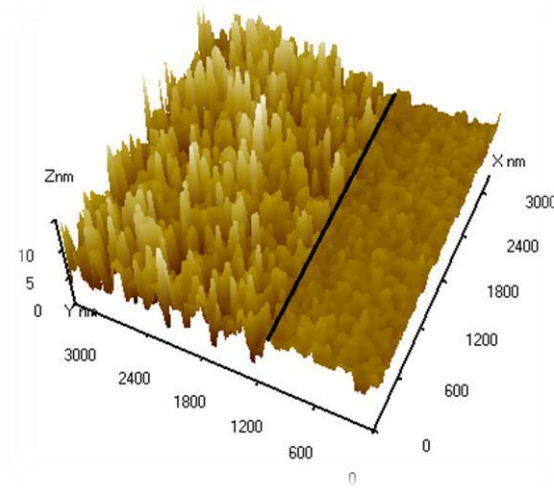


Fig.1. a) AFM-image of surface morphology (0001)  $Bi_2Te_3$ <Cu-B>: a) 3D-image, b) 2D-image.

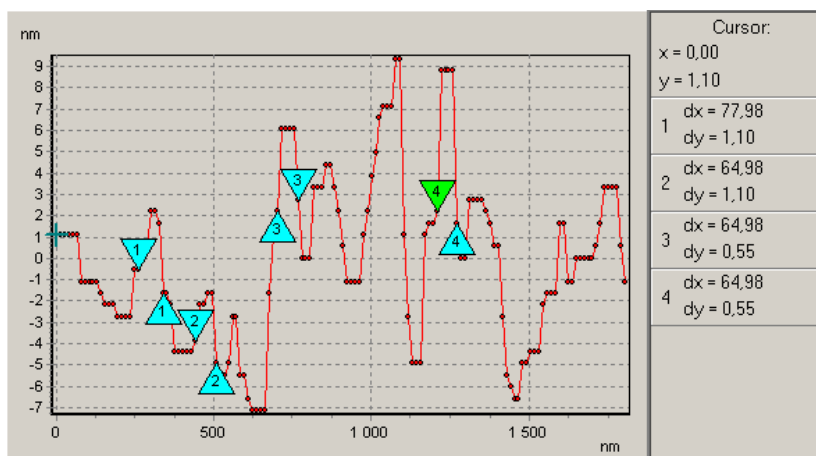
As for fractal (self-affine) surface S and  $\delta$  values are connected by following relation [3,8-10]:

$$S = S_0 \delta^{2-D_f} \quad (6)$$

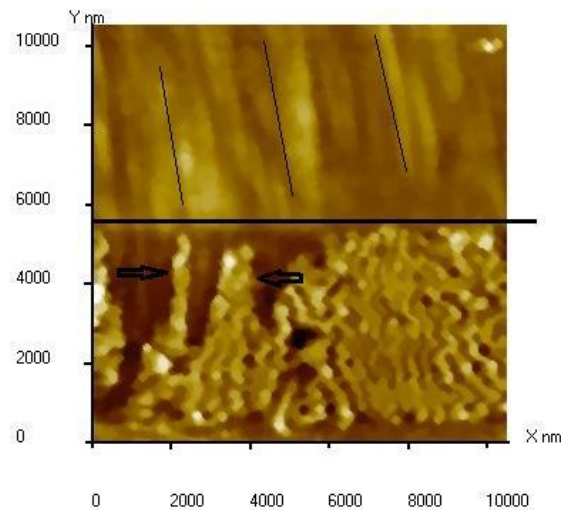
where  $S_0$  is projection area of lateral surface on (x, y)(this plane (0001)  $Sb_2Te_3$ <Te>)) plane, one can easily define  $D_f$  value on incident angle of linear section of  $\ln S = f(\ln \delta)$  dependence. The estimation of fractal dimension value of 2D surface carried out by triangulation method gives  $D_f = 1,85$  value that means the enough developed surface (0001) ( particularly, strongly rough surface) of  $A_2^V B_3^{VI}$  system. The strong surface roughness (0001) leads to significant increase of the area of its surface. So estimations of real surface area made with the use of (6) expression give the value  $20 \mu m^2$  (Fig.2a).



a)

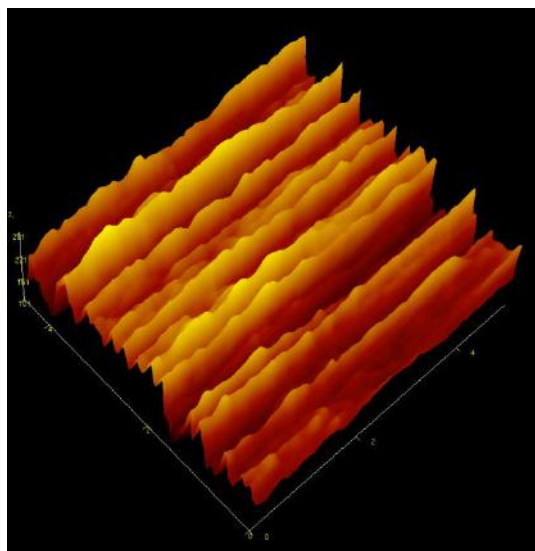


b)

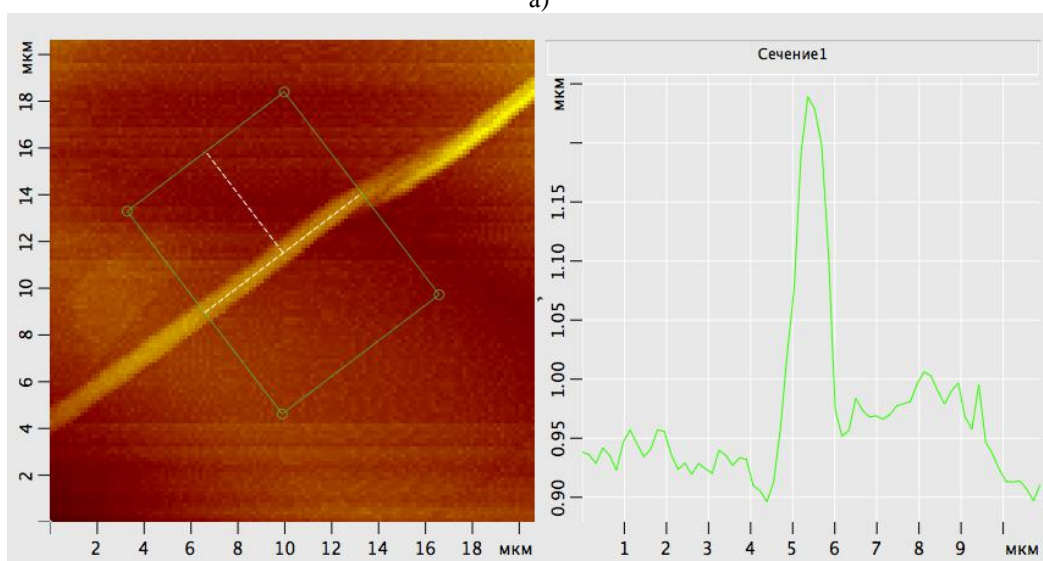


c)

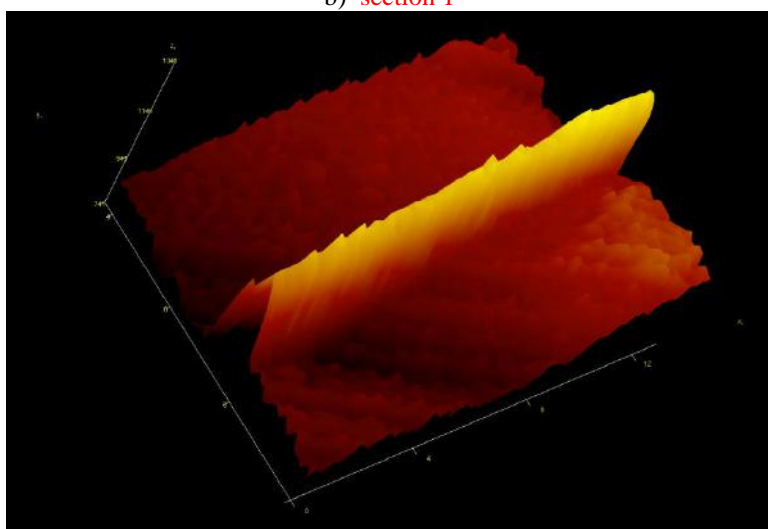
Fig.2. a) AFM- images of (0001)  $\text{Bi}_2\text{Te}_3\langle\text{In}\rangle$  surface, a) the profile along image perpendicular to black line on (fig. A), b) 2D image of (0001) surface.



a)

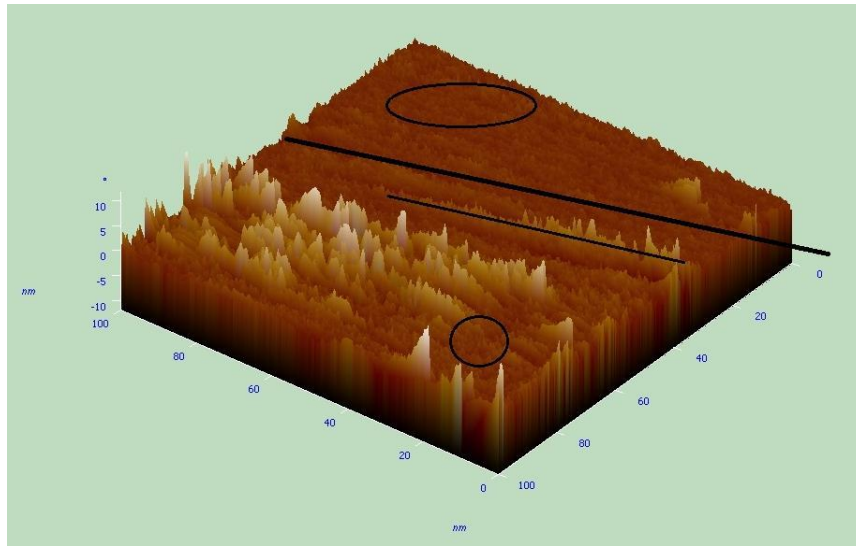


b) section 1

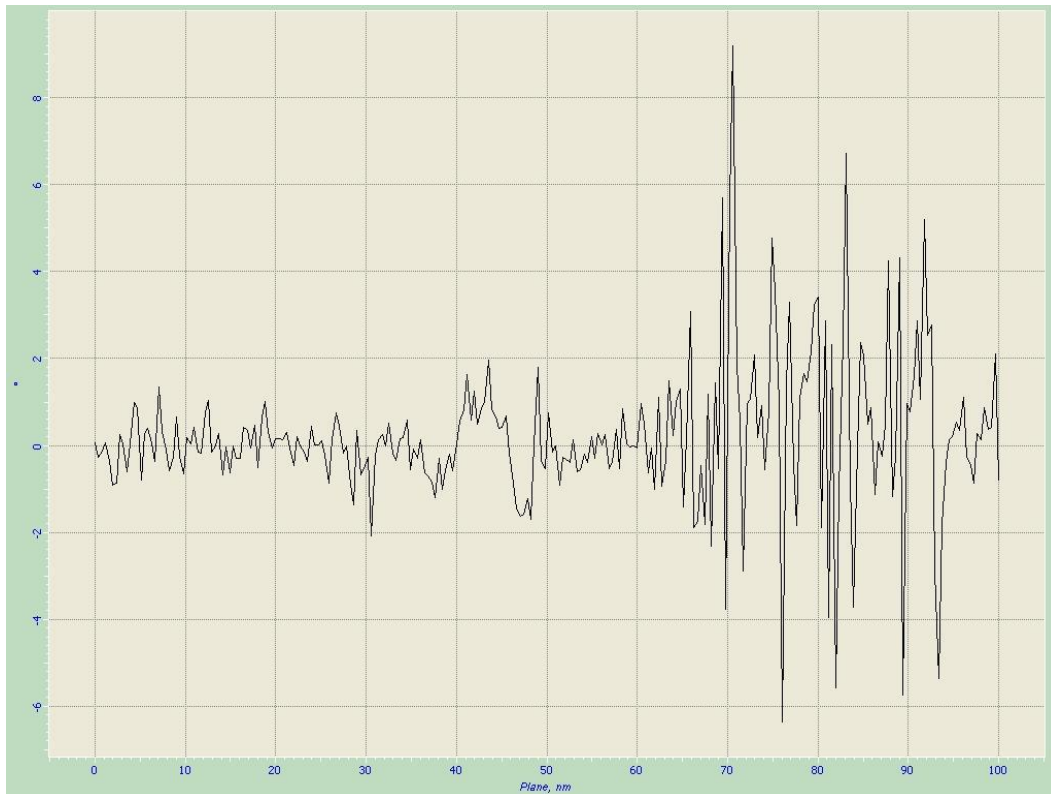


c)

Fig. 3. a) AFM-images (in 3D scale) of (0001)  $\text{Bi}_2\text{Te}_3\langle\text{Cu-B}\rangle$  surface, b) the profile image perpendicular to filament line growth, c) Koch surface fragment (3D scale)



a)



b)

Fig.4. a)AFM-images (3D scale) of (0001)  $Sb_2Te_3<Te>$  surface, b) profile diagram demonstrating the surfaces with different fractal dimensions.

The fractal dimension value of semiconductor surface shows not only value of average value of roughnesses, but the character of their distribution on the surface. The surfaces (0001) given on fig.1 characterize by heterogeneity: roughness average value of the main relief is  $\Delta h \approx 2nm$ . Moreover, its significant part is covered by nano-islands with height up to 10nm and diameter near foundation 50-100nm forming the specific surface with strong transitions of nano-structure dimensions (see fig.1-2). The observable saving the surface relief character at the simultaneous

growth of roughness average level with increase of analyzed area is the reflection of fractal mechanism of surface relief formation (0001)  $A_2^V B_3^{VI} <impurity>$ .

The interlayer nano-particles on (0001)  $Sb_2Te_3<Te>$  surface characterize by fractality features: structural hierarchy, scale invariance and high values of specific interlayer surface (0001).

Let's consider the surfaces in interlayer spaces where impurity fractal structures (fig.4) form. If we cross the horizontal section on the one of the obtained

“picture”, then we will have the images in the form of “island” and “water line”.

The fractal dimension of such lines obtained by surface cross with the plane equal to  $D = 2 - H = 1.5$ . The nonintegral value ( $1 < D < 2$ ) is the evidence of the plane fractal structure.

The nature of fractal structure formation on the free surface and in interlayer space of layered crystals  $Bi_2Te_3$ ,  $Bi_2Te_3<Ag>$  and  $Bi_2Te_3<Cu>$ ,  $Bi_2Te_3<Ni>$ ,  $Bi_2Te_3<B>$ ,  $Bi_2Te_3<Sn>$ ,  $Bi_2Te_3<Cd>$ ,  $Bi_2Te_3<In>$ ,  $Sb_2Te_3<Se>$ ,  $Sb_2Te_3<Cd>$  are analogues ones. The fractal structure of these crystals reveals in distribution properties of impurity layers between telluride quintets  $T_e^{(1)} - T_e^{(1)}$ . For such layers the following situation realizes. The structure fractal properties reveal in scale range limited below by the dimension of order  $\sim (5 - 10)$  nm forming the fractal aggregate and upper limited by dimension of initial fractal clusters (1000)nm. The presence of forming nano-layers and islands prints of different dimensions on them can be seen on the crystal surface planes (0001) on the base of their study. The nano-layer formation in the crystals on  $Bi_2Te_3$  base can be connected with draining of diffused impurity atoms (argentums, cuprum and nickel in very small degree) from telluride quintets  $Te^{(1)} - Te^{(1)}$  and other defects in interlayers. The draining periods of impurity atoms take place gradually: on first stage the number of transited atoms is small one and they take place the small part of interlayer surface, i.e. impurity atoms concentrate in small quantity. With time their concentration achieves the saturation; they form the nano-islands united in nano-particles. The process is accompanied by formation of total layers on which the enlarged ordered islands accumulate. The island general quantity significantly decreases as a result of discrete diffusion particle shift on short space which leads to the fact that islands drain in ordered filaments (fig.1-3).

At bigger resolution it is seen that surface relief  $Sb_2Te_3<impurity>$  forms by the layer of nano-structural elements (NSE) tightly joined to each other. These structures have two well expressed boundaries and relatively big oscillations of the dimensions (on fig.4a these regions are expressed by black lines). It is interesting that corbelled “NSE” on fig.4(a) and regions out of them have the fractal structure with the difference that NSE are collected in 3D formations that emphasize them on the main relief background. Such regions on fig.1b are emphasized by ellipses on the surface.

As a whole, we can say that though the phase contrast interpretation has quality character, he gives the important additional information about geometrical structure of surface formations.

## CONCLUSION

The interlayer nanoobjects having the fractality features and relating to geometrical classification (Koch surface type) are obtained, fractal nature of forming objects reveals in different scales.

In connection of nano-structure formation in semiconductors the fractal nano-structures of less dimensions (5-10nm) obtained by us can present themselves the practice interest and influence on properties of thermoelectric crystals.

The state control of Van-der-Waals surface (0001)  $Sb_2Te_3<Te>$   $Bi_2Te_3<In>$  on nano-level by AFM method reveals the presence of vertically grown fractal objects ( $D_f=1,85$ ) by height from 5 up to 10nm. The investigated parameters agree with data of 3D images with relief profile and fractal density distribution on surface (0001) on the height divided from each other by different hierarchy level. The corrugated structures on surface (0001)  $Bi_2Te_3<Cu-B>$  are experimentally revealed.

- 
- [1] *Jens Feder*. Fractals, Department of Physics University of Oslo, Norway, 1990, p.259
- [2] *B.M. Smirnov*. // Fizika fraktalnih klasterov, I. Nauka, Moskva, 1991, s.134. (in Russian)
- [3] *A.D. Morozov*. // Vvedenie v teoriyu fraktalov. – Moskva-Ijevsk: Institut kompyuternix issledovaniy,2002, 160 str. (in Russian)
- [4] *E.M. Derun, M.Q. Pishkin, F.K. Aleskerov, S.Sh. Kaxramanov*. // J. TRANSACTIONS, (Azerbaydjan).V. XXII, №5, 2007, r.39-43. (in Russian)
- [5] *N.A. Torxov, V.Q. Bojkov*. Fizika I tehnika poluprivodnikov,2009, tom 43, vip.5, s.577-58. (in Russian)
- [6] *N.A. Torxov, V.Q. Bojkov, I.V. Ivonin, V.A. Novikov*. Fizika I tehnika poluprivodnikov. 2009 .T.43.Vip.1.S. 38-46. (in Russian)
- [7] *N.N. Qerasimenko, S.A. Aprelov*. Rossiyskie nanotehnologii, t.2,N1-2, 2007,s.136-139. (in Russian)
- [8] *S.A. Aprelov, S.A. Qaydukov, N.N. Qerasimenko, N.A. Metodov*. Izvestiya vuzov: Elektronika №2.220. s.25-32. (in Russian)
- [9] *N.N. Qerasimenko, M.N. Pavlyuchenko, K.K. Djamanbalin*. Izvestiya vuzov: Elektronika № 6,2002. (in Russian)
- [10] *Gomez –Rodriguez J.M. ,Baro. A. M. Salvarezza R.C* Journal of Vacuum Science and Technology B .191.- Vol 9. -No2. -P.495-499.
- [11] *V.V. Shitov, P.V. Moskalev*. JTF 2005. t .75.vip.2.s.1-5. (in Russian)
- [12] *S. Chesters, H.C. Wang, G. Kasper*. // A fraktal based method for describing surface roughness and texture. In Proc .of Insitute of Environmetal Science.- 1990-P.316.

Received: 27.06.2012

RADIATIVE RECOMBINATION IN  $\text{MnGa}_2\text{Se}_4$  SINGLE CRYSTALS

T.G. KERIMOVA<sup>1</sup>, O.B. TAGIYEV<sup>1,2</sup>, S.G. ASADULLAYEVA<sup>1</sup>,  
I.B. BAHTIYARLI<sup>3</sup>, K.O. TAGIYEV<sup>3</sup>

<sup>1</sup>*Institute of Physics of Azerbaijan National Academy of Sciences  
AZ1143, H.Javid ave., 3, Baku, Azerbaijan.*

<sup>2</sup>*The branch of Moscow State University named after M.V.Lomonosov in Baku*

<sup>3</sup>*Institute of Chemistry of Azerbaijan National Academy of Sciences  
AZ 1143, H.Javid ave., 29  
E-mail: oktay58@mail.ru*

The photoluminescence spectra of single crystal  $\text{MnGa}_2\text{Se}_4$  have been investigated at different temperatures. The photoluminescence spectrum has the doubling structure the intensity of which decreases with temperature increase, however, the energy position of doublet doesn't change. The independence of radiation lines at 2.53 eV and 2.38 eV proves the fact that photoluminescence in  $\text{MnGa}_2\text{Se}_4$  is connected with intracenter radiative transitions in  $\text{Mn}^{2+}$  ions from  ${}^4\text{T}_2({}^4\text{G})^6$  state into  ${}^6\text{A}_1$  one which is splitted by crystal field.

**Keywords:** radiative recombination, photoluminescence spectrum.

**PACS:** 76.30, 78.55

## INTRODUCTION

There are class of semimagnetic semiconductors by  $\text{A}^2\text{B}^3\text{C}^6$  (A-Mn, Fe, Ni, Co, B-Ga, In, C- S, Se, Te) type and solid solutions on their base among triple diamond-like compounds. These compounds crystallize in  $\text{S}_4^2$  space group and are crystal-chemical analogues of the compounds crystallizing in structures of chalcopyrite sphalerite.

Firstly  $\text{S}_4^2$  had been synthesized by authors [1]. In the result of the carried investigations it is established that this compound crystallizes in tetragonal structure (space group  $\text{S}_4^2$ ). The lattice parameters are:  $a=5,674 \text{ \AA}$ ,  $c=10,757 \text{ \AA}$ ,  $c/a=1.896$ . Further this compound had been synthesized by authors [2].

The presence of linear dichroism [4], the significant values of forbidden band which are in the combination with high photosensitivity and bright luminescence become the series of perspective materials for formation on their base of the optoelectronic transformers controlled by magnetic field, are character ones for these compounds. That's why the complete investigation of their physical properties is the actual task.

The magnetic properties of this compound are investigated in works [5,6] and it is revealed that  $\text{MnGa}_2\text{Se}_4$  at low temperatures has the antiferromagnetic properties and at 14GPa the phase transition into rock salt structure is observed and this transition is irreversible one.

Earlier the optical spectra in the region of intrinsic absorption edge and photoluminescence in  $\text{MnGa}_2\text{Se}_4$  [7] had been investigated by us. Because of absence of band spectrum calculations for identification of observable peculiarities and establishment of optic transition characters formulating the valence band top and conduction band bottom, we used the following moments. The method of theoretic-group analysis and crystal-chemical proximity of compounds crystallizing in the structure of sphalerite and chalcopyrite had been used so far as  $\text{MnGa}_2\text{Se}_4$  crystallizes in space group  $\text{S}_4^2$ . It is shown that minimal optical transitions are localized in the center of Brillouin zone and peculiarities at 2,31 and

2,45eV observed in long-wave region of optic absorption spectrum are connected with intracenter optic transitions in  $\text{Mn}^{2+}$  ions. The energy distance between maximums 2,31 and 2,45 eV is caused by crystal splitting of  ${}^6\text{A}_1$  state in  $\text{Mn}^{2+}$  ions.

In the present work the investigation results of photoluminescence spectra of single crystal samples  $\text{MnGa}_2\text{Se}_4$  in 77-185K interval are given.

THE PREPARATION OF  $\text{MnGa}_2\text{Se}_4$  SINGLE CRYSTALS AND EXPERIMENT TECHNIQUE

The diffusion method of gas-transport process is applied for growing of  $\text{MnGa}_2\text{Se}_4$  single crystals. The polycrystalline  $\text{MnGa}_2\text{Se}_4$  synthesized from corresponding elements with purity Mn – 99.99 %, Ga – 99.99 % and Se – 99.99 % was used in the capacity of initial object. The substance is put in the one of the edges of glassy quartz ampoule. The iodine (2-5mg per  $1\text{cm}^3$  of ampoule volume) in the capacity of transporting agent was put into ampoule (by length 160-200mm, diameter by 10-20mm) at 700–800 °C after degassing in the vacuum ( $10^{-4}$  –  $10^{-5}$  millimeter of mercury). Later the ampoule was evacuated up to  $10^{-5}$  millimeter of mercury and unsoldered. At iodine ampoule evacuating one its edge was cooled by mixture of dry ice with ethyl alcohol. The ready ampoule was situated in the middle part of horizontal two-sectional furnace so that all initial material was in one its edge. In all tests the crystallization band temperature in the furnace was controlled with the help of platinum-platinum-rhodium thermocouple the registrations of which were recorded by electronic automatic potentiometer EPR-09 M3. The transfer takes place from high temperature band  $\text{T}_2$  into low temperature band  $\text{T}_2$ . The transfer is carried out mainly by diffusion method. After process finishing the furnace was switched off and ampoule was cooled towards with furnace.

At carrier optimal quantity the single crystals  $\text{MnGa}_2\text{Se}_4$  of tetragonal structure with lattice parameters  $a=5.74 \text{ \AA}$ ,  $c=10.6 \text{ \AA}$  and space group  $\text{S}_4^2$  had been grown.

The photoluminescence spectra were measured on

device MDR-23. The radiation line of 365nm mercury arc lamp is used in the capacity of excitation source.

**EXPERIMENTAL RESULTS AND DISCUSSION**

The photoluminescence spectrum  $\text{MnGa}_2\text{Se}_4$  is shown on fig.1.

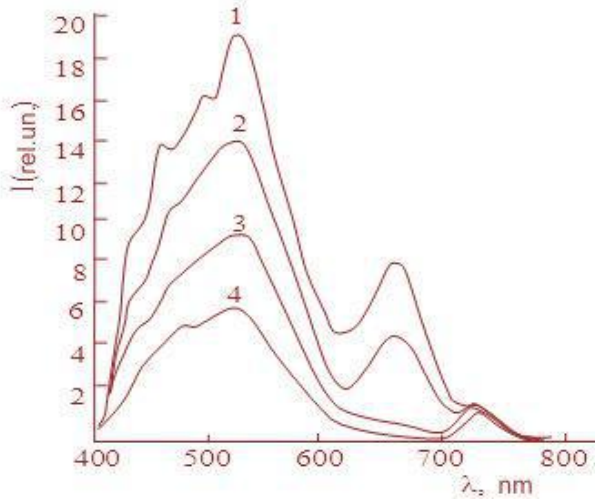


Fig.1. PL spectrum of  $\text{MnGa}_2\text{Se}_4$  single crystals at T, K: 1– 77, 2– 125, 3– 145, 4– 185.

It is seen that photoluminescence spectrum envelopes the region of wave lengths 400-600nm, from short-wave side it has the sloping decay and from long-wave side the strong one. The asymmetrical form and big semi-half of photoluminescence spectrum evidence about the fact that this photoluminescence band in interval 400-600nm isn't elementary one. Indeed, the bending is observed in spectrum from short-wave side at 490nm (2.43eV) and maximum is observed at 520nm (2.38eV).

The photoluminescence intensity decreases with temperature increase, however, the energy position of lines in doublet don't change. The energy distance between lines in doublet is equal to 0,14eV and coincides with energy distance in doublet in optic absorption spectra [5]. The independence of line energy position at 2.48eV and 2.53eV evidences about the fact that the observable doublet structure is connected with intracenter transitions in  $\text{Mn}^{2+}$  ions. Besides, the energy distance between lines in doublet structure is close to line values at 2.31eV and 2.45eV in optic absorption spectra [8]. Thus, we can conclude that radiative recombination in  $\text{MnGa}_2\text{Se}_4$  takes place from  ${}^4T_2({}^4G)$  state into  ${}^6A_1$  one splitted by crystal field ( ${}^4T_2({}^4G) \rightarrow {}^6A_1^1$  and  ${}^4T_2({}^4G) \rightarrow {}^6A_1^2$ ). The scheme of radiative transitions in  $\text{MnGa}_2\text{Se}_4$  is presented on fig.2.

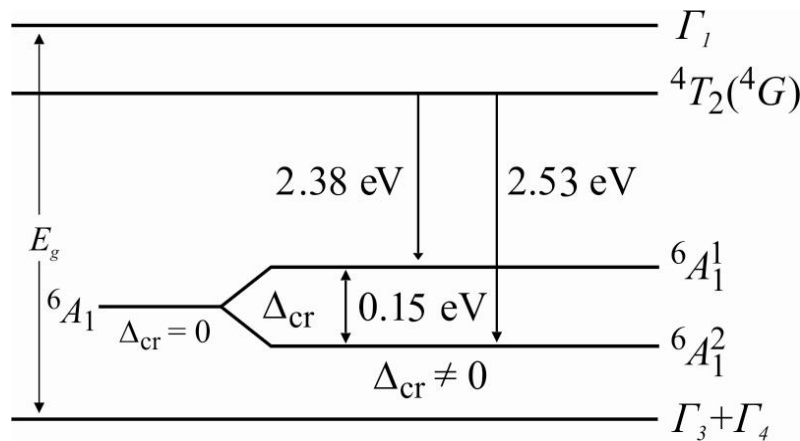


Fig. 2 The scheme of radiative transitions in  $\text{Mn}^{2+}$  ions in  $\text{MnGa}_2\text{Se}_4$ .

It is known that crystal splitting in triple tetragonal compounds is caused by complexity of chemical composition (two types of atoms in cation sublattice). Besides, the presence of lattice pressing along tetragonal axis is the character one for these compounds. These factors influence the excitative action on energy spectrum leading to term splitting. From above mentioned it is seen that term  ${}^6A_1$  of  $\text{Mn}^{2+}$  ion is splitted. The splitting value in doublet structure is equal to 0,15eV coincides with the same one in optic absorption spectra [8].

In photoluminescence spectrum of  $\text{MnGa}_2\text{Se}_4$  (fig.1) at 77K the radiative bands are observed at 690nm (1,8eV) and 730nm (1,9eV). The band intensity at 690nm decreases with temperature increase and at 180K doesn't

observe. The photoluminescence rapid damping evidences about the fact that in  $\text{MnGa}_2\text{Se}_4$  samples there are both centers of radiative recombination and ones at which the thermal ejection of non-equilibrium carriers from localized centers with following recombination on damping centers takes place.

**CONCLUSION**

The independence of radiation lines at 2.48eV and 2.53eV evidences about the fact that photoluminescence in  $\text{MnGa}_2\text{Se}_4$  is connected with radiative intracenter transitions in  $\text{Mn}^{2+}$  ions from state  ${}^4T_2({}^4G)$  into  ${}^6A_1$  one splitted by crystal field.

The given work is supported by Science Development Foundation under President of Azerbaijan Republic – Grant № EIF-2011-1(3)-82/01/1

- [1] *E.I. Range, H.J. Hubner.* Naturforschung, 316 (1976), 886.
- [2] *R. Rinet, D. Schlener, D. Fuchart.* J.Physique 47, (1982), 1759.
- [3] *R. Tovar, M. Quintero, F. Quintero, P. Bocaronda, J. Rutz, R. Caderas, Mora.* Materials Research Bulletin 37, (2002), 1011-1022.
- [4] *R.N. Bekimbetov, Q.A. Medvedking, V.D. Prochuxan, Yu.B. Rud, M.A. Tairov.* JTF 1987, t.23, v.17, s.1040-1043. (in Russian)
- [5] *M. Morocoima, M. Quintero, E. Quintero et al.* J. Appl. Phys., 2006, v. 100, No 5, p. 053907–053911.
- [6] *I. Consalez, R.I. Licos Caldera, M. Quintero, M. Maracoima.* Phys.Stat.Sol, 1999, v.211, №1, 45-49.
- [7] *Q.M. Niftiev, O.B. Tagiev, E.Z. Zeynalov, D. Aliev.* FTP, 1991, t.25., v.4., 704-705. (in Russian)
- [8] *B.Q. Tagiev, T.Q. Kerimova, O.B. Tagiev, I.A. Mamedova, S.Q. Asadullaeva.* Fizika, 2011, t.17, №3, s.16-17.

Received: 08.05.2012

## SUPERION CONDUCTION OF TlInSe<sub>2</sub> CRYSTALS RADIATED BY $\gamma$ – QUANTUMS

R.M. SARDARLI, O.A. SAMEDOV, N.A. ALIYEVA, A.P. ABDULLAYEV,  
F.T. SALMANOV, S.F. SAMEDOV, A.M. ALESKEROV

*Institute of radiation problems of Azerbaijan NAS  
370143, B.Vahabzade ave., 9, Baku, Azerbaijan  
sardarli@yahoo.com*

The investigations of TlInSe<sub>2</sub> crystal electric conduction on applied electric field strength (E) and  $\gamma$  - radiation show that the maximum value of conductivity along tetragonal axis at dose 50 mrad increases the initial one in 10 times, moreover, the transition temperature into superion state decreases. The critical values of radiation doze and electric field strength at which the abrupt conduction change, is observed, are obtained.

**Keywords:** superion conduction, activation energy, hopping conduction, volt-ampere characteristics (VAC), Frenkel-Pool thermo-field effect.

**PACS:** 72.20.-Fr

### INTRODUCTION

The compound TlInSe<sub>2</sub> crystallizes in tetragonal space group D<sub>4h</sub><sup>18</sup> and has 4 formula units in elementary cell [1]. In work [2] the authors inform about superion conduction in this crystal higher than temperature 300K which is connected with diffusion Tl<sup>+</sup> ion on vacancies in thallium sublattice between nano-rods (In<sup>3+</sup>Se<sub>2</sub><sup>-2</sup>).

The compound TlInSe<sub>2</sub> structure one can represent as the structure consisting of two systems: hard subsystem in the form of negatively charged rods (In<sup>3+</sup>Se<sub>2</sub><sup>-2</sup>) which are parallel ones to crystal axis and more mobile system of thallium ions [1]. The superion conduction in TlGaTe<sub>2</sub> crystals (structural analogue of TlGaTe<sub>2</sub>) at temperature higher than 300K is observed in works [3-5]. It is shown that Tl<sup>+</sup> ions are responsible for superion conduction also as in the case with TlInSe<sub>2</sub> crystal.

The investigation of temperature dependence of electric conduction  $\sigma(T)$  and volt-ampere characteristics (VAC) of single crystals TlGaTe<sub>2</sub> [5] subjected to different dozes of  $\gamma$  – radiation show that  $\sigma(T)$  dependence measured in VAC ohmic region has the hopping character and is described in Mott approximation. The density values of localized states  $N_F$ , activation energy  $E_a$ , jump lengths  $R$ , the difference between state energies  $\Delta E$  near Fermi level and concentrations of deep traps  $N_t$  are calculated. VAC investigations of TlGaTe<sub>2</sub> crystals in the region of more strong current increase show that this VAC region is described within the framework of Frenkel-Pool thermo-field effect. As the crystal lattice defects are the main reason of appearance of superion conduction, so in the given work we set the problem connected with radiation defect influence on peculiarity of superion conduction in TlInSe<sub>2</sub> crystal.

### EXPERIMENT TECHNIQUE

The TlInSe<sub>2</sub> compound samples are synthesized by the melting of initial components (purity not less 99,99) in vacuumed quartz ampoules and their single crystals are grown up by Bridgman modification method. The freshly cleaved samples prepared for investigation in which “c” crystal axis is oriented in a cleavage plane, have the rectangular form. The condensers in which the plates of investigated materials serve the dielectric are prepared for

measurement of temperature dependences of electric conduction of TlInSe<sub>2</sub> crystals. The condenser armatures are obtained by the marking of silver current-conducting paste on plate surfaces. The samples have the p-type conduction. The investigations of electric conduction are carried out by immittance numerical measurer E7-20 in temperature interval 100÷450K. The amplitude of measuring field doesn't exceed 1V·cm<sup>-1</sup>. After previous measurements  $\sigma(T)$  and  $\sigma(E)$  samples are subjected to the influence of  $\gamma$ -radiation from standard source of Co<sup>60</sup> radiation. The radiation doze accumulates gradually in each in investigated samples by the means of consistent expositions of  $\gamma$ - influence up to value 100mrad. Moreover, the measurements are carried out after each radiation exposition in temperature region 100-450K.

### EXPERIMENTAL RESULTS AND THEIR DISCUSSION

The temperature dependencies of electric conduction in two experiment geometries of  $\sigma_{||}(T)$  and  $\sigma_{\perp}(T)$  initial samples and TlInSe<sub>2</sub> crystals radiated by  $\gamma$  - quanta are given on fig.1a and fig.1b correspondingly.

It is known that crystal  $\gamma$ -radiation leads to formation of radiation defects in the form of vacancies, interstitial atoms and also the defects of different type complexes interacting between each other and with chemical impurities. Such type defects influence on the crystal conduction character and especially on the conduction:

- on localized states;
- on states caused by ionized impurities;
- and especially, directed radiation defects will influence on crystal ion conduction as ion conduction is directly result of structure defect.

As it is seen from fig.1a the conduction increase in temperature region with superion conduction is observed at measurements perpendicular to tetragonal axis “c” with radiation doze increase up to 50mrad. The defects of ionization type (charged defects) which appear as a result of radiation by  $\gamma$ -quanta, play the dominating role in these processes, i.e the radiation-stimulated healing of structure defects leading to the increase of crystal electric conduction is observed. The further increase of radiation doze leads to conduction decrease that obviously is connected with

increase of crystal structure imperfection under influence of  $\gamma$  - quanta. The doze in 50mrad is the critic one after

which  $\text{TlInSe}_2$  crystal conduction begins to decrease.

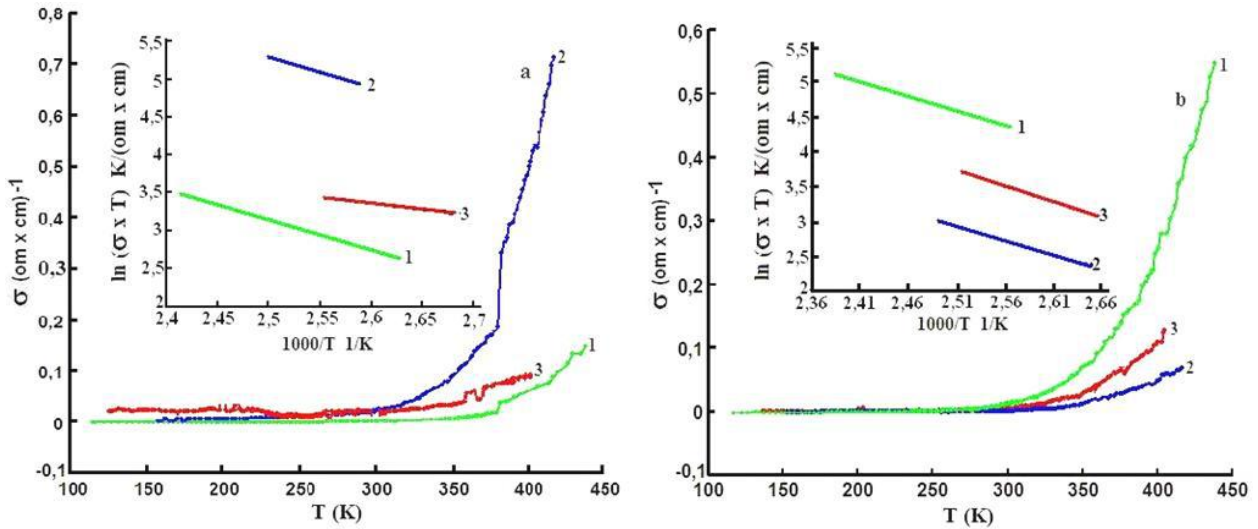


Fig.1. The temperature dependences of  $\sigma(T)$  electric conduction of  $\text{TlInSe}_2$  crystal. The figure (a) presents the measurements carried out perpendicularly to crystal tetragonal axis “c”, (b) presents the measurements carried out parallel to crystal tetragonal axis “c” (curves 1-3:0, 50, 100 mrad correspondingly, the dependence  $\ln(\sigma \cdot T)$  on  $1000/T$  is given on insertion).

At electric conduction measurement in the direction parallel to  $\text{TlInSe}_2$  crystal tetragonal axis “c” the conduction decrease is observed with increase of radiation doze and after doze 50mrad the conduction increase takes place (fig.1(b)). Thus, the conduction behavior different character on radiation influence at measurements in experiment different geometries is observed. The critic doze of  $\gamma$  - radiation (50mrad) after which the conduction strong increase ( $\approx 10$  times) for measurements in geometry perpendicular to chains ( $\sigma_{\perp}(T)$ ) and strong conduction decay ( $\approx 10$  times) at measurements parallel to chains ( $\sigma_{\parallel}(T)$ ) are observed, is the general one for measurements in geometries  $\sigma_{\perp}(T)$  and  $\sigma_{\parallel}(T)$ .

The dependence  $\ln(\sigma \cdot T)/1000T$  for temperature region with superior conduction [2] is given on insertion of figures 1a and 1b, as it is seen, the experimental points of this dependence are well situated on direct line which is described for the case of ion conduction by the equation [6-8]:

$$\sigma T = \sigma_0 \exp(-\Delta E^{\sigma}/kT) \quad (1)$$

It is known that such character of electric conduction shows on the dominating character of ion conduction higher than critic temperature [7,8]. The electric conduction increase  $\sigma(T)$  with temperature increase is caused mainly by  $\text{Tl}^+$  ion diffusion on vacancies of  $\text{TlInSe}_2$  crystals in thallium sublattice. This change takes place in the result of phase transition accompanying by disorder (melting) of Tl crystal sublattice. Such lattice is typical for superior semiconductors [6-8].

The calculative values of activation energies  $\Delta E^{\sigma}$  of unirradiated and irradiated  $\text{TlInSe}_2$  crystals are given in the table.

As it is known the ion disorder not only depends on crystal temperature but also in general case can change under influence of external fields and  $\gamma$ - radiation.

Activation energy  $\Delta E^{\sigma}$  of unirradiated and irradiated  $\text{TlInSe}_2$  crystals

	direction	initial	50 mrad	100 mrad
$\Delta E^{\sigma}$	$\sigma_{\parallel}c$	0,52 eV	0,96 eV	0,76 eV
	$\sigma_{\perp}c$	0,84 eV	0,5 eV	0,79 eV

The measurement results of  $\text{TlInSe}_2$  crystal electric conduction on electric field strength  $E$  and  $\gamma$  -radiation at different temperatures are presented on fig.2 (figure a: the measurements are carried out parallel to crystal tetragonal axis “c”, b: the measurements are carried out perpendicular to crystal tetragonal axis “c”). At comparably few fields the conduction doesn’t practically depend on field that is connected with the fact that conduction in this field strength region is defined by electronic component. At defined critic field value

The switching effect is observed, i.e. by our opinion the disorder of cation sublattice Tl in electric field takes place. In this region the conduction ion component dominates under electronic conduction. In  $\gamma$ -radiated  $\text{TlInSe}_2$  crystals the ion conduction dominates under electronic one at low values of electric field strength  $E$ . This is connected with increase of cation sublattice disorder  $\text{Tl}^+$  under influence of  $\gamma$ -radiation.

The temperature dependence of strength at which the switching in  $\text{TlInSe}_2$  crystal from high-ohmic state into low-ohmic one takes place, is given on fig.3. The initial samples are given on figure 1, the samples subjected to 100 mrad doze of  $\gamma$  - radiation are given on figure 2. As it is seen from the figure on the samples subjected to radiation influence the switching into low-ohmic state takes place at more high values of electric field strengths. The monotonous decay of switching strength value is observed with temperature increase.

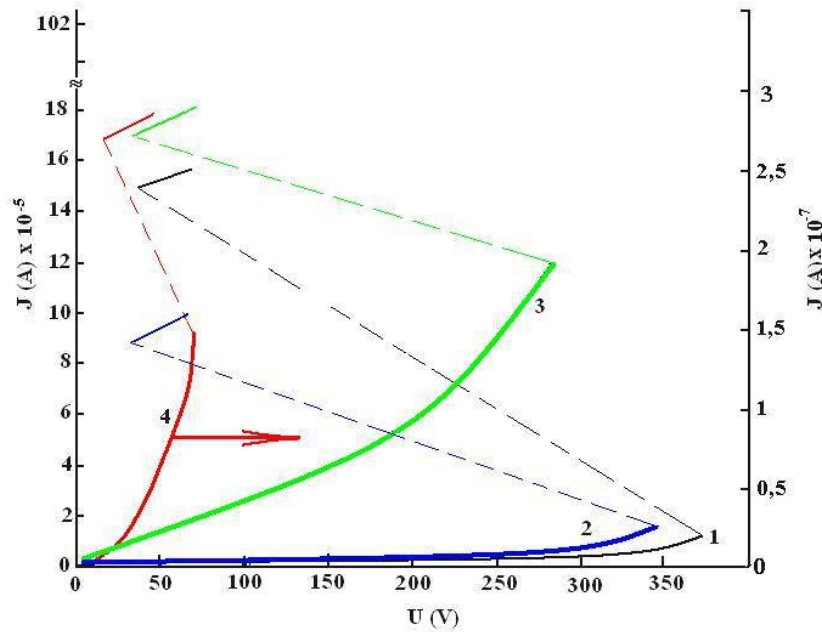


Fig.2. The TlInSe<sub>2</sub> crystal volt-ampere characteristics in geometry parallel to crystal tetragonal axis. The samples are subjected to  $\gamma$  - radiation of doze in 100 mrad at temperatures 1-168K, 2-260K, 3-300K and 4-300K (at radiated 100 mrad).

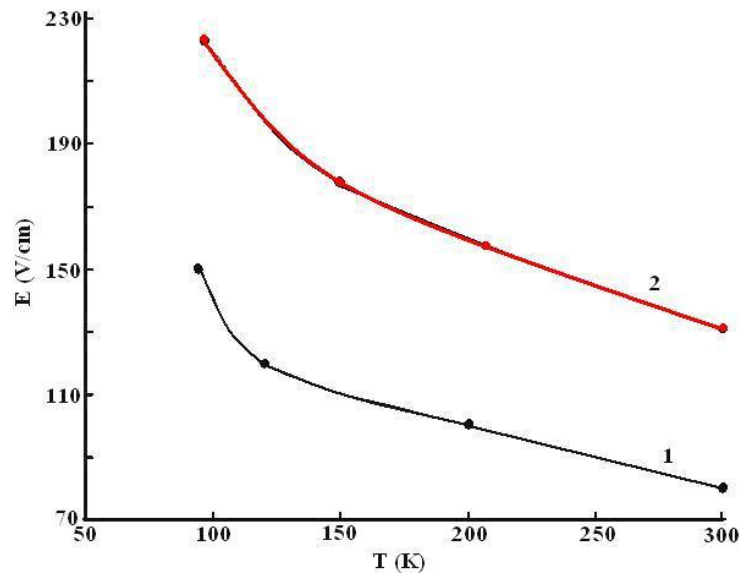


Fig. 3. Temperature dependence of strength at which the switching in TlInSe<sub>2</sub> crystal from high-ohmic state into low-ohmic one takes place. 1 are initial samples, 2 are samples kept by 100 millirad doze of  $\gamma$  - radiation.

## CONCLUSION

Thus, the obtained results show that at temperatures lower 360K the electron component of conduction dominates. The conduction abrupt increase is observed with further temperature increase that is connected with increase of ion component caused by disorder cation sublattice Tl<sup>+</sup>. In the given temperature region the ion component of conduction already dominates under electron one. It is shown that at measurements perpendicular to TlInSe<sub>2</sub> crystal tetragonal axis “c”, the maximum value of electric conduction at doze 50 mrad in 10 times exceeds the initial values of TlInSe<sub>2</sub> crystal electric conduction and transition temperature into superion state shifts to the side of low temperatures. The investigations of TlInSe<sub>2</sub> crystal electric conduction

dependence on strength of applied electric field and radiation doze by  $\gamma$ - quantum shows on appearance possibility of abrupt disorder of ion sublattice Tl<sup>+</sup> which is accompanied by abrupt conduction change at defined critic value of electric field strength and radiation doze.

Note that the described effect induced by the field of abrupt disorder gives the possibility to realize the TlInSe<sub>2</sub> crystal superion state at enough comfortable temperatures (from applied point of view) that opens the interest possibilities of its practical use.

The given work is carried out at financial support of Science Development Foundation under President of Azerbaijan Republic – Grant № EIF-2011-1(3)-82/13/1.

- 
- [1] V.D. Muller, H. Hahn. Zur structur des  $TiGaSe_2$ , Z. Anorg. Allg. Chem. v.438, №1, 1978, 258-272.
- [2] R.M. Sardarli, O.A. Samedov, A.P. Abdullayev, F.T. Salmanov, O.Z. Alekperov, E.K. Guseynov, N.A. Aliyeva. Phizika i tekhnika poluprovodnikov. 2011, t. 45, vip. 11, 1441-1445.(in Russian)
- [3] R.M. Sardarli, O.A. Samedov, A.P. Abdullayev, E.K. Guseynov, E.M. Gojayev, F.T. Salmanov. Phizika i tekhnika poluprovodnikov. 2011, t. 45, vip. 8, 1009-1013.(in Russian)
- [4] R.M. Sardarly, O.A. Samedov, A.P. Abdullaev, F.T. Salmanov, A. Urbanovic, F. Garet, J-L. Superionic Conductivity in One-Dimensional Nanofibrous  $TiGaTe_2$  Crystals. Japanese Journal of Applied Physics 50 (2011) 05FC09-1 – 2.
- [5] R.M. Sardarli, O.A. Samedov, A.P. Abdullayev, E.K. Guseynov, F.T. Salmanov, G.R. Safarova. Phizika i tekhnika poluprovodnikov. 2010, t. 44, vip. 5, 610-614. (in Russian)
- [6] A.Lidyard. Ionnaya provodimost kristallov. Izd-vo IL, M.,1962. 222 s. (in Russian)
- [7] L.S. Parfyonovaba, A.I. Shelikh, A.I. Smirnov, A.B. Prokofyev, V. Assmus. FTT , 2004, t. 46, vip. 6, 998-1000.(in Russian)
- [8] L.S. Parfyonovaba, A.I. Shelikh, A.I. Smirnov, A.B. Prokofyev, V. Assmus., Kh. Misiorek, Y. Mukha, A. Yejovskiy, I.G. Vasilyeva. FTT, 2003, t. 45, vip. 11, 1991-1996. (in Russian)

Received: 20.06.2012

## THE INCIDENCE ANGLE INFLUENCE ON THE STRUCTURE OF SECONDARY-EMISSION CHARACTERISTICS OF SINGLE CRYSTALS

**E.R. GASANOV**

*Baku State University, AZ-1148, Z. Khalilov str., 23*

**B.Z. ALIYEV**

*Azerbaijan Technical University, AZ-1073, H. Javid ave., 25*

The dependences  $\sigma(\varphi), \eta(E_p)$  and  $\sigma(E_p)$ , of  $W$  and  $M_0$  single crystals in different atom planes have been studied in this work. It is revealed that maximums are added to each dependency and also minimums of first and second degree. This fact is explained by diffraction dynamic theory.

**Keywords:** maximum, minimum, diffraction, dynamic theory, single crystal.

**PACS:** 07.57-c, 77.22.Ch

It is established that electron diffraction oriented not perpendicularly to crystal surface is the reason of appearance of second order structure on studied secondary-emission characteristics. By comparison of  $E_p$  value found by the way of graphic construction of Evald sphere and reciprocal lattice with experimentally defined nonmonotonicity of energy positions, allows us to come to agreement them with each other. The development of first order structure at small angles  $\varphi \leq 1^\circ$  shows that it is very sensitive. It is obvious that it directly connects with effects of very accurate orientations of incident beam relative to lattice.

The electron interaction with solid state lattice periodic field accompanying by their diffraction dispersion leads to redistribution of electric density of electron beam incident on solid state surface at its penetration and propagating into crystal depth [1,2]. The flow electrons can be concentrated both near lattice nodes and in the space between them in the dependence on incident beam orientation relative to crystallographic lattice axes. The differences in space localization of electron charge density form the anisotropy of their motion conditions in single crystals. This exists in orientation effects of almost all phenomena accompanying to solid state electron penetration and particularly, secondary electron emission (SEE).

SEE anisotropy [3-10] reveals firstly in the difference of secondary-emission parameters of single different crystal edges, secondary, in the fact that clear structure which is also different of different crystal faces, is character for secondary-emission single crystal characteristics. The structure belongs to dependences of electron reflection coefficients (ERC)  $\eta$ , SEE (CSEE)  $\sigma$  and real SEE (CRSEE)  $\delta$  on primary electron energy  $E_p$ . The investigation of this structure of single crystals of high-melting metals [6,8] allows us to divide it on two types differing between each other by nonmonotonicity amplitudes and their energy lengths and designated in [8] as structures of first and secondary orders. In work [4] it is noted that structure of considered of SEE main dependences is sensitive to small changes of angle  $\varphi$  of incident electrons on the crystal. There is no information

about the fact, whether small variations of  $\varphi$  angle influence on both revealed structure types or on only one of them in work [4]. Moreover, such information can be useful at decoding of this structure.

In the present work being the continuation and development of SEE investigations of high-melting metal single crystals begun earlier by authors, the structure dependence of SEE main characteristics of face (III)  $w$  on  $\varphi$  angle has been studied. The face (III)  $w$  has been chosen because as it is mentioned in [9] the bad repeatability in different experiments for it is observed. Either small difference in  $\varphi$  angles connected with not enough alignment accuracy of electron injector, or any uncontrolled defects and imperfections of crystal surface layers are the reason of all this.

### 1. EXPERIMENT TECHNIQUE AND RESULTS

The measurements are carried out in sealed device at pressure  $\leq 10^{-8}$  millimeter of mercury. The device is constructed so that one can possible to take measures of two different samples. With this aim the crystals are fixed on molybdenic rod which is build up perpendicular to electron injector axis. Rod of magnet can be rotated round its axis changing angle  $\varphi$  and shifted to horizontal direction put the necessary sample under electron beam and also established the crystals in positions in which their degassing is carried out. The angle  $\varphi$  is defined by the inclination of light spot which reflected from the mirror fixed on crystal holder. The measurement error of  $\varphi$  increases with  $\varphi$  increase. At  $\varphi$  equal to several degrees, it is approximately equal to  $30^\circ$ .

The inaccuracy of (III) face obtaining of both investigated single crystals doesn't exceed 10. They are established so that for one crystal (sample 1) electron beam is approximately in plane (112) and for second one (sample 2) it is in plane (110) at change  $\varphi$ .

The measurements are carried out in static mode in interval  $E_p = (0,3 \div 2)$  keV. For sample 1 almost all data are obtained with the help of electrometric scheme with Veston normal elements. The errors of  $\eta$  and  $\sigma$  definition are (0,2-07)%, of coefficient  $\delta = \sigma - \eta$  it is

not less (0, 6-1, 2)%. The measurement inaccuracy of  $E_p$  is near 1eV. The measurements with sample 2 are carried out with the help of galvanometers M1201 and have the less accuracy and especially:  $\frac{\Delta\eta}{\eta}$  and  $\frac{\Delta\sigma}{\sigma}$  in the limits

(1-1,5)%, but  $\frac{\Delta\delta}{\delta}$  - (2-3)%. Errors of  $E_p$  measurements achieves 20-30eV at  $E_p \simeq (1,5-2)$ keV. Thus, for sample 2 one can be obtained results only about structure of first order.

The clear structure beginning from less  $E_p$  values used in the present work is observed in both crystals on CSEE angle dependences, i.e. with  $E_p \simeq (250-300)$  eV (fig.1). According [10] this is indirect confirmation of enough perfectness of surface layers of the investigated samples.

For the revealing  $\varphi$  angle influence on the structure of main secondary-emission characteristics, the dependences  $\eta(E_p)$  and  $\sigma(E_p)$  are measured at different  $\varphi$  every interval  $\Delta\varphi \simeq 45^\circ \div 1^\circ 30'$ . The angle corresponding to central maximum position on  $\eta(\varphi)$  and  $\sigma(\varphi)$  curves is taken as  $\varphi = 0$ .

The obtained results are illustrated on fig.2 and 3 on which  $\eta(E_p)$  and  $\sigma(E_p)$  curves are given for both crystals for four  $\varphi$  values. The curves relating to sample 2 are shifted below on 0,1.

The consideration of given data on fig.2 and 3 shows that small changes of electron incident angle significantly influence on general behavior of investigated dependences which is defined by structure of first order. Especially clearly this is revealed in CRE for which the first order structure is more strongly expressed.

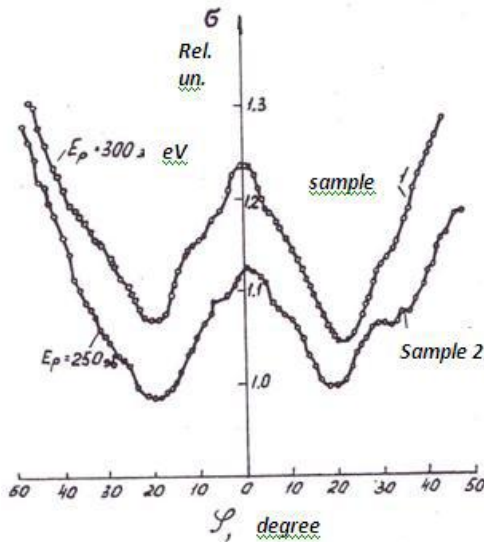


Fig.1. CSEE dependences on electron incident angle  $\varphi$  on the crystal.

Let's consider the question about influence of  $\varphi$  small changes on second order structure. With this aim the second-emission characteristics of sample 1 are measured every intervals  $\Delta E_p \simeq 10$ eV.

It is seen that all curves have the energy position of dominating number of nonmonotonicity approximately coincides. The influence of  $\varphi$  small changes reveals mainly in amplitude variations of structure peculiarities of second order and changes of their form.

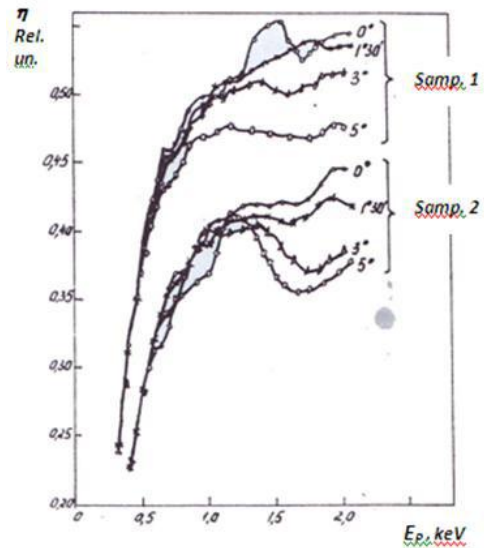


Fig. 2. CRE dependences on  $E_p$  energy of primary electrons at different angles  $\varphi$ .

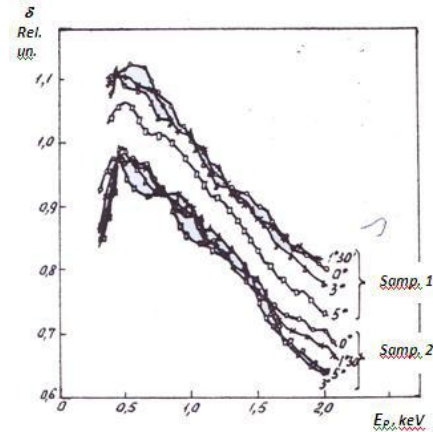


Fig.3. CRSEE dependences on  $E_p$  energy of primary electrons at different angles  $\varphi$ .

Thus, in the difference on first order structure which is sensitive even to small  $\varphi$  changes less than  $1^\circ$ , the second order structure on  $\varphi$  (at small  $\varphi$ ) weakly depends.

As differences in first order structure caused by small  $\varphi$  variations reveal mainly at  $E_p$  exceeding  $\sim 1$ keV and  $\sigma_{max}$  and  $\delta_{max}$  are at less  $E_p$ , these changes of  $\varphi$  angle insignificantly influence on values themselves  $\sigma_{max}$  and  $\delta_{max}$  and  $E_{p,max}$  and  $E_{p,max}$  values corresponding to them. The biggest  $\eta$  values obtained by us for faces and  $E_p$  region (in investigated interval  $E_p$ ) in which they are observed, are given in the table. It is consisted on the base of all experimental data obtained by us for investigated faces w and  $M_0$  and also polycrystalline samples of the same metals.

Table 1

Surfaces	(100)	(111)	(110)	Polycrystal
		w		
$\delta_{max}$	1,84-1,66	1,52-1,58	1,44-1,48	1,42
$E_{p,max}^{eV}$	760-790	650-680	~550 and ~720	700
$\delta_{max}$	1,15-1,18	1,08-1,12	~1,06	1,10
$E_{p,max}^{eV}$	470-490	550-570	500-550	400
$\eta$	~0,6	~0,55	~0,6	
$E_p^{eV}$	1400-1500	1450-1550	2200-2600	
		Mo		
$\delta_{max}$	1,50-1,52	~1,45	1,33-1,35	1,27
$E_{p,max}^{eV}$	350-400	~350 and ~540	440-460	400
$\delta_{max}$	1,09-1,11	1,13-1,14	0,87-1,02	0,99
$E_{p,max}^{eV}$	~350	~360	~360	370+380
$\eta$	~0,45	~0,42	~0,43	
$E_p^{eV}$	1300-1600	2200-2800	2500-3000	

**2. RESULT DISCUSSION**

The general comparison of secondary-emission parameters of studied faces is made by us in [9]. Note that only the fact that all three faces (100), (110) и (111) w and Mo both CRE and CSEE are higher than polycrystal samples of the same metals have. In [9] some thoughts concerning to electron diffraction scattering in crystals are said. Let’s consider this task more detail.

Analyzing the diffraction phenomena appearing at the radiation of main boundaries (100), (110) band (110)w and Mo by electrons of average energies, they are divided in two types. Firstly, electron waves normally incident on the edge (hkl) and diffract on planes perpendicular to crystal surface. Secondary, electrons can be in the diffraction scattering on any other planes oriented not perpendicular to surface crystal. The main difference between the given two types of diffraction phenomena is in the fact that in the first case the diffraction takes place at all  $E_p$  and Bregg condition here is always carried out inaccurately. In the second case for each system of the reflecting planes the Bregg condition can be strongly satisfied, and this takes place at fixed values of these (hke) and  $E_p$ .

The theoretic consideration of first type of electron diffraction scattering, for example, in [1,2] is carried out only within the framework of two-wave approximation, i.e. at supposition about appearance of only one diffracted wave in the crystal. The appearance of this wave in the crystal and its interaction with incident nonscattered wave leads to redistribution of charge density in the electron flow penetrating into solid state depth, that is described by two Bloch waves having the different space symmetry. At electron motion parallel to reflecting planes (hkl) the case  $\varphi < \varphi_{Br}$  (where  $\varphi_{Br}$  is Bregg angle) realizes and from two Bloch waves excited in the crystal, the second type wave with dominating localization of electron cloud in lattice nods has the biggest intensity .

Let’s consider the second from above mentioned types of electron diffraction scattering. The symmetry conditions having the definite boundaries on excitation

possibility of different Bloch waves [2] in the crystal play for it the significant role at normal electron incident on main faces of the crystals. Taking under consideration these conditions, as we mention in [8,9], also causes the dominant distribution in solid state of second type wave which are strongly scattered by the substance. This should lead to the additional increase of CRE.

As for each system of planes (hkl) Bregg condition is carried out only at fixed value  $E_p$  then changing electron energy from  $E_p < E_p$  up to  $E_p > E_p$  we constitutently pass through  $\Delta E_p$  regions where  $\varphi < \varphi_{Bp}$ ,  $\varphi = \varphi_{Bp}$  and  $\varphi > \varphi_{Bp}$ .

The electron diffraction on the planes oriented not perpendicular to crystal surface is the reason of the appearance of second order structure on investigated secondary-emission characteristics. The comparison of  $E_p$  values found by graphic construction of Evald sphere cross-section and reciprocal lattice with experimentally defined energy positions of the given nonmonotonocities indeed allows us to agree them with each other.

The small changes of electron incident angle  $\varphi$  on crystal surface of  $\sim (1:3)^0$  order in the investigated interval  $E_p$  leads to insignificant inclinations from Bregg conditions. That’s why their influence reveals mainly because of disturbance of symmetry condition of beam orientation that leads to electron density redistribution in wave field propagating in the crystal with  $\eta$  value change accompanying to it. The energy position of considered nonmonotonocities of second order structure in correspondence with exeriment data at  $\varphi$  angle small changes, is approximately saved.

The most difficulties appear at attempts to consider the first order structure. As it is seen above, it is very sensitive even to small  $\varphi (\leq 1^0)$  angle changes. That’s why it is directly connected with effects of very accurate orientations of incident beam relative to lattice. Nowadays we can’t say more detail about this.

- [1] *H. Hashimoto, A. Howie, M.J. Whelan.* Proc.Roy.Soc., A269, 80, 1962; *Howie A.* Philos.Mag., 14, 233, 1966
- [2] *P. Xirsh, A. Xovi, R. Nikolson, D. Peshli, M. Uealan.* Elektronnaya mikroskopiya tonkix kristallov. Izd-vo «Mir», M., 1968. (In Russian)
- [3] *B.D. Krachev, A.P. Komar, Yu.S. Korobochk., V.I. Mineev.* FTT, 10, 2408, 1968. (In Russian)
- [4] *A.P. Shulman, V.V. Korablev, Yu.A. Morozov.* FTT, 10, 1571, 1968. (In Russian)
- [5] *A.P. Shulman, V.V. Korablev.* Ri E, 11. 2432. 1970.(In Russian)
- [6] *A.P. Shulman, V.V. Korablev, Yu.A. Morozov.* FTT, 10, 1913, 1968, *Izv.AN SSSR, ser. Fiz.33,* 475, 1969. (In Russian)
- [7] *P.W. Palmeg.* J.Appl. Phys., 38, 2137, 1967.
- [8] *A.P. Shulman, V.V. Korablev, Yu.A. Morozov.* FTT, 12, 758, 1970. (In Russian)
- [9] *M.V. Qomoyunova, B.Z. Aliev.* FTT, 11, 3619, 1969. (In Russian)
- [10] *M.V. Qomoyunova, B.Z. Aliev.* FTT, 12, 2742, 1970. (In Russian)
- [11] *M.V. Qomoyunova, B.Z. Aliev.* *Izv. AN SSSR, ser.fiz.35,* 231, 1972.(In Russian)
- [12] *V.V. Korablev.* Avtoreferat kand. diss., LPI im. M.I. Kalina, 1972. (In Russian)

*Received: 06.06,2012*

**RELATIVISTIC QUANTUM FREE PARTICLE  
IN A VARIABLE HOMOGENEOUS FIELD**

**SHAKIR M. NAGIYEV, KONUL Sh. JAFAROVA**

*Institute of Physics, Azerbaijan National Academy of Sciences,*

*Javid Av. 33, AZ-1143 Baku, Azerbaijan*

*E-mail: [smnagiyev@physics.ab.az](mailto:smnagiyev@physics.ab.az)*

A one-dimensional motion of a relativistic quantum particle in a variable homogeneous field is considered. This exactly solvable problem is formulated in the framework of a relativistic finite-difference quantum mechanics. Wave function of the system in the relativistic configurational  $x$  - representation satisfies a finite-difference equation, but in the momentum  $p$  -representation it satisfies a partial differential one. In our case the momentum space is a one-dimensional Lobachevski space, realized on the upper branch of the mass hyperbola  $p_0^2 - p^2 = m^2 c^2$ . The connection between  $x$  - and  $p$  - representations is given by the use of an evolution operator of the system. The evolution operator is defined through the chronological  $T$  - product. We have also found a solution of a definite class of partial differential and finite-difference equations. Explicit form of the wave functions in  $p$  -, as well as in  $x$  - representations is obtained. It is showed that they *i)* satisfy the orthogonality and complicity conditions and *ii)* have a correct non-relativistic limit. We have derived the new operator identities analogous to the well-known Beyker-Hausdorff formula.

**Keywords:** relativistic quantum free particle, variable homogeneous field

**PACS:** 539.145.6, 539.12.01

**1. INTRODUCTION**

The finite-difference variant of relativistic quantum mechanics is developed in works [1-14]. This variant is based on the perception of relativistic configurational  $\vec{r}$  - space [1].  $\vec{p}$  -impulse space canonically conjugated to  $\vec{r}$  - space is Lobachevski three-dimensional space realized on head margin of mass hyperboloid  $p_0^2 - \vec{p}^2 = m^2 c^2$ . Lorenz group is the group of impulse space motion. The relativistic plane waves [1] connecting  $\vec{r}$  - and  $\vec{p}$  - spaces are introduced in work [15] and has the form:

$$\xi(\vec{p}, \vec{r}) = \left( \frac{p_0 - \vec{p}\vec{n}}{mc} \right)^{-1 - i\vec{r}/\lambda}, \quad (1)$$

where  $\lambda = \hbar/mc$  is Compton length of particle wave and  $\vec{n} = \vec{r}/r$ .

Within the framework of finite-difference relativistic quantum mechanics many exactly solvable quantum-mechanic tasks (potential well [1], Coulomb potential [2,8,9], harmonic oscillator [4,6,7],  $q$  -deformed oscillator [10,11], singular oscillator [13] and etc) are generalized for relativistic case.

Here we are limited ourself by consideration of one-dimensional motion. In one-dimensional case the functions [6] play the role of plane waves (1)

$$\xi(p, x) = \left( \frac{p_0 - p}{mc} \right)^{-ix/\lambda} \equiv e^{ix/\lambda}. \quad (2)$$

Here value  $\chi = \ln \frac{p_0 + p}{mc}$  is called by the rapidity,

$p_0 = mc \operatorname{ch}\chi$ ,  $p = mc \operatorname{sh}\chi$ . The one-dimensional impulse Lobachevsky  $p$  -space is realized on upper branch of mass hyperbole  $p_0^2 - \vec{p}^2 = m^2 c^2$ . In this space the function system (2) is orthogonal and complete one, i.e.

$$\begin{aligned} \frac{1}{2\pi\hbar} \int_{-\infty}^{\infty} \xi^*(p, x) \xi(p', x) dx &= \frac{1}{mc} \delta(\chi - \chi'), \quad (3) \\ \frac{1}{2\pi\hbar} \int_{-\infty}^{\infty} \xi^*(p, x) \xi(p, x') d\Omega_p &\equiv \\ \equiv \frac{1}{2\pi\lambda} \int_{-\infty}^{\infty} \xi^*(p, x) \xi(p, x') d\chi &= \delta(x - x') \end{aligned}$$

where  $d\Omega_p = mc dp/p_0 = mc d\chi$  -is volume invariant element.

The wave functions in impulse  $p$ - and relativistic configuration  $x$ -representations are connected between each other by Fourier relativistic transformation, i.e.

$$\begin{aligned} \phi(p, t) &= \frac{1}{\sqrt{2\pi\hbar}} \int \xi^*(p, x) \psi(x, t) dx, \\ \psi(x, t) &= \frac{1}{\sqrt{2\pi\hbar}} \int \xi(p, x) \phi(p, t) d\Omega_p. \quad (4) \end{aligned}$$

The wave function  $\psi(x, t)$  in one-dimension relativistic configuration  $x$ -representation satisfies to finite-difference equation

$$i\hbar \frac{\partial \psi(x, t)}{\partial t} = [H_0 + V(x, t)]\psi(x, t), \quad (5)$$

where  $H_0 = mc^2 \text{ch} \lambda \partial_x$  is free Hamiltonian, and  $V(x, t)$  is potential energy (quasi-potential). The equation (5) is obtained from non-stationary Schrodinger equation if we exchange in it the usual differentiation on  $x$  on finite-difference differentiation with step  $h = i\lambda$  [11].

In non-relativistic limit eq.(5) transits into non-stationary Schrodinger equation and relativistic plane waves (2) transit into usual plane waves:

$$\lim_{c \rightarrow \infty} \xi(p, x) = \exp(ipx/\hbar).$$

The study of one-dimensional motion of free relativistic quantum particle in variable homogeneous field is the aim of the present work. This exactly solvable task in  $x$ -representation is described by equation

$$i\hbar \frac{\partial \psi(x, t)}{\partial t} = [mc^2 \text{ch} \lambda \partial_x - F(t)x]\psi(x, t), \quad (6)$$

where  $F(t)$  is force dependent on time which influences on the particle. This task is formulated within the framework of finite-difference relativistic quantum mechanics. Some its aspects are considered in work [16]. The same task in the case when force influencing on the particle doesn't depend on time is studied in [14]. The solutions of corresponding non-relativistic stationary and non-stationary tasks [18] are known.

The article structure is given in the following form: in §2 the particle motion is described in impulse representation. §3 is dedicated to the same task in relativistic representation. In §4 we obtain the operator identity which are the analogues of known Beyker-Hausdorf formula §5 is conclusion. In application we obtain some formulae using in text.

## 2. PARTICLE MOTION IN IMPULSE $P$ -REPRESENTATION

To solve the equation (6) is convenient to the impulse representation. We have

$$i\hbar \frac{\partial \phi(p, t)}{\partial t} = [mc^2 \text{ch} \lambda - i\lambda F(t) \frac{\partial}{\partial \lambda}] \phi(p, t). \quad (7)$$

In the nonrelativistic limit, this equation transforms to the corresponding non-stationary Schrodinger equation:

$$\hat{U}(y, t) = \text{Te}^{-\frac{i}{\hbar} \int_0^t H(t') dt'} = \text{Te}^{-\frac{i}{\hbar} \int_0^t [H_0(y) - i\hbar a(t') \frac{\partial}{\partial y}] dt'}, \quad t > 0. \quad (12)$$

According to Dawson formula the meaning of the expression in right part of (12) is defined by exponent power series expansion:

$$i\hbar \frac{\partial \phi_N(p, t)}{\partial t} = \left[ \frac{p^2}{2m} - i\hbar F(t) \frac{\partial}{\partial p} \right] \phi_N(p, t). \quad (8)$$

Equations (7) and (8) are special cases of following type

$$i\hbar \frac{\partial u(y, t)}{\partial t} = \left[ H_0(y) - i\hbar a(t) \frac{\partial}{\partial y} \right] u(y, t), \quad (9)$$

where  $H_0(y)$  is free Hamiltonian in impulse representation and  $a(t)$  is force depending on time.

In work [16] the solution of equation (9) satisfying to initial condition  $u(y, 0) = \varphi(y)$  is found with the use of evolution operator  $\hat{U}(y, t)$  of the system in  $p$ -representation :

$$u(y, t) = \hat{U}(y, t)u(y, 0), \quad (10)$$

In terms of  $\hat{U}(y, t)$  the motion equation (9) has the form:

$$i\hbar \frac{\partial \hat{U}(y, t)}{\partial t} = H(t) \hat{U}(y, t). \quad (11)$$

Here  $u(y, 0) = \varphi(y)$  is wave function of corresponding stationary task in  $p$ -representation at  $t=0$  playing the initial condition role, and

$H(t) = H_0(y) - i\hbar a(t) \frac{\partial}{\partial y}$  is total Hamiltonian, moreover  $t > 0$ . As operators  $H(t)$  for different  $t$  values shouldn't commute with each other, then from (11) we have usable representation for  $\hat{U}(y, t)$  operator over chronological  $T$ -composition (see for example [19])

$$\begin{aligned}\hat{U}(t) &= 1 + \sum_{n=1}^{\infty} \frac{(-i/\hbar)^n}{n!} \int_0^t dt_1 \int_0^{t_1} dt_2 \dots \int_0^{t_{n-1}} dt_n T(H(t_1)H(t_2)\dots H(t_n)) = \\ &= 1 + \sum_{n=1}^{\infty} \frac{(-i/\hbar)^n}{n!} \int_0^t dt_1 \int_0^{t_1} dt_2 \dots \int_0^{t_{n-1}} dt_n H(t_1)H(t_2)\dots H(t_n),\end{aligned}\quad (13)$$

i.e. the symbol  $T$  shows on the fact that noncommutating operators  $H(t_i)$  ( $i = 1, 2, \dots, n$ ) should be ordered on time.

The solution of equation (9) found in [16] has the following form:

$$u(y, t) = e^{-\frac{i}{\hbar} \int_0^t H_0(y - \delta(t) + \delta(t')) dt'} \varphi(y - \delta(t)), \quad (14)$$

where  $\delta(t) = \int_0^t a(t') dt'$  designation is introduced.

Taking under consideration (14) we now obtain the following expression for wave function of considered relativistic quantum system in  $p$ - representation:

$$\phi_E(p, t) = e^{-\frac{i}{\hbar} \int_0^t mc^2 \text{ch}(\chi - \delta_R(t) + \delta_R(t')) dt'} \phi_E^{(0)}(\chi - \delta_R(t), 0). \quad (15)$$

Here  $\phi_E^{(0)}(\chi, t)$  is wave function in the case of constant force when  $F(t) = F_0 = \text{const}$  [14]

$$\phi_E^{(0)}(\chi, t) = \frac{1}{\sqrt{2\pi\hbar|F_0|}} e^{\frac{i}{\lambda F_0}(\chi E - mc^2 \text{sh}\chi) - \frac{iEt}{\hbar}}, \quad (16)$$

and  $\delta_R(t) = \frac{1}{mc} \int_0^t F(t') dt'$ . Note that in nonrelativistic limit from (15) and (16) we obtain nonrelativistic wave functions in  $p$ - representation for free particle in homogeneous field for nonstationary [17] and stationary tasks correspondingly [18], i.e.

$$\lim_{c \rightarrow \infty} \phi_E(p, t) = \phi_{NE}(p, t) = e^{-\frac{i}{\hbar} \int_0^t \frac{1}{2m} (p - \delta_N(t) + \delta_N(t'))^2 dt'} \phi_{NE}^{(0)}(p - \delta_N(t), 0), \quad (17)$$

$$\lim_{c \rightarrow \infty} \phi_E^{(0)}(\chi, t) = \phi_{NE}^{(0)}(p, t) = \frac{1}{\sqrt{2\pi\hbar|F_0|}} e^{\frac{i}{\hbar F_0} (pE_N - \frac{p^3}{6m}) - \frac{iE_N t}{\hbar}}, \quad (18)$$

where  $\delta_N(t) = \int_0^t F(t') dt'$ .

The functions (15) are obeyed to conditions of orthogonality and fullness.

$$\int_{-\infty}^{\infty} \phi_E^*(p, t) \phi_{E'}(p, t) d\Omega_p = \delta(E - E'), \quad (19a)$$

$$\int_{-\infty}^{\infty} \phi_E^*(p, t) \phi_E(p', t) dE = \frac{1}{mc} \delta(\chi - \chi'). \quad (19b)$$

### 3. THE PARTICLE MOTION IN RELATIVISTIC CONFIGURATIONAL X- REPRESENTATION

Knowing wave function (15) of relativistic quantum particle in variable homogeneous field in  $p$ - representation, it is easy to find wave function in non-relativistic configurational  $x$ - representation. According to (4) we have

$$\Psi_E(x, t) = \frac{1}{2\pi\tilde{\lambda}\sqrt{|F_0|}} e^{\frac{ix\delta_R(t)}{\tilde{\lambda}}} J, \quad J = \int_{-\infty}^{\infty} e^{iQ(z)} dz, \quad (20)$$

where  $Q(z) = x_1 z/\tilde{\lambda} - Q_1(z)$ ,  $x_1 = x + E/F_0$  and  $Q_1(z) = \frac{mc^2}{\hbar} \int_0^t \text{ch}(z + \delta_R(t')) dt' + \frac{mc}{\tilde{\lambda}F_0} \text{sh}z$ .

Introducing the designations

$$\sigma(t) = \frac{mc^2}{\hbar} \int_0^t \text{ch}\delta_R(t') dt', \quad \gamma(t) = \frac{mc^2}{\hbar} \int_0^t \text{sh}\delta_R(t') dt' + \frac{mc^2}{\tilde{\lambda}F_0}, \quad (21)$$

we transform the expression for  $Q_1(z)$ :

$$Q_1(z) = \sigma(t)chz + \gamma(t)shz. \quad (22)$$

Further, we will be limited ourself by  $\sigma(t) \equiv \sigma > 0$  and  $\gamma(t) \equiv \gamma > 0$  values.

As  $chi\tilde{\lambda}\partial_x e^{ixz/\tilde{\lambda}} = chze^{ixz/\tilde{\lambda}}$ , so with taking under consideration integral formula for McDonald function  $K_\nu(a)$  [20]

$$\int_{-\infty}^{\infty} e^{iashx - px} dx = 2e^{-\frac{i\pi p}{2}} K_p(a), \quad |\text{Re } p| < 1, \quad a > 0, \quad (23)$$

one can rewrite (20) in following operator form:

$$J = 2e^{-i\sigma(t)chi\tilde{\lambda}\partial_x} e^{\frac{\pi x_1}{2\tilde{\lambda}}} K_{ix_1/\tilde{\lambda}}(\gamma(t)). \quad (24)$$

Here operator action  $e^{-i\sigma chi\tilde{\lambda}\partial_x}$  on arbitrary function  $f(x)$  is defined by following way

$$e^{-i\sigma chi\tilde{\lambda}\partial_x} f(x) = \frac{1}{2i\tilde{\lambda}} \int_{-\infty}^{\infty} e^{\frac{\pi(x'-x)}{2\tilde{\lambda}}} H_{i(x'-x)/\tilde{\lambda}}^{(2)}(\sigma) f(x') dx', \quad (25)$$

where  $H_\nu^{(2)}(z)$  is Gankel function of second kind. As  $\lim_{c \rightarrow \infty} mc^2(chi\tilde{\lambda}\partial_x - 1) = -\frac{\hbar^2}{2m}\partial_x^2$ , then formula (25) is “relativistic” analogue of known formula.

$$e^{\alpha\partial_x^2} f(x) = \frac{1}{\sqrt{4\pi\alpha}} \int_{-\infty}^{\infty} e^{-\frac{(x'-x)^2}{4\alpha}} f(x') dx'. \quad (26)$$

The derivations of (25) and (26) formulae are given in Application.

From (20) with help of (25) we obtain the integral representation for wave function  $\Psi_E(x, t)$

$$\Psi_E(x, t) = \frac{1}{2\pi i\tilde{\lambda}^2 \sqrt{|F_0|}} e^{\frac{ix\delta_R(t)}{\tilde{\lambda}} + \frac{\pi x_1}{2\tilde{\lambda}}} \cdot \int_{-\infty}^{\infty} e^{\pi'/\tilde{\lambda}} H_{ix'/\tilde{\lambda}}^{(2)}(\sigma) K_{i(x'+x_1)/\tilde{\lambda}}(\gamma) dx'. \quad (27)$$

This expression can be represented also in infinite sum form

$$\psi_E(x,t) = \frac{1}{2\pi\tilde{\lambda}\sqrt{|F_0|}} e^{\frac{ix\delta_R(t) + \pi x_1}{\tilde{\lambda}} + \frac{\pi x_1}{2\tilde{\lambda}}} \sum_{n=0}^{\infty} \frac{(-\sigma/2)^n}{n!} \sum_{k=0}^n (-1)^k C_n^k K_{n-2k+i x_1/\tilde{\lambda}}(\gamma). \quad (28)$$

For obtaining of more compact expression for wave function  $\psi_E(x,t)$  (20) let's consider separately the cases when  $\sigma < \gamma$  and  $\sigma > \gamma$ .

1) In case  $\sigma < \gamma$  the expression for  $Q_1(z)$  (22) can be represented in the form

$$Q_1(z) = A(t)sh(z + q_1), \quad (29)$$

where  $A(t) = \sqrt{\gamma^2 - \sigma^2}$  and  $thq_1 = \sigma/\gamma$ . Then with formula (23) we find that wave function has the following form:

$$\psi_E(x,t) = \frac{1}{\pi\tilde{\lambda}\sqrt{|F_0|}} e^{\frac{ix\delta_R(t) + x_1}{\tilde{\lambda}} + \frac{x_1}{\tilde{\lambda}}(\frac{\pi}{2} - iq_1)} K_{ix_1/\tilde{\lambda}}(\sqrt{\gamma^2 - \sigma^2}). \quad (30)$$

2) In case  $\sigma > \gamma$ , we represent  $Q_1(z)$  in the form

$$Q_1(z) = B(t)ch(z + q_2), \quad (31)$$

where  $B(t) = \sqrt{\sigma^2 - \gamma^2}$  and  $thq_2 = \gamma/\sigma$ . Then if we use the formula [20]

$$\int_{-\infty}^{\infty} e^{-iachx - px} dx = -i\pi e^{\frac{i\pi p}{2}} H_p^{(2)}(a), \quad -\text{Re}(ia) < 0, \quad (32)$$

then for wave function we obtain the following expression

$$\psi_E(x,t) = \frac{1}{2\pi\tilde{\lambda}\sqrt{|F_0|}} e^{\frac{ix\delta_R(t) + x_1}{\tilde{\lambda}} + \frac{x_1}{\tilde{\lambda}}(\frac{\pi}{2} - iq_2)} H_{ix_1/\tilde{\lambda}}^{(2)}(\sqrt{\sigma^2 - \gamma^2}). \quad (33)$$

Note that in case  $\sigma < \gamma$  the equation (6) is equivalent to recurrent relation for McDonald function

$$K_{\nu+1}(z) - K_{\nu-1}(z) = \frac{2\nu}{z} K_{\nu}(z), \quad z = \sqrt{\gamma^2 - \sigma^2},$$

and in case  $\sigma > \gamma$  equation (6) is equivalent to recurrent relation for Gankel function of second kind

$$H_{\nu+1}^{(2)}(z) + H_{\nu-1}^{(2)}(z) = \frac{2\nu}{z} H_{\nu}^{(2)}(z), \quad z = \sqrt{\sigma^2 - \gamma^2},$$

where  $\nu = i(x + E/F_0)/\tilde{\lambda}$ .

In nonrelativistic region where  $c \rightarrow \infty$  is only one wave function (30) exist. At  $t = 0$  from (30) we obtain the wave function of stationary task in  $x$ -representation [14]

$$\psi_E^{(0)}(x) = \frac{1}{\pi\tilde{\lambda}\sqrt{|F_0|}} e^{\frac{\pi x_1}{2\tilde{\lambda}}} K_{ix_1/\tilde{\lambda}}\left(\frac{mc^2}{\tilde{\lambda}F_0}\right). \quad (34)$$

The function (30) satisfies to conditions of orthogonality and completeness, i.e.

$$\begin{aligned} \int_{-\infty}^{\infty} \psi_E^*(x,t) \psi_{E'}(x,t) dx &= \delta(E - E'). \\ \int_{-\infty}^{\infty} \psi_E^*(x,t) \psi_E(x',t) dE &= \delta(x - x'). \end{aligned} \quad (35)$$

At obtaining of conditions (35) we use the following integral formula [20]

$$\int_{-\infty}^{\infty} e^{\pi x} K_{i\nu+ix}(b) K_{i\mu+ix}(c) dx = \pi e^{-\mu\pi} K_{i(\nu-\mu)}(b-c), \quad b > c > 0$$

and limit relation [14]  $\lim_{z \rightarrow 0} K_{ix}(z) = \pi\delta(x)$ .

Note that the comparison (27) with (30) and (33) leads us to following integral formulae

$$\int_{-\infty}^{\infty} e^{\pi x} H_{ix}^{(2)}(\sigma) K_{ix+iv}(\gamma) dx = 2ie^{-ivq_1} K_{iv}(\sqrt{\gamma^2 - \sigma^2}) \text{ при } \gamma > \sigma, \quad (36a)$$

$$= \pi e^{-ivq_2} H_{iv}^{(2)}(\sqrt{\sigma^2 - \gamma^2}) \text{ при } \sigma > \gamma, \quad (36b)$$

where  $thq_1 = \frac{\sigma}{\gamma}$  and  $thq_2 = \frac{\gamma}{\sigma}$ .

If in formulae (36) we go to limit  $\sigma \rightarrow 0$  (or  $\gamma \rightarrow 0$ ) and take under consideration the limit relations (which are consequences of integral representations (23) and (32))

$$\lim_{z \rightarrow 0} K_{ix}(z) = \pi\delta(x), \quad \lim_{z \rightarrow 0} H_{ix}^{(2)}(z) = 2i\delta(x), \quad (37)$$

and also the equality [21]  $H_{-v}^{(2)}(z) = e^{-i\pi v} H_v^{(2)}(z)$ , then (36) transforms to identities.

#### 4. OPERATOR IDENTITIES

In work [14] the operator solution of equation (9) leads to disclosure of chronological  $T$ -composition (12) and especially

$$Te^{-\frac{i}{\hbar} \int_0^t [H_0(y) - i\hbar a(t') \frac{\partial}{\partial y}] dt'} = e^{-\frac{i}{\hbar} \int_0^t H_0(y - \delta(t) + \delta(t')) dt'} e^{-\delta(t) \frac{\partial}{\partial y}}. \quad (38)$$

Analogically to this, we can solve the equation (6) describing the motion of quantum particle in relativistic configurational  $x$ -representation by operator method. In non-relativistic limit it transits into corresponding non-stationary Schrodinger equation in coordination representation describing the motion of free particle in variable field:

$$Te^{-\frac{i}{\hbar} \int_0^t [H_0(y) - i\hbar a(t') \frac{\partial}{\partial y}] dt'} = e^{-\frac{i}{\hbar} \int_0^t H_0(y - \delta(t) + \delta(t')) dt'} e^{-\delta(t) \frac{\partial}{\partial y}} e^{-\frac{i}{\hbar} (1-\lambda) \int_0^t H_0(y + \delta(t')) dt'}, \quad (39)$$

where  $\lambda = \lambda(t)$  is arbitrary time function.

It is obvious that equations (6) and (39) are private cases of equation of the following form

$$i\hbar \frac{\partial \nu(x,t)}{\partial t} = [H_0(-i\hbar \partial_x) - a(t)x] \nu(x,t). \quad (40)$$

The solutions of equations 99) and (40), i.e. functions  $u(y,t)$  and  $\nu(x,t)$  are connected with each other by Fourier transformation

$$\nu(x,y) = \frac{1}{\sqrt{2\pi\hbar}} \int_{-\infty}^{\infty} e^{ixy/\hbar} u(y,t) dy, \quad u(y,t) = \frac{1}{\sqrt{2\pi\hbar}} \int_{-\infty}^{\infty} e^{-ixy/\hbar} \nu(x,t) dx. \quad (41)$$

Let's write the symbol solutions of equation (40):

$$\nu(x,t) = \hat{U}(x,t) \nu(x,0), \quad (42)$$

where  $\hat{U}(x,t)$  is evolution operator of system in  $x$ -representation

$$\hat{U}(x,t) = Te^{-\frac{i}{\hbar} \int_0^t [H_0(-i\hbar \partial_x) - a(t')x] dt'}. \quad (43)$$

It connects with evolution operator in impulse representation  $\hat{U}(y;t)$  by (12) Fourier transformation, i.e.

$$\hat{U}(x,t)u(x,0) = \frac{1}{\sqrt{2\pi\hbar}} \int_{-\infty}^{\infty} e^{ixy/\hbar} \hat{U}(y,t)u(y,0)dy.$$

From here we obtain the following rule for opening of  $T$ -composition including in (43):

$$\begin{aligned} T e^{-\frac{i}{\hbar} \int_0^t [H_0(-i\hbar\partial_x) - a(t')x] dt'} &= \\ = e^{-\frac{i}{\hbar} \lambda \int_0^t H_0(-i\hbar\partial_x - \delta(t) + \delta(t')) dt'} e^{\frac{ix\delta(t)}{\hbar}} e^{-\frac{i}{\hbar} (1-\lambda) \int_0^t H_0(-i\hbar\partial_x + \delta(t')) dt'}. \end{aligned} \quad (44)$$

As operators are noncommutative in (44) then in further we can ignore the sign  $T$  and integrate on  $t$  in left part, i.e.

$$T e^{-\frac{i}{\hbar} \int_0^t [H_0(-i\hbar\partial_x) - a(t')x] dt'} = e^{-\frac{i}{\hbar} [tH_0(-i\hbar\partial_x) - \delta(t)x]} \quad (45)$$

Let's particular cases of formula (44)

1)  $H_0(-i\hbar\partial_x) = i\hbar\partial_x$ ,  $a(t) = a_0 = const$ . In this case  $\delta(t) = a_0 t$  and formula (45) has form:

$$e^{-t[\frac{i}{\hbar}y + a_0\partial_y]} = e^{-\lambda a_0(t\partial_y + \frac{it^2}{2\hbar})} e^{-\frac{it}{\hbar}y} e^{-(1-\lambda)a_0(t\partial_y - \frac{it^2}{2\hbar})}, \quad y = -a_0x. \quad (46)$$

2)  $H_0(-i\hbar\partial_x) = \frac{1}{2m}(-i\hbar\partial_x)^2 = -\frac{\hbar^2}{2m}\partial_x^2$ ,  $a(t) = a_0 = const$ . In this case formula (45) has the following form:

$$\begin{aligned} e^{\frac{i}{\hbar}t \left[ \frac{\hbar^2}{2m}\partial_x^2 + a_0x \right]} &= \\ = e^{-\frac{i}{\hbar} \lambda \int_0^t \frac{1}{2m} (-i\hbar\partial_x + a_0t + a_0t')^2 dt'} e^{\frac{ia_0t}{\hbar}x} e^{-\frac{i}{\hbar} (1-\lambda) \int_0^t \frac{1}{2m} (-i\hbar\partial_x + a_0t')^2 dt'} \end{aligned} \quad (47)$$

or after of integration has the form:

$$\begin{aligned} e^{\frac{i}{\hbar}t \left[ \frac{\hbar^2}{2m}\partial_x^2 + a_0x \right]} &= \\ = e^{\lambda \left( \frac{i\hbar}{2m}t\partial_x^2 + \frac{a_0t^2}{2m}\partial_x - \frac{ia_0^2t^3}{6m\hbar} \right)} e^{\frac{ia_0t}{\hbar}x} e^{(1-\lambda) \left( \frac{i\hbar}{2m}t\partial_x^2 - \frac{a_0t^2}{2m}\partial_x - \frac{ia_0^2t^3}{6m\hbar} \right)}, \end{aligned} \quad (48)$$

that agrees with results of works [22,23].

2) Let's also give "relativistic" analogue of formula (48). For this let's take  $H_0$  in following form  $H_0(-i\hbar\partial_x) = mc^2 \chi \lambda \partial_x$ ,  $a(t) = a_0 = const$ . Then following formula will be relativistic analogue of (48)

$$e^{-\frac{i}{\hbar}t[mc^2ch\hat{\nu}\partial_x - a_0x]} = e^{-\lambda\frac{imc^2}{\hbar}[a(t)ch\hat{\nu}\partial_x + \beta(t)sh\hat{\nu}\partial_x]} e^{\frac{ia_0t}{\hbar}x} e^{-(1-\lambda)\frac{imc^2}{\hbar}[\alpha(t)ch\hat{\nu}\partial_x - \beta(t)sh\hat{\nu}\partial_x]} \quad (49)$$

where

$$\alpha(t) = \int_0^t ch \frac{a_0 t'}{mc} dt' = \frac{mc}{a_0} sh \frac{a_0 t}{mc}, \quad \beta(t) = \int_0^t sh \frac{a_0 t'}{mc} dt' = \frac{mc}{a_0} \left( ch \frac{a_0 t}{mc} - 1 \right). \quad (50)$$

At  $c \rightarrow \infty$  (49) transforms into (48).

## 5. CONCLUSION

In present work we study the one-dimensional motion of free relativistic quantum particle in variable homogeneous field. This is one of the exactly solvable non-stationary tasks. The task is formulated within framework of finite-difference relativistic quantum mechanics. The system wave function in relativistic configurational  $x$ -representation satisfies to finite-difference equation and in impulse representation satisfies to differential one. The connection between canonically conjugate  $x$ - and  $p$ -representations is carried out with the help of Fourier relativistic transformation. The motion equation has been solved (as in  $p$ -representation and in  $x$ -representation) with the use of system evolution operator which is defined over  $T$ -product.

The solution of certain class of differential equations in partial derivatives of first order describing the motion in  $p$ -representation and solution of certain class of differential and finite-difference equations describing the particle motion in variable homogeneous field in  $x$ -representation has also been found.

We have established the exact expression of wave functions in both impulse and configuration representations. It is shown that firstly, they satisfy to conditions of orthogonality and completeness, secondly, they have the right nonrelativistic limit. The operator formulas analogous to known Beyker-Hausdorf formula are obtained. These formulas give the opening rule of chronological  $T$ -product. In particular cases they reproduce the known formulas.

We hope that obtained operator formulae allow us to formulate the quantum-mechanical analogues of Vic theorem, well known in quantum field theory and to develop the perturbation theory.

The results of the given work can be applied at study of relativistic quantum particle motion in variable homogeneous magnetic, electric and gravitational fields.

Note that other nonstationary quantum-mechanical tasks can be solved by operator method. For example, one can show the task about harmonic oscillator.

The knowing of evolution operator expression over  $T$ -product allows us to find the propagators of simple algebraic way (see [23]).

## APPLICATION

1. Let's deduce formulae (26). For  $f(x)$  function we have:

$$f(x) = \frac{1}{\sqrt{2\pi}} \int_{-\infty}^{\infty} g(y) e^{ixy} dy, \quad g(y) = \frac{1}{\sqrt{2\pi}} \int_{-\infty}^{\infty} f(x) e^{-ixy} dx. \quad (II.1)$$

As

$$e^{\alpha\partial_x^2} e^{ixy} = \sum_{n=0}^{\infty} \frac{\alpha^n}{n!} \partial_x^{2n} e^{ixy} = \sum_{n=0}^{\infty} \frac{(-\alpha y^2)^n}{n!} e^{ixy} = e^{-\alpha y^2 + ixy},$$

then we have

$$e^{\alpha\partial_x^2} f(x) = \frac{1}{\sqrt{2\pi}} \int_{-\infty}^{\infty} g(y) e^{-\alpha y^2 + ixy} dy = \frac{1}{2\pi} \int_{-\infty}^{\infty} dx' f(x') \int_{-\infty}^{\infty} e^{-\alpha y^2 - i(x'-x)y} dy.$$

Using formulae [20]

$$\int_{-\infty}^{\infty} e^{-px^2 - qx} dx = \sqrt{\frac{\pi}{p}} e^{q^2/4p}, \quad \text{Re } p > 0 \quad (II.2)$$

to integral on  $y$  we obtain formula (26).

Formulae (26) can be deduced by other method. According to (II.2) for operator  $e^{\alpha\partial_x^2}$  one can write the following expression:

$$e^{\alpha \hat{\partial}_x^2} = \frac{1}{\sqrt{4\pi\alpha}} \int_{-\infty}^{\infty} e^{-\frac{x'^2}{4\alpha} + x' \hat{\partial}_x} dx'. \quad (\text{II.3})$$

Now we can easily obtain the formulae (26):

$$\begin{aligned} e^{\alpha \hat{\partial}_x^2} f(x) &= \frac{1}{\sqrt{4\pi\alpha}} \int_{-\infty}^{\infty} e^{-\frac{x'^2}{4\alpha} + x' \hat{\partial}_x} f(x) dx' = \\ &= \frac{1}{\sqrt{4\pi\alpha}} \int_{-\infty}^{\infty} e^{-\frac{x'^2}{4\alpha}} f(x+x') dx' = \frac{1}{\sqrt{4\pi\alpha}} \int_{-\infty}^{\infty} e^{-\frac{(x'-x)^2}{4\alpha}} f(x') dx'. \end{aligned}$$

2. Let's deduce formulae (25). Taking under consideration  $i\hbar \partial_x e^{ix\chi/\hbar} = -\chi e^{ix\chi/\hbar}$  we have:

$$\begin{aligned} e^{-i\alpha \hbar i \hat{\partial}_x} f(x) &= \frac{mc}{\sqrt{2\pi\hbar}} \int_{-\infty}^{\infty} g(\chi) e^{-i\alpha \hbar i \hat{\partial}_x} e^{\frac{ix\chi}{\hbar}} d\chi = \\ &= \frac{mc}{\sqrt{2\pi\hbar}} \int_{-\infty}^{\infty} g(\chi) e^{-i\alpha \hbar \chi + \frac{ix\chi}{\hbar}} d\chi = \frac{1}{2\pi\hbar} \int_{-\infty}^{\infty} dx' f(x') \int_{-\infty}^{\infty} e^{-i\alpha \hbar \chi - \frac{ix\chi}{\hbar}(x'-x)} d\chi. \end{aligned} \quad (\text{II.4})$$

For integral calculation on  $\chi$  let's apply the formulae (32). As a result we obtain formula (25).

3. Analogously to (II.4) one can show the following expression:

$$e^{i\gamma sh \hat{\partial}_x} f(x) = \frac{1}{\pi\hbar} \int_{-\infty}^{\infty} e^{\frac{\pi(x-x')}{2\hbar}} K_{i(x-x')/\hbar}(\gamma) f(x') dx'. \quad (\text{II.5})$$

- 
- |  |  |
|--|--|
| <p>[1] V.G. Kadyshevsky, R.M. Mir-Kasimov, N.B. Skachkov. Nuovo Cim. 55A, 1968, 233-257.</p> <p>[2] V.G. Kadyshevsky, R.M. Mir-Kasimov, M. Freeman. Yad. Fiz. 9, 1969, 646.</p> <p>[3] M. Freeman, M.D. Mateev, R. M. Mir-Kasimov. Nucl. Phys B12, 1969,197.</p> <p>[4] A.D. Donkov, V.Q. Kadishevskiy, M.D. Mateev, R.M. Mir-Kasimov. Theor. Math. Phys. 8, 1071, 61.(In Russian)</p> <p>[5] V.G. Kadyshevsky, R.M. Mir-Kasimov, N.B. Skachkov, Phys. Elem. Part. At. Nucl.2, 1972, 635.</p> <p>[6] N.M. Atakishiyev, R.M. Mir-Kasimov, Sh.M. Nagiyev, TMF 44, 1980, 47-62.(In Russian)</p> <p>[7] N.M. Atakishiyev, R.M. Mir-Kasimov, Sh.M. Nagiyev. Ann. Phys. (Leipzig) 42_1985, 25.</p> <p>[8] Sh.M. Nagiyev, J. Phys. A: Math. Gen. 21, 1988 2559.</p> <p>[9] Sh.M. Nagiyev, Theor. Math. Phys. 80, 1989, 697.</p> <p>[10] E.D. Kagrmanov, R.M. Mir-Kasimov, S.M. Nagiyev, J. Math. Phys. 31, 1990, 1733.</p> <p>[11] Sh.M. Nagiyev, Theor. Math. Phys. 102, 1995, 180.</p> <p>[12] R.A. Frick, Eur. Phys. J. C 28, 2003, 431.</p> | <p>[13] Sh.M. Nagiyev, E.I. Jafarov, R.M. Imanov, L. Homorodean, Phys. Lett. A 334, 2005, 260.</p> <p>[14] Sh.M. Nagiyev, S.I. Guliyeva. Phys. Lett. A373, 2009, 2810-2813.</p> <p>[15] I.S. Shapiro, DAN SSSR 106, 1956, 647.(In Russian)</p> <p>[16] Sh.M. Nagiyev, K.Sh. Dhafarova, S.I. Qulieva, J.of Qafqaz Univ., 2012 (v pechati).(In Russian)</p> <p>[17] L.D. Landau, E.M. Lifshich. Kvantovaya mexanika. M:Nauka, 1974.(In Russian)</p> <p>[18] V.V. Dodonov, V.I. Manko, O.V. Shakhmistova. Phys. Lett. A102, 1984, 295-297.</p> <p>[19] B.V. Medvedev, Nachala teoriticheskoy fiziki, M: Nauka,1977.(In Russian)</p> <p>[20] A.P. Prudnikov, Yu.A. Bichkov, O.I. Marichev, Integrali iryadi. Elementarnie funkchii. M: Nauka, 1981.(In Russian)</p> <p>[21] Q. Beytmen, A. Erdeyn. Visshie transchendentnie funkchii, t.2, M.: Hayka, 1974.(In Russian)</p> <p>[22] J.Katriel, J. Phys. A:Math. Gen. 16, 1983, 4171-4173.</p> <p>[23] W.Qinnou, J.Phys. A: Math. Gen. 20, 1987, 5041-5044.</p> |
|--|--|

Received: 02.10.2012

## FORMATION OF LATERAL HOMOGENEOUS STAIN ETCHED POROUS SILICON WITH ACETIC ACID AT OXIDANT INSUFFICIENCY

F.A. RUSTAMOV, N.H. DARVISHOV, M.Z. MAMEDOV,  
E.Y. BOBROVA, H.O. GAFAROVA

*Baku State University, Institute for Physical Problems,, Semiconductor Physics Division, AZ-1148,  
Z. Khalilov, 23, Baku, Azerbaijan  
e-mail: farhad.rustamov@bsu.az*

The influence of acetic acid on the process of stain etched porous silicon formation on the restricted surface area in etching solution HF/HNO<sub>3</sub>/CH<sub>3</sub>COOH at oxidant insufficiency have been investigated. It is shown, that with increasing of acetic acid concentration the incubation time increases, the rate of reaction falls, the evolution of bubbles decreases and the lateral homogeneity of stain etched porous silicon improves. It is found, that the process of stain etched porous silicon formation is accompanied with the evolution of two types of bubbles, which differ in their sizes, surface distribution and ability to stick to surface. The optimal concentration of etching solution, in which reaction occurs without bubbles evolution, is determined and very homogeneous, uniformly coloured specular porous silicon layers are obtained. In spite of the fact that the etching was performed on the restricted area of wafers surface the influence of boundaries did not occur and the pore formation process has a very good repeatability and reproducibility. It is shown that in this etchant composition the porous silicon formation does not depend on the volume of etching solution. It is also shown, that the method of final treatment of the wafers surface before etching without changing the pore formation rate essentially affects the incubation time. The investigations of photoluminescence emission and excitation spectra showed that in spite of independence of photoluminescence maximum position, optical bandgap of porous silicon decreases with increasing etching time.

**Keywords:** porous silicon; stain etching; acetic acid, homogeneity; photoluminescence

**PACS:** 81.05.Rm; 81.65.Cf; 78.40.Fy; 78.55.-m; 78.55.Mb

### 1. INTRODUCTION

Potential of porous silicon (PS) for use in Si-based optoelectronic integrating circuits attracts the attention of researchers since the discovery of unique properties of this material [1,2]. Most important of these are their optical properties, particularly intensive red-orange photo- and electroluminescence in visible spectra [1-4]. The studies show large perspectives in the use of nanoporous silicon layers as sensors and antireflecting coating for solar cells [5-8].

The layers of nanoporous silicon are obtained both by electrochemical and pure chemical etching [3,4]. In case of anodization the Si substrate is a supplier of holes needed for PS formation, but in stain etching the holes are generated in solution during the HNO<sub>3</sub> dissociation. This is a main reason, that stain etched PS layers, obtained by chemical etching are rather thin but possesses a significant porosity. While a mechanism of PS formation is identical in both cases, the method of pure chemical etching is simpler and more technologically suitable for a conventional processing cycle of Si wafers. It is sufficient to immerse the wafer into the appropriate etching solution for a desired time. This technology eliminates the need for application of the ohmic contact on the opposite side of the wafer and performs etching without applied voltage. Moreover, in this method, evens very thin layers of PS (20 – 200 nm) are luminescent, so the problem of cracking does not exist any longer [3,4,9].

It is known that Si etching reaction in fresh HF/HNO<sub>3</sub> solutions is autocatalytic and the incubation period can range from few seconds to 30 min depending on type and value of Si wafers, conductivity and etchant composition [3,10]. The process is followed by bubbles evolution, which affects the morphology and lateral homogeneity of obtained samples. In electrochemical etching methanol, ethanol, isopropanol or acetic acid is

added to etching solution to minimize bubbles evolution and prevent bubbles adhesion. It is not desirable to add these alcohols to the solution during the chemical etching in HF/HNO<sub>3</sub> mixture since they enter into reaction with the etchant [10]. Usually at stain etching acetic acid (CH<sub>3</sub>COOH) is used for this purpose. It has low surface tension and low dielectric constant in comparison to those of water. It improves on the one hand the wettability of hydrophobic Si surface and promotes the yield of unwanted bubbles [3,4], but on the other hand, reducing the degree of HNO<sub>3</sub> molecules dissociation leads to increase of etchant reactivity.

Pre-cleaning methods of the wafers surface from contaminants and etching of natural oxide film influence both the incubation period and lateral homogeneity of PS layers. For pre-cleaning of wafers the washing in organic solvents, such as acetone, methanol, ethanol, isopropanol and deionized water [3,4,10], sulfuric peroxide mixture at 80°C for 5 min is commonly used [11,12]. Ultrasonic cleaning in these solvents are also applied [13,14]. There are various methods to remove the natural oxide film and reduce the surface defects: final treatment in 5% or 50% aqueous solution of HF during 30 s – 1.5 hours [3,4,11,14,15], in HF:HNO<sub>3</sub>:CH<sub>3</sub>COOH (1:4:3 volume) solutions for 2 min for chemical polishing [16], treatment in NaOH (30% wt) at 80°C for 10 min [5,17] or KOH (50%) [6, 18] to reduce surface defects, oxidized in hot HNO<sub>3</sub> and oxide remove in 50% HF for 30 s [15].

The etchant composition for obtaining the porous silicon is much diversified too [3,4]. The selection of composition is defined by substrate conductivity, incubation period, reproducibility, lateral homogeneity, luminescence and antireflection properties. Now, for formation of stain etched PS two types of solutions are mainly used: the etching solutions with insufficiency of HF [3,4,15,19,20] and solutions with insufficiency of

oxidant [4,5,8,17,19,20]. In solutions with insufficiency of HF, the PS formation process is controlled by diffusion of HF molecules to surface of wafer, but in solutions with insufficiency of oxidant, it is controlled by rate of Si oxidation.

Such variety of methods of wafer surface treatment and application of various etchant compositions are related to poor reproducibility of experiments and complication of obtaining of lateral homogeneous stain etched PS films without traces of sticking bubbles. Usually obtained PS samples have traces of sticking bubbles and laterally inhomogeneous. The interference bands are observed on their surfaces because of the films thickness inhomogeneity. Such inhomogeneity is observed especially during the etching of the wafer surface in restricted area.

Reproducible porous silicon layers are obtained in solutions with insufficiency of oxidant [5,8,17,20]. In etching solution HF:HNO<sub>3</sub>:CH<sub>3</sub>COOH (1000:1 or 1200:1 volume), i.e., at oxidant insufficiency, the PS formation process is controlled by rate of Si oxidation by nitric acid. Here, the reaction occurs spontaneously, whatever the type and conductivity of Si wafers, and it is characterized by good reproducibility and more thick layers. However, even in this case, at large etching times (greater than 1 minute) the bubbles, accompanying the process, stick to the surface of the sample and break its homogeneity. In addition, during formation of PS on the restricted area of the surface, which is especially important for patterning of the surface, the influence of boundaries is observed. Etching on a selected surface leads to the appearance of interference rings, showing an inhomogeneous PS film thickness.

To use porous silicon in various optoelectronic devices, it is important to develop technologies for formation of luminescence PS films having a high degree of reproducibility, unaffected by bubbles traces, homogeneous along the surface and through the thickness.

The purpose of the given work is to investigate the influence of acetic acid in HF/HNO<sub>3</sub> solutions at oxidant insufficiency to sticking ability of bubbles, surface homogeneity and luminescence properties of stain etched porous silicon formed on the restricted surface area.

## 2. EXPERIMENTAL DETAILS

In the present work, the PS layers were obtained by stain etching on the monocrystalline p- and n- type Si wafers, polished on each side, with resistivity from 0.1 to 40 Ω·cm and 0.1 to 7.5 Ω·cm, respectively. As etchant a solution of HF (50%), HNO<sub>3</sub> (65%) and acetic acids in volume proportion of HF:HNO<sub>3</sub>:CH<sub>3</sub>COOH from 1200:1:0 to 1200:1:1800 was used. The etching was performed only on the one side of wafers in Teflon cell. The use of chemically resistant seal has made it possible to avoid the influence of wafers borders and carry out the etching only on restricted area of wafer. The etched area is 1 cm<sup>2</sup>. Before the etching, the wafers were immersed into organic solvents to remove the organic contaminations. At first, the wafers were immersed into acetone for 50 min and then washed in bidistilled water. Then the wafers were immersed into 15% alcohol solution of HF for 1.5 hours to remove natural oxide layer and after washing in bidistilled water, they were blown by N<sub>2</sub>

jet. The stain etching was performed at daylight illumination at room temperature. After etching, the samples were washed in bidistilled water, then in isopropanol and were dried by N<sub>2</sub> jet.

Morphology of PS and porous layer thickness has been inspected by interference microscope MII – 4 and visually on the bases of Rollet's table of interference colours [21]. This method enables to perform in situ checking of the film thickness during PS formation. The photoluminescence (PL) and photoluminescence excitation spectra (PLE) have been investigated under room temperature. The PL was excited by light of Xenon lamp DKSL-1000, transmitted through monochromators SPM-2 and IKS -12 in geometry "on reflection". Signals were recorded by cooled photoelectric multiplier FEU-79. Photoluminescence spectra have been corrected on sensibility of spectrometric system.

## 3. RESULTS

Fig.1a shows a typical stain etched PS layer of p-type Si wafer obtained in a restricted surface by etching in a solution 1200:1:0 for more than 60 seconds. The incubation time in this concentration is about 30 sec. It can be seen, that the surface of PS is covered with traces of bubbles and the interference rings. These rings indicate nonuniformity of PS layers in thickness. Reaction always starts at the boundaries of the region and extends to the center. Bubbles appear in a minute after the start of the reaction and they do not detach from the surface.

On addition of acetic acid to solution up to concentration 1200:1:600 this pattern remains almost unchanged, although the incubation period is increased by 1 min. At a concentration 1200:1:600 the reaction course changes dramatically. The reaction starts at once on the entire surface and there are no interference rings. With thickening of the PS a simultaneous change of colors takes place on the surface. Fig.1b shows a typical sample obtained in this regime. Although the absence of the interference rings and the uniform etching indicate the homogeneity over the PS layer thickness, there are many traces of sticking bubbles on the surface of samples. At this composition, the reaction is accompanied with the bubbles evolution, impairing the lateral homogeneity of PS layers. With further increase of acetic acid concentration the incubation period increases and gradually decreases the amount of sticking bubbles.

Most of bubbles formed during the reaction start to detach spontaneously. At this stage, we can see that at the start of reaction, as well as in electrochemical etching [1,2], very small bubbles are formed and then detach. With further etching, the evolution of small bubbles almost stopped and a few large bubbles appear. The number of these large bubbles does not change with further etching and they rarely detached from the surface and, if they detach, in their place immediately new bubbles appear. In terms of homogeneity, the best results were obtained when the concentration of etching solution is 1200:1:1200. Here, the incubation period increases up to 9 minutes. The reaction starts at once on the entire surface and proceeds without bubbles evolution even 30 min after the start. In situ observation shows a simultaneous change of PS surface colors without any interference bands. After completion of the etching and

drying the sample the laterally homogeneous and uniformly colored specular PS layers are obtained (Fig.1. c–f). From this figure, it can be seen that with increasing etching time an uniform change in color of samples occurs and this indicates an increase in the thickness of the PS layer. Investigations by Rollet's table of interference colors and MII-4, show that at these compositions of the etchant it is possible to obtain high quality samples with thickness of up to 300 nm. It is very important that even at the boundaries of the samples nonuniformity of etching does not appear.

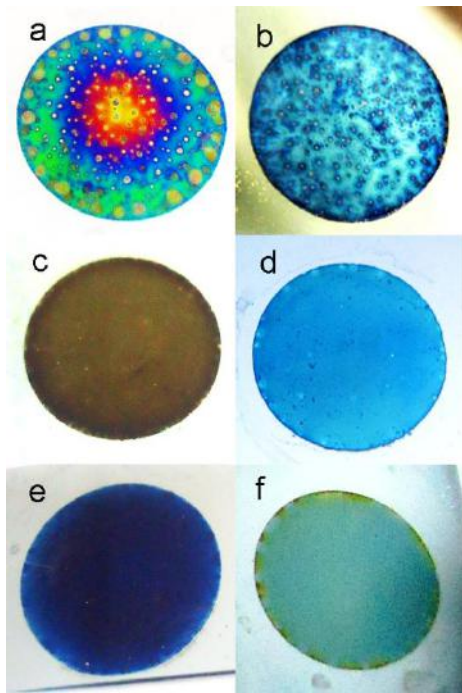


Fig.1. Stain etched PS layers formed in HF:HNO<sub>3</sub>:CH<sub>3</sub>COOH solutions with various compositions: a) 1200:1:0, b) 1200:1:600, c), d), e) and f) 1200:1:1200 for 1.5 min, 9 min, 30 min and 45 min, correspondingly.

The influence of etching solution volume on the formation of PS has been studied too. Experiments were carried out with solutions in volume from 0.2 cm<sup>3</sup> to 6 cm<sup>3</sup>, when the height of the column of solution on the wafer varied from 2 to 60 mm, respectively. No change in the incubation period, either in the reaction rate, and neither in the lateral homogeneity of the obtained samples was observed.

The influence of the final treatment of wafers prior to the reaction on the incubation period, the reaction rate of pore formation and the homogeneity of obtained PS layers has also been studied. After washing in acetone, final treatment of wafers was carried out in three different ways: in 15% alcohol solution of HF, in 15% aqueous solution of HF and in pure isopropanol. The first two solutions remove the natural oxide from the surface of the wafers, but third solution does not remove the oxide layer and is intended only for cleaning of the surface. It has been found that final treatment method significantly affects the incubation time. In aqueous solution of HF, the incubation period was 2 min, in an alcohol solution it was

9 min and in pure isopropanol - 12 min. It must be noted that the reaction rate of pore formation does not depend on the method of surface treatment and in all cases the homogeneous mirror-like PS layers luminescent at room temperature were obtained. Photoluminescence peaks in all cases coincided. The same solution was used for etching of the n-type wafers too. In these wafers, laterally homogeneous layers of PS also were obtained despite of oscillatory nature of the change in PS thickness at the initial stage of etching.

All the samples of porous silicon show visible luminescence at room temperature. Excitation was induced by wave of 320 nm. Fig.2 shows photoluminescence spectra of p-type samples with 20 Ω·cm resistivity measured after four days exposure at ambient conditions. The samples have different etching time beyond incubation time: 1 - 1.5 min, 2 - 9 min, 3 - 30 min, 4 - 45 min. It can be seen from Fig.2 that with increasing etching time the position of PL peak is shifted slightly - at first from 1.84 eV to 1.81 eV and then back to 1.84 eV. The maximum intensity is observed for samples in which the reaction continued for 9 min. The halfwidth of spectra for all samples were about 0.4 eV.

PLE spectra at maximum of PL have been measured for all obtained samples (Fig.3). Changing the maximum of PLE spectra as a function of etching time is nonmonotonic. At first, maximum increases from 3.88 eV to 4 eV and then decreases down to 3.76 eV. Since all investigated samples were rather thin (d < 300 nm), low energy wing of PLE spectra should be proportional to absorption coefficient [22-24] and analysis of these spectra can give information about optical bandgap.

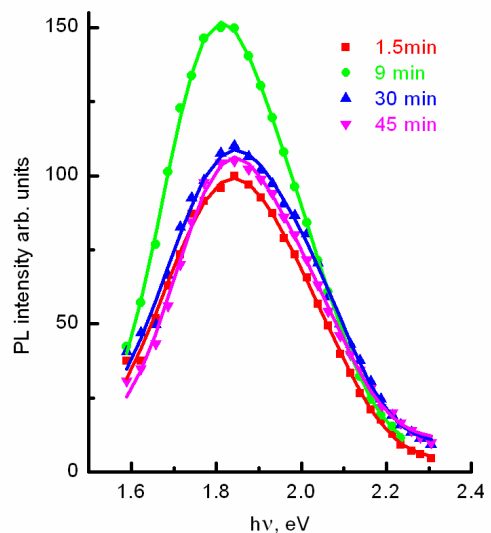


Fig.2. PL spectra of stain etched PS layers formed during various time and exposed 4 days at ambient conditions.

Fig.4 shows the dependencies of  $(I_{PLE}h\nu)^{1/2}$  versus  $h\nu$ . The straight lines indicate the extrapolation to the low energy region and there points of intersection with  $h\nu$  axis allow estimation of bandgap value. It can be seen from Fig.4 the bandgap value nonmonotonically decreases from 2.6 eV to 2.2 eV with increasing etching time.

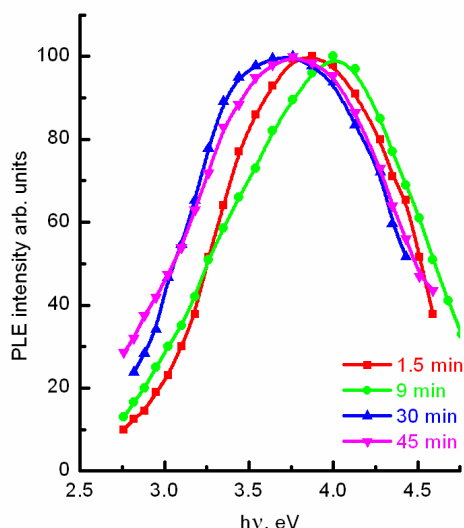


Fig.3. PLE spectra of stain etched PS layers formed during various time and exposed 4 days at ambient conditions.

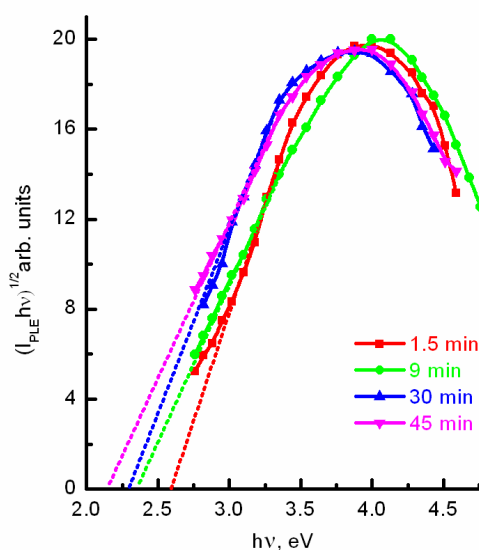


Fig.4. Dependencies of  $(I_{PLE} hv)^{1/2}$  versus  $hv$  and their extrapolation by straight line at low energy region for stain etched PS layers formed during various time and exposed 4 days at ambient conditions.

#### 4. DISCUSSION

It is known that composition and concentration of etching solution strongly affect both the process of etching and morphology of porous silicon. Depending on concentration of HF:HNO<sub>3</sub>:CH<sub>3</sub>COOH solutions the etching can lead to either polishing surface or PS formation. In microelectronics these solutions are usually used for final polishing of Si wafers surface. Addition of acetic acid helps to reduce the reaction rate. To obtain the

porous silicon the acetic acid is usually added to increase the wettability of hydrophobic Si surface and for best filtration of pores. Addition of acetic acid leads to the change of HNO<sub>3</sub> molecules dissociation degree and concentration of NO<sub>2</sub> molecules in solution, which carry out the effective oxidation of Si to supply the holes needed for reaction.

When performing the reaction on a restricted surface it is natural to expect the influence of boundaries. The appearance of interference rings in the solution to a concentration 1200:1:600 associated with the inhomogeneous distribution of the oxidant on the surface. The reaction always starts at the boundaries of the sample and slowly extends to the center. There are many traces of sticking bubbles on the wafers surface. With increasing of acetic acid concentration the incubation time increases and rate of reaction decreases. This tends to equalize the concentration of oxidizing agent over the entire surface. That is why the reaction starts at once on the entire surface, interference rings disappear and uniform staining specular layers of PS are obtained.

At concentration above 1200:1:600 the low rate of the reaction makes it possible to distinguish two types of bubbles, formed during the formation of PS layer. These bubbles differ by size and ability to stick to surface. Initially, small bubbles appear on the entire surface and are easily detached from the surface with increasing concentration of acetic acid. With increasing etching time, the evolution of these small bubbles stop and in some parts of surface the larger bubbles appear. These large bubbles hardly detach from the sample surface, even at very violent shaking of the etching cell. If these large bubbles are detached from the surface then new bubbles immediately appear. This behavior may be explained by etching irregularities or defects in monocrystalline silicon wafers [25]. It is known that the electrochemical method of PS formation is always succeeded by the evolution of hydrogen bubbles. In formation of stain etched PS, applying HNO<sub>3</sub> as an oxidant, evolved gases consist of mixtures H<sub>2</sub> and NO<sub>x</sub> [26]. The evolution of two types of bubbles may be associated with composition of these bubbles.

It has been mentioned earlier that the best results in terms of repeatability, reproducibility and lateral homogeneity of the PS layers in restricted area are obtained at concentration 1200:1:1200. In this case, the reaction proceeds without evolution of any bubbles and uniformly colored, laterally homogeneous, mirrored samples are formed even at the etching time more than 30 min.

It is usually assumed, that for obtaining of homogeneous stain etched PS layers, the surface of the wafers should be hydrophilic. By adding acetic acid to the etching solution and increasing incubation period, we were able to investigate the effect of cleaning solutions composition, used for final treatment of wafers, on the formation of PS. It was found, that in the treatment of wafers with an aqueous solution of HF the incubation time is significantly shorter than that in the treatment of wafers with an alcohol solution of HF or pure isopropanol. Also it has been found that with increasing incubation time an evolution of the bubbles are reduced and homogeneity of PS layers is improved. Thus, for a

given composition of the etching solution the initial hydrophilicity does not matter, only the depth of the surface treatment and its roughness is important. This is probably due to the fact that given etchant has sufficient acetic acid to eliminate the need for surfactants and an initial hydrophilicity of wafers surface.

All stain etched PS samples had visible photoluminescence at room temperature. The dependence of PL intensity and its peak position on etching time differ from that obtained by the electrochemical method of PS formation. Usually, in anodized PS, the PL peak shifted over etching time to high-energy region [1-4] and its intensity increases. This shift of PL peak is associated with an increase of porosity and so, with decrease in particle size of Si nanocrystallites. The increase in intensity is explained by an increase in layer thickness of porous silicon, i.e., with increasing number of emitting centers. In our case (Fig. 2), with increasing etching time the PL maximum shifts only slightly, initially to low energy and then to high-energy region. Such independence of PL maximum is well known [10,18,26] and indicates a very weak dependence of PL peak position on the etching time in stain etched PS. At the same time, the PL intensity at first increases and then decreases.

This difference in behavior of PL spectra of porous silicon is obtained by electrochemical and purely chemical etching methods can be explained by considering the difference in the processes of thickening of the PS layers. During the electrochemical etching, the PS layer thickness increases monotonically with increasing etching time. The upper boundary of the porous silicon subjected to more prolonged exposure to water or an alcohol solution of HF becomes more porous. This upper boundary is almost none etched off in etchant, there is a gradient of porosity, and hence, of particle size of the Si nanocrystallites. The particle sizes of crystallites on the upper side of porous layer, are reduced, resulting in a PL peak shift to high-energy region and, as consequence, the bandgap broadening. The chemical etching solution contains an oxidizing agent, so the process of thickening of the PS layer is determined by the balance between the etching off the upper layer of PS and pore formation at the boundary of porous silicon/bulk silicon. At the initial stage of etching the process of pore formation dominates, the layer thickness increases, although the upper boundary layer is etched off too. This leads to an increase in PL intensity. But since the upper boundary is subject to more prolonged exposure an etchant containing an oxidizing agent, it is more porous and over time is etched off this highly porous area of PS. Therefore, with increasing etching time Si nanocrystallites of smaller sizes are etched, and therefore there is no shift of PL maximum to high energy region. With increase of etching time the etching rate of upper highly porous PS boundary increases too. Equilibrium is established between the processes of upper boundary etching and pore formation and this greatly slows down the thickening of PS. Since all this time highly porous upper boundary of PS is etched off, there is no shift to the high-energy region of PL peak position.

However, investigations of only PS photoluminescence spectra are not sufficient to prove the

change in the particle size of Si nanocrystallites and, so, the bandgap due to the presence of different possible channels of radiative recombination. Therefore, PL excitation spectra have been investigated in each case (Fig.3, 4). One major restriction of this method in investigation of the bandgap and nanocrystallite sizes may be the thickness of PS layer. It is known that PLE intensity is proportional to the absorption coefficient only on condition of  $\alpha d \ll 1$  ( $\alpha$  - the absorption coefficient,  $d$  - the thickness of PS layer). But stain etched PS layers are usually very thin and the use of this method becomes suitable. It can be seen from Fig. 3 with increasing etching time irregular shifting of PLE maxima is observed. This shift itself indicates the change in optical bandgap of the nanocrystallites, and hence its size, with increasing etching time. For more detailed definition of bandgap value and absorption behavior we show  $(I_{PLE}h\nu)^{1/2}$  as a function of  $h\nu$  in Fig.4. The straight lines indicate the extrapolation in the low energy region. Good extrapolation of these dependencies indicates indirect behavior of absorption, which does not depend on etching time. The intersection points of extrapolation straight lines with the  $h\nu$  axis, showing the optical bandgap, shift to low energy region with increasing etching time. This indicates the fact that with increasing etching time the optical bandgap nonmonotonically decreases, meaning that average particle size of Si nanocrystallites in PS layer increases. That is why PL peak does not shift to high-energy region with increasing etching time. However, difference in the measured values of optical bandgap and the maximum values of the PL spectra is clearly seen. This difference is also observed in as-anodized PS [24]. This indicates that although the absorption responsible for visible PL occurs in Si nanocrystallites, the radiative recombination occurs in boundary oxide layer.

## 5. CONCLUSIONS

The influence of acetic acid on the formation of stain etched PS in etching solution of HF/HNO<sub>3</sub>/CH<sub>3</sub>COOH at oxidant insufficiency in the restricted area has been investigated. It is shown, that with increasing concentration of acetic acid the incubation period increases, the rate of pore formation and bubbles evolution decreases and it improves the lateral homogeneity of PS layers. Slower rate of reaction revealed the evolution of two types of bubbles differing in size, allocation on the surface and ability to stick to surface and so, perhaps, in their composition. It has been revealed, that in concentration of the etching solution 1200:1:1200 the reaction occurs without evolution of bubbles and very homogeneous uniformly colored specular PS layers of different thicknesses are obtained. Although the etching was carried out on a restricted surface area of wafers, the influence of boundaries did not occur and the process of pore formation had a very good repeatability and reproducibility. It was found that in this composition of the etching solution, process of pore formation does not depend on etchant volume and formation of PS layers can be performed even with a small amount of it. We have also found that the method of final treatment of the wafers surface, without changing the rate of pore formation, essentially affect the incubation time. All obtained samples showed visible

photoluminescence, the maximum position of which, in contrast of anodized PS, hardly changed with increasing etching time. PLE spectra study showed that with

increasing etching time the optical bandgap decreases, i.e., the average size of Si nanocrystallites increases.

- 
- [1] V. Lehmann, *Electrochemistry of Silicon*, Willey VCH, New-York NY, 2002.
- [2] L.T. Chanham, *Appl. Phys. Lett.* 57 (1990) 1046.
- [3] L.T. Chanham, *Properties of porous silicon*, EMIS Data Review Series No. 18, London, 1997.
- [4] V. Lehmann, U. Gosele, *Appl. Phys. Lett.* 58 (1991) 856.
- [5] L. Schirone, G. Sotgiu, M. Montecchi, *J. Lumin.* 80 (1999) 163.
- [6] R.R. Bilyalov, R. Ludemann, W. Wettling, L. Stalmans, J. Poortmans, J. Nijs, L. Scgirone, G. Sotgiu, S. Strehlke. C. Levy-Clement, *Sol. Energy Mater. Sol. Cells.* 60 (2000) 391.
- [7] M. Lipinski, P. Panek, E. Bielanska, J. Weglowska, H. Czernastek, *Opto-Electron. Rev.* 8, 4 (2000) 418.
- [8] B. Gonzalez-Diaz, R. Guerrero-Lemus, B. Diaz-Herrera, N. Marrero, J. Mendez-Ramos, Dietmar Borchert, *Mater. Sci. Eng. B.* 150/160 (2009) 295.
- [9] M. Bouchaour, A. Ould-Abbas, N. Diaf, N. Chabane Sari, *J. Ther. Anal. Calorim.* 76 (2004) 677.
- [10] M. Nahidi, K.U. Kolasinski, *J. Electrochem. Soc.* 153, 1 (2006) C19.
- [11] S. Adachi, M. Oi, *J. Appl. Phys.* 102 (2007) 063506-1.
- [12] J. Xu, A.J. Steckl, *Appl. Phys. Lett.* 65, 16 (1994) 2081.
- [13] K. Tomioka, S. Adachi, *Appl. Phys. Lett.* 87 (2005) 251920-1.
- [14] K. Uchida, K. Tomioka, S. Adachi, *J. Appl. Phys.* 100 (2006) 014301-1.
- [15] S.D. Campbell, L.A. Jones, E. Nakamichi, F.X. Wei, L.D. Zajchowski, *J. Vac. Sci. Technol. B.* 13, 3 (1995) 1184.
- [16] N. Gabouse, S. Bellhousse, R. Outemzabet, *Acta Phys. Slov.* 53, 3 (2003) 207.
- [17] B. Gonzalez-Diaz, R. Guerrero-Lemus, J. Mendez-Ramos, B. Diaz-Herrera, B. Diaz-Herrera, V.D. Rodriguez, *Sens. Actuators. A* 150 (2009) 97.
- [18] V.A. Makara, M.M. Melnichenko, K.V. Svezhentsova, L.Yu. Khomenkova, O.M. Shmyryeva, *Semicond. Phys. Quantum Electron. Optoelectron.* 6, 4 (2003) 492.
- [19] E.A. Starostina, V.V. Starkov, A.F. Vyankin, 31, 2 (2002) 88.
- [20] F.A. Ben Hander, J.D. Moreno, M.L. Marcos, J. Gonzalez Velasco, *J. New Mater. Electrochem. Syst.* 6 (2003) 129.
- [21] S. Lazarouk, P. Jaguiro, S. Katsouba, G. Maiello, S. La Monica, G. Masini, E. Proverbio, A. Ferrari, *Thin Solid Films.* 297 (1997) 97.
- [22] Z.C. Feng, R. Tsu. *Porous silicon*. World Scientific Publishing. New-York NY, 1995.
- [23] A. Kux, M. Ben Chorin, *Mater. Res. Soc. Symp. Proc.* 358 (1995) 447.
- [24] F.A. Rustamov, N.H. Darvishov, M.Z. Mamedov, E.Y. Bobrova, H.O. Qafarova, *J. Lumin.* 131, 10 (2011) 2078.
- [25] K.W. Kolasinski, J.W. Gogola, *ECS Trans.* 33 (2011) 23.
- [26] M.J. Winton, S.D. Russell, J.A. Wolk, R. Gronsky, *Appl. Phys. Lett.* 69 (1996) 4026.

Received: 19.05.2012

## MEASUREMENT OF THE PULSE SHAPE AND PULSE ENERGY DISTRIBUTION AT THE IBR-2M REACTOR

A.A. GARIBOV<sup>2</sup>, R.N. MECHTIYEVA<sup>2</sup>, L.A. TAYIBOV<sup>1,2</sup>

<sup>1</sup> Joint Institute for Nuclear Research,

141980 Dubna, Joliot-Curie street, 6, Russia

<sup>2</sup> Institute of Radiation Problems, Azerbaijan National Academy of Sciences,  
Baku, AZ-1143, B. Vaxabzade street, 9, Azerbaijan

The IBR-2M pulse shape and pulse energy distribution density have been investigated during the physical startup of the reactor. The experimental data on the pulse shape allow the average lifetime of prompt neutrons to be estimated at  $\tau = (6,46 \pm 0,3) \cdot 10^{-8}$  s. It was shown that the experimental results are close to the calculated ones.

**Keywords:** IBR-2M reactor, pulse energy, pulse shape, lifetime of prompt neutrons.

**PACS:** 621.039.56

### 1. BRIEF DESCRIPTION OF THE MODERNIZED IBR-2 REACTOR

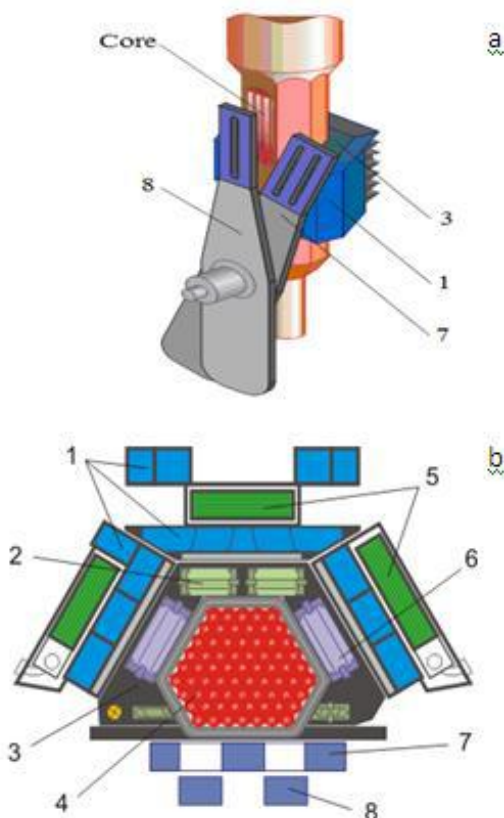


Fig. 1. a) IBR-2M reactor, b) Horizontal section of IRR-2M: 1 - Water moderators; 2 - Emergency system; 3 - Stationary reflector; 4 - Fuel assemblies; 5 - Cold moderators; 6 - Control rods; 7 - Main moveable reflector; 8 - Auxiliary moveable reflector.

The IBR-2M pulsed fast research reactor with the nominal power of 2 MW is a modernized version of the IBR-2 reactor which was shut down in 2006 because its service life had come to the end [1].

The core and the shell, stationary reflectors, and control and emergency protection elements were completely replaced in the course of modernizing. The

IBR-2M core differs from the IBR-2 core by a smaller size and absence of the central channel. The IBR-2M reactor and its horizontal section are schematically shown in Fig. 1.

The IBR-2M fuel elements are identical to the IBR-2 fuel elements. They are PuO<sub>2</sub> pellets. The reactor coolant is liquid sodium. The IBR-2M reactivity level is adjusted by the control and protection system elements, which are movable tungsten blocks in the array of stationary reflectors. Neutron pulses are produced by the reactivity modulator that had been in operation at IBR-2 since 2004. The reactivity modulator consists of the primary movable reflector (PMR) and the secondary movable reflector (SMR). The primary movable reflector rotor is a blade with three “teeth”, and the secondary movable reflector rotor is a blade with two “teeth”. The rotors of the main and secondary movable reflectors rotate in opposite directions with different velocities. When both reflectors coincide near the reactor core, a power pulse is generated. Some of the main parameters of IBR-2M reactor are presented in Tab. 1.

### 2. MEASUREMENT PROCEDURE

The pulse shape was measured for fast neutrons. In all measurements the reactor state was as follows: the system of water moderators was in the standard state, the primary movable reflector and secondary movable reflector blades were in the maximum reactivity position. The fast-neutron pulse shape is measured at a power of 20 kW using the Th fission chamber placed in the 1st horizontal neutron beam on a flight path of 11 m.

The pulse energy was recorded by a specially designed measuring system. The measuring system is shown in Fig.2. The neutron detector was the KNK-53M chamber placed near the core immediately at the moderator on its first horizontal neutron beam side. After accumulation of 8 192 successive pulse energy values the data were recorded in the file for further processing. The statistical analysis of temporal series was used. The density and parameters of the pulse energy distribution were calculated.

Table. 1. Parameters of IBR-2M

Average power, MW	2
Fuel	PuO <sub>2</sub>
Number of fuel assemblies	69
Maximum burnup, %	9
Pulse repetition rate, Hz	5; 10
Pulse half-width, μs: fast neutrons thermal neutrons	220 340
Rotation rate, rev/min: main reflector auxiliary reflector	600 300
MMR and SMR material	nickel + steel
Movable reflector service life, hours	55000
Background, %	7.5
Thermal neutron flux density from the surface of the moderator: - time average - burst maximum	~ 10 <sup>13</sup> n/cm <sup>2</sup> ·s ~ 10 <sup>16</sup> n/cm <sup>2</sup> ·s

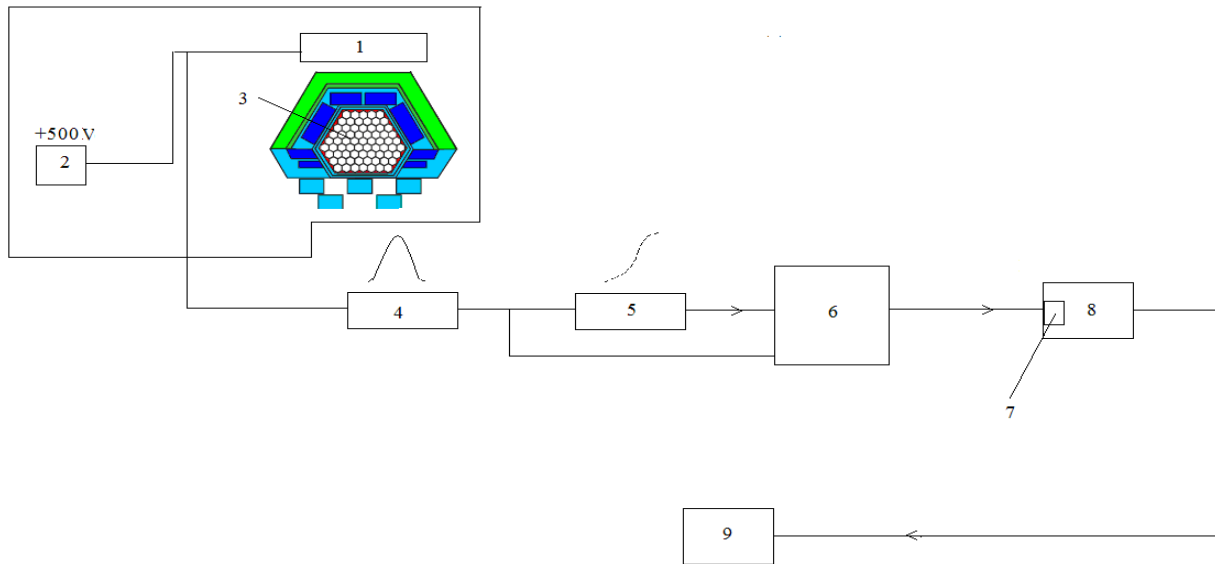


Fig. 2. Diagram of measuring the pulse energy of the IBR-2M

1—Ionization chamber, 2— Power supply, 3— Active core, 4— Amplifier pulse current, 5— Integrator, 6 — Digital converter pulse, 7— Communication controller, 8—Workstation, 9— Data processing station.

### 3. MAIN RESULTS AND ESTIMATION OF THE LIFETIME OF PROMPT NEUTRONS ( $\tau$ ) FROM THE POWER PULSE SHAPE

More detailed information on stochastic properties of reactor noise can be obtained from the pulse energy

distribution density  $P_T(n)$ , where  $n$  is the number of neutrons per pulse. According to [2], the distribution of the number of neutrons in the reactor during a burst corresponds to the Polya negative binomial distribution

$$P_T(n) = P_T(0) \left( \frac{\bar{n}}{1 + \Delta_{st}^2 \bar{n}} \right)^n \frac{(1 + \Delta_{st}^2)(1 + 2\Delta_{st}^2) \dots [1 + (n-1)\Delta_{st}^2]}{n!}, \quad (1)$$

where  $\Delta_{st}^2 = \frac{v \cdot D}{2S\tau}$  is the relative dispersion of stochastic fluctuations,  $D$  and  $v$  are the dispersion of the number of prompt neutrons and the average number of neutrons in a single fission event respectively,  $\tau$  — is the lifetime of prompt neutrons in the core,  $S$  — is the intensity of the neutron source continuously operating

during a pulse,  $\bar{n}$  — is the average number of neutrons per pulse. In the asymptotic case of  $\bar{n} \gg 1$  and  $\Delta_{st}^2 \bar{n} \gg 1$  (these inequalities hold at practically any power level), the distribution (1) passes into the standard distribution

$$P_T(n)dn = \left( \frac{n}{\Delta_{st}^2} \right)^{1/\Delta_{st}^2 - 1} \exp \left\{ - \frac{n}{\Delta_{st}^2} \right\} \frac{dn}{\Delta_{st}^2 \Gamma(1/\Delta_{st}^2)} , \quad (2)$$

where  $\Gamma(x)$  — is the gamma function. Using the notation

$$X = \frac{n}{\Delta_{st}^2} , \text{ we write expression (2) in the form}$$

$$P_T(X)dX = \frac{(X)^{1/\Delta_{st}^2 - 1}}{\Gamma(1/\Delta_{st}^2)} e^{-X} dX . \quad (3)$$

For a “weak” source ( $S\tau \ll 1$ ) the distribution (3) is sharply asymmetric with a shift to lower pulse intensities. For a “strong” source ( $S\tau \gg 1$ ) the  $n/\bar{n}$  distribution tends to the Gaussian shape. The “strong” source condition is fulfilled at an average power above 1 W. By way of example, Fig. 3 shows the calculated shape of the energy distribution for the upgraded IBR–2 reactor pulses at a few average power levels.

Figure 4 shows the measured pulse energy distribution at a number of average power levels and the calculated distribution shape approximating the experimental points in terms of the free parameter of

average power. As is evident from Fig. 4, the distributions are well approximated by the Gaussian dependence.

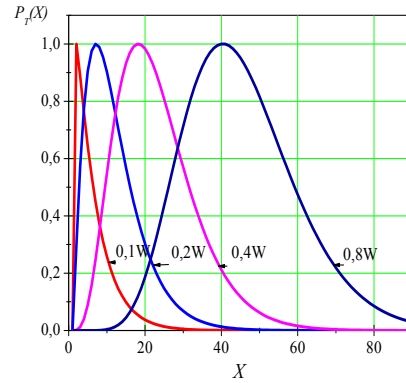


Fig. 3. Calculated density of the IBR–2M pulse energy distribution.

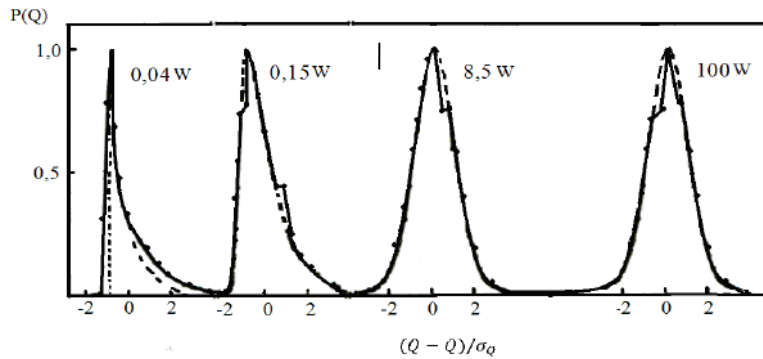


Fig. 4. Normalized measured pulse energy distribution density of the IBR–2M at some average power levels. The dashed line is approximation by (3).

The theoretical pulse shape within the single-point model is discussed at length in [3]. The power pulse shape (time dependence of the fission neutron generation rate) at the parabolic reactivity variation near the peak is defined with an accuracy about 0.1% by the formula [3]

$$N(t) = S \cdot \frac{\sqrt{B\pi}}{\varepsilon_m} \cdot \exp \left[ - \frac{Bt^2}{3} (\bar{t} - 3) \right] \quad (4)$$

where  $\bar{t}$  — is the time,  $B = \varepsilon_m^{3/2} / \alpha^{1/2} \omega \tau$  — is the dimensionless parameter,  $S$  — is intensity of generation of delayed neutrons,  $\varepsilon_m$  — is the pulse super criticality,  $\alpha$  is the parabola coefficient of the reactivity modulator,  $\omega = 360N$  — is the angular velocity of the reactivity

modulator,  $N = 10s^{-1}$  — is the rotation frequency of the main reactivity modulator in the modernized IBR–2 reactor. In the Gaussian approximation, the pulse shape near the peak quite well agrees with the exact shape. Here, according to [3], the half-width of the power pulse is defined by the formula

$$\theta_{1/2} = 2 \cdot \sqrt{B \ln 2} \cdot \tau / \varepsilon_m , \quad (5)$$

for the equilibrium mode, it is

$$\theta_{1/2} = 1,4 \cdot (\tau / \alpha \omega^2)^{1/3} . \quad (6)$$

The measured power pulse shape for fast neutrons is shown in Fig. 5. The duration of the fast-neutron burst at half maximum is  $\theta_{1/2} = 220 \pm 3 \mu s$ .

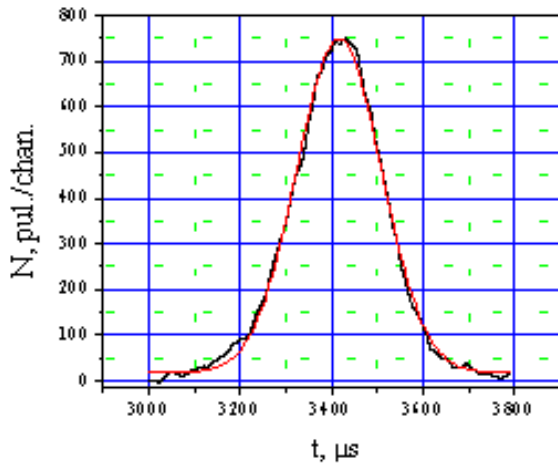


Fig. 5. Shape of the modernized IBR-2 reactor power pulse for fast neutrons (Gaussian approximation is given).

For the equilibrium mode with the burst repetition rate  $5\text{s}^{-1}$ , using the experimental values  $\theta_{1/2} = 220 \pm 3 \mu\text{s}$ ,  $\alpha = 1.29 \cdot 10^{-3} \text{ deg}^{-2}$ , and  $\omega = 360N \text{ (deg/s)}$ , from (6) we obtain  $\tau = (6,46 \pm 0,3) \cdot 10^{-8} \text{ s}$ . The calculated value is  $\tau = (6.50 \pm 0.5) \cdot 10^{-8} \text{ s}$  [4]. Thus, estimate of the lifetime of prompt neutrons made from the power pulse shape is rather close to the calculated value.

- 
- [1] V.D. Ananaev, A.V. Vinogradov, A.V. Dolgikh. IBR-2 Reactor: Operation and Prospects for Development. In: 11th Annual Russian Workshop on Safety of Research Nuclear Facilities, Dimitrovgrad, 2009, pp. 69–77.
- [2] A.B. Govorkov, B.Kozik. Statistics of IBR Reactor Burst Amplitudes. Preprint JINR R-2076, Dubna, 1965.
- [3] E.P.Shabalin. Pulsed Fast Reactors, Moscow, Atomizdat, 1976.
- [4] R.N. Mekhtieva, Yu.N. Pepelyshev, A.D. Rogov, et al. Calculation of the Effective Fraction of Delayed Neutrons and the Lifetime of Prompt Neutrons in the IBR-2M Reactor, Preprint JINR R-13-2010-89, Dubna, 2010.

Received: 25.06.2012



---

---

**CONTENTS**

---

---

1.	SHF-magnetic resonances in nickel-zinc ferrite <b>A.A. Habibzade, Sh.N. Aliyeva, S.I. Aliyeva, T.R. Mehdiyev</b>	3
2.	NANO-fractal structures on (0001) Van-der-Waals surface of $A^V_2B^{VI}_3$ crystals <b>F.K. Aleskerov, S.A. Nasibova, R.M. Tagiyev, A.Sh. Kakhramanov</b>	17
3.	Radiative recombination in $MnGa_2Se_4$ single crystals <b>T.G. Kerimova, O.B. Tagiyev, S.G. Asadullayeva, I.B. Bahtiyarli, K.O. Tagiyev</b>	24
4.	Superion conduction of $TlInSe_2$ crystals radiated by $\gamma$ – quantum <b>R.M. Sardarli, O.A. Samedov, N.A. Aliyeva, A.P. Abdullayev, F.T. Salmanov, S.F. Samedov, A.M. Aleskerov</b>	27
5.	The incidence angle influence on the structure of secondary-emission characteristics of single crystals <b>E.R. Gasanov, B.Z. Aliyev</b>	31
6.	Relativistic quantum free particle in a variable homogeneous field <b>Shakir M. Nagiyev, Konul Sh. Jafarova</b>	35
7.	Formation of lateral homogeneous stain etched porous silicon with acetic acid at oxidant insufficiency <b>F.A. Rustamov, N.H. Darvishov, M.Z. Mamedov, E.Y. Bobrova, H.O. Gafarova</b>	44
8.	Measurement of the pulse shape and pulse energy distribution at the IBR-2M reactor <b>A.A. Garibov, R.N. Mechtiyeva, L.A. Tayibov</b>	50



[www.physics.gov.az](http://www.physics.gov.az)